Measurement of seawater by refractometric methods

Instrumentation and Measurement Science

Kristian Børve

Department of Physics and Technology

University of Bergen

August 2013

Abstract

The aim of this work has been to design and test a refractometer for accurate measurement of seawater refractive index. The goal was to create a refractometer with a cylindrical embodiment and measure refractive indices with an accuracy of 10^{-6} refractive index units (RUI).

The realization of the instrument resulted in a measurement chamber consisting of a cylindrical glass tube with an inner radius if 4 mm, thickness of 1 mm and length of 115 mm. To transverse the laser beam into the glass cylinder in a satisfactory way, the beam is directed by mirrors submerged in an immersion oil. The oil functions as a "compensating" medium between the air-glass interface and was only used because desired embodiments were not available. The final refractometer design was decided after rigorous computer simulations.

The experiments were conducted by measuring the laser beam displacement of sodium chloride solutions, with salinities ranging from 0 to 40 parts per thousand. A brief temperature measurement was also conducted.

The results revealed that the instrument was able to short-term measurements with an accuracy of $1.5 \cdot 10^{-5}$ RIU, but poor repeatability of the instrument decreased the overall accuracy to $2.9 \cdot 10^{-4}$ RIU. The increased uncertainties is considered to be caused by either small displacements in the tweakable components in the setup or by slow drifts in the laser/detector caused by heating processes.

Acknowledgements

I would first like to thank my supervisor, professor Lars Egil Helseth, for engagement, guidance and support through this last year's period of work. My thanks also to Xiaodong Guo for helping with the vaporising system. And to the institute workshop for making important parts for my setup.

Thanks also to Jostein Hovdenes (AADI), Jon Hellevang (CMR), Peter Thomas (CMR), and Benny Svardal (CMR) for a rewarding and interesting meeting, where the basic design idea of the setup first arose.

At last, thanks to my fellow students, friends and family, especially my sister, for their help and support.

Table of Contents

List of Common Symbols

Symbol	Quantity	Unit
S_A	Absolute salinity	g/kg
$\vec{\boldsymbol{E}}$	Electric field	V/m
$\vec{\boldsymbol{H}}$	Magnetic intensity	A/m
$\vec{\boldsymbol{J}}$	Current density	A/m^2
$\vec{\boldsymbol{D}}$	Electric displacement	C/m^2
$\vec{\boldsymbol{B}}$	Magnetic field	T
σ	Charge density	C/m^2
ρ	Charge density	C/m^3
μ , K_M	Permeability	$C^2/N\,m^2$
ϵ , K_E	Permittivity	N/A^2
g	Conductivity	S/m
n	Refractive index	Ratio
k	Wave number	m^{-1}
ω	Angular frequency	rad/s
u_E , u_M	Energy	J
I	Irradiance	W/m^2
$\vec{\boldsymbol{p}}$	Dipole moment	$C\,m$
f	Frequency	$1/s$
λ	Wavelength	m

List of Acronyms

Acronym	Explanation
psu	Practical salinity unit
ppt	Parts per thousand
ppm	Parts per million
PSS	Practical Salinity Scale
PSD	Position Sensitive Detector
RIU	Refractive Index Unit
EQE	External Quantum Efficiency
rms	Root mean square
SNR	Signal-to-noise ratio
PVC	Polyvinyl chloride
SAN	Styrene Acrolynitrile

1 Introduction

1.1 Background

The salinity of water is an important property which must be monitored in wide field of applications. Industrial applications vary from leakage detection, build up in cooling systems, to water treatment in agriculture and aquaculture [1] [2] [3]. The field in greatest need of high precision salinity measurement is probably oceanographic research, which has been studying ocean salinity from its very beginning in the 1870's [4]. The behavior of the ocean is directly related to the parameters temperature, pressure and salinity. From these three parameters the density of water can be determined, which again determines oceanic currents. Understanding the behavior of the ocean is of highest interest because of our activity there. The ocean also has a huge influence on atmospheric weather and climate. This influence can be to some extent observed by salinity measurements at sea surface, by tracking the net flow of water at the oceans. This water flow takes the form of evaporation, ice melting, river estuaries, rainfall, and so on [5] [6].

Absolute salinity is traditionally defined as the mass fraction of dissolved material in seawater, expressed in $g\,kg^{-1}$ and denoted S_A. This mass is difficult to measure in practice, and it was nearly impossible to do off-shore measurements in early ages due to limited sensitivity of existing balances. An international protocol was adopted in 1902 saying; salinity becomes the mass of solids contained in one kilogram of seawater after carbonates are transformed into oxides, bromide and iodide being replaced by the equivalent of chloride, and all organic matter is oxidized [7]. This implicit assumption that the composition of seawater is constant was used with modification until new conductimetric methods were introduced in the 1960's. Since conductivity sensors do not measure absolute salinity but the amount of electrolytes, the Practical Salinity Scale of 1978 (PSS 78) was introduced and is still used today. In this thesis practical salinity is denoted “psu” (practical salinity unit) even though this concept has limited validity. The PSS 78 and conductimetric methods are further explained in section 2.3. Accuracy of salinity measurements

done by conductimetric methods have an absolute limit of 0.003 ppt (parts per thousand) [8]. This limitation is caused by high correlations between conductivity and temperature and the lack of sensitivity to seawater composition. To progress in observing and modelling the thermodynamic properties of the seas, it is clear that new measurements methods must be adapted. Already before the 19th century the direct relation between absolute salinity and refractive index was known. However, it was not until recently optical equipment with required resolution and accuracy has become available [9]. Current position sensitive detectors (PSD) are able to measure laser beam positions with an accuracy of 0.3 μm. Thus, the refractive index of water, denoted RIU (refractive index unit), is currently the most promising parameter to measure when determine salinity of seawater. A refractive index sensor must be able to cover the range of oceanic conditions: from -2 to 40 °C in temperature, from 0 to 40 in psu, and from 0 to 11 000 dbar in pressure [10]. The accuracy of measurements must be 1 ppm (part per million) at atmospheric pressure, and 3 ppm at high pressure [11]. The sensor is also desired to have long-term stability of several months, particular for applications in automatic observational systems.

Several optical sensors have been successfully tested in laboratory environment with required resolution and range [12] [13]. A common feature of these refractometer setups is the geometrical choice of embodiment. All of these embodiments have geometrical breaking points (sharp edges and corners) giving them advantages of high ratio between size and resolution. But in situ application, the refractometers experience several disadvantages. Having geometrical breaking points will increase the complexity of estimating deformation of the embodiment caused by stress and strain due to high pressure. Implementation of effective protection against biofouling is also much harder. It is therefore safe to conclude that none of these refractometers are optimal suited for long-term automatic in situ measurements.

The objective of this thesis was to construct and test an instrument that measures the refractive index seawater. The sensor requirements mentioned above was attempted to be met; though extra priority was laid on practicality and long-term stability of in situ measurements. This resulted in construction of a refractometer

with a cylindrical sample container chamber. This sensor geometry has not been tested before and should give substantial advantages for in situ application. The refractometer has been tested with water samples covering the oceanographic range in salinity. There has also been brief testing of the refractometer with different temperatures.

1.2 Outline of thesis

The work in this thesis is presented in the following way:

- Chapter 2 gives an introduction to the basic theory of electromagnetic wave propagation, and how this theory are applied to measure refractive indices of water solutions. Also the different electrical and optical components relevant for the measurements are presented.
- Chapter 3 introduces the actual measurement setups, how the setups are designed, constructed and configured is explained.
- Chapter 4 presents the raw data of the different measurements. At first static measurements of the different components to determine noise and errors. Afterwards measurements of a wide variety of NaCl samples are presented, and at last measurements of how temperature changes impacts the sensor.
- Chapter 5 contains the discussion and final conclusions of the thesis. The performance of the measurement setups are evaluated and compared to theoretical models. An ideal instrument is presented, with characteristic estimations based on measurement results in this thesis.

2 Theoretical background

This chapter reviews the theoretical background needed for the development and understanding of this thesis. Basic geometric and physical optics will be covered. Theory of the physical properties of materials and electrical components used in the experiments will also be reviewed.

2.1 Propagation of Electromagnetic Waves

2.1.1 Maxwell's Equations

From observation of certain experiments like simply putting a conducting coil in a magnetic field, empirical equations describing electromagnetic physics was formed [14]. Some of the most important of these equations are known as Maxwell's Equations [15]:

$$\nabla \times \vec{\boldsymbol{H}} = \vec{\boldsymbol{J}} + \frac{\partial \vec{\boldsymbol{D}}}{\partial t}, \tag{2.1}$$

$$\nabla \times \vec{\boldsymbol{E}} = -\frac{\partial \vec{\boldsymbol{B}}}{\partial t}, \tag{2.2}$$

$$\nabla \cdot \vec{\boldsymbol{D}} = \rho, \tag{2.3}$$

and

$$\nabla \cdot \vec{\boldsymbol{B}} = 0, \tag{2.4}$$

where $\vec{\boldsymbol{H}}$ is defined as magnetic intensity, $\vec{\boldsymbol{J}}$ as current density, $\vec{\boldsymbol{D}}$ as electric displacement, ρ as charge density and $\vec{\boldsymbol{B}}$ and $\vec{\boldsymbol{E}}$ are defined as magnetic and electric fields. Extensive experimental works have shown that these equations are applicable to all macroscopic situations [15]. An important consequence of Maxwell's equations is the equations for electromagnetic wave propagation in a linear medium. The wave equation can be derived by take the curl of (2.2):

$$\nabla \times \nabla \times \vec{\boldsymbol{E}} = -\nabla \times \frac{\partial \vec{\boldsymbol{B}}}{\partial t}. \tag{2.5}$$

Using the relation $\vec{H} = \frac{1}{\mu}\vec{B}$ and equation (2.1) yields

$$\nabla\times\nabla\times\vec{E} = -\frac{\partial}{\partial t}\left(\mu\vec{J} + \mu\frac{\partial\vec{D}}{\partial t}\right). \tag{2.6}$$

By setting $\vec{D} = \epsilon\vec{E}$, $\vec{J} = g\vec{E}$ and assuming the absolute permittivity ϵ, conductivity g and absolute permeability μ to be constant, we obtain:

$$\nabla\times\nabla\times\vec{E} = -g\mu\frac{\partial\vec{E}}{\partial t} - \epsilon\mu\frac{\partial^2\vec{E}}{\partial t^2}. \tag{2.7}$$

Using the operator identity $\nabla\times\nabla\times = \nabla\nabla\cdot - \nabla^2$ and restricting the application of the equation to a charge free medium so that $\rho = \nabla\cdot\vec{D} = \epsilon\nabla\cdot\vec{E} = 0$, we obtain

$$\nabla^2\vec{E} - g\mu\frac{\partial\vec{E}}{\partial t} - \epsilon\mu\frac{\partial^2\vec{E}}{\partial t^2} = 0. \tag{2.8}$$

Even though seawater is conductive, we restrict ourselves to only nonconducting mediums to simplify further progress. This yields a general equation,

$$\nabla^2\vec{E} = \epsilon\mu\frac{\partial^2\vec{E}}{\partial t^2}, \tag{2.9}$$

of a wave traveling with the phase velocity $v_p = \sqrt{\frac{1}{\epsilon\mu}}$. And as predicted the phase speed of light in empty space, where $\mu = \mu_0$ and $\epsilon = \epsilon_0$, will be [15]:

$$c = \sqrt{\frac{1}{\epsilon_0\mu_0}} = 2{,}99979\times10^8 m/s. \tag{2.10}$$

The ratio of speed of light in vacuum and the phase speed of light in a medium, is defined as the absolute index of refraction of the dielectric medium

$$n \equiv \frac{c}{v_p} = \sqrt{\frac{\epsilon\mu}{\epsilon_0\mu_0}}. \tag{2.11}$$

In terms of relative permittivity K_E and relative permeability K_M, where $\epsilon = K_E\epsilon_0$ and $\mu = K_M\mu_0$, n becomes

$$n = \sqrt{K_E K_M}. \tag{2.12}$$

We only want to investigate materials that are transparent in visible light, and these are essentially nonmagnetic [14]. Thus we can assume that $\mu \approx \mu_0$ and simplify

the expression for refractive index further:

$$n \approx \sqrt{K_E} = \sqrt{\frac{\epsilon}{\epsilon_0}} . \tag{2.13}$$

This expression is known as Maxwell's Relation [14].

2.1.2 Boundary Conditions

When an electromagnetic wave propagates from one medium to another, there are boundary conditions at the interface between the two media that must be fulfilled. We can deduce these condition requirements from Maxwell's equation.

We start with investigating the tangential component of the electrical field at the boundary.

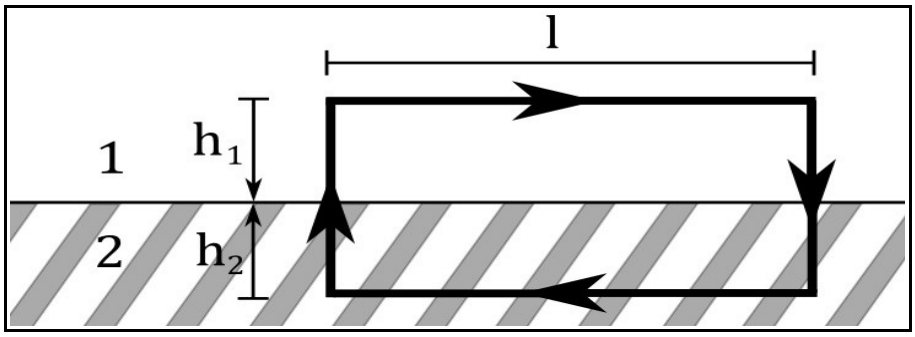

Figure 2.1: The rectangular path at the interface between two media.

By integrating equation (2.2) over the surface bounded by a rectangular loop such as that shown in Figure 2.1 we obtain

$$\int_S \nabla \times \vec{\boldsymbol{E}} \cdot \vec{\boldsymbol{n}}\, da = -\int_S \frac{\partial \vec{\boldsymbol{B}}}{\partial t} \cdot \vec{\boldsymbol{n}}\, da , \tag{2.14}$$

where $\vec{\boldsymbol{n}}$ is the normal vector of the boundary surface. Applying Stokes's theorem to the left side of the expression above gives

$$l E_{1\mathrm{P}} - l E_{2\mathrm{P}} + h_1 E_{1\mathrm{N}} + h_2 E_{2\mathrm{N}} - h_1 E'_{1\mathrm{N}} - h_2 E'_{2\mathrm{N}} = -\int_S \frac{\partial \vec{\boldsymbol{B}}}{\partial t} \cdot \vec{\boldsymbol{n}}\, da ,$$

where E_P and E_N is the electrical field component parallel and normal to the

boundary surface. By letting h_1 and h_2 go towards zero the last four terms on the left side vanishes, also will the right side expression vanish since the area A_S after integration will be infinitesimally small provided that $\partial \vec{\boldsymbol{B}} / \partial t$ is bounded. This reveals that the tangential component (parallel to the surface) of $\vec{\boldsymbol{E}}$ must be continuous all across the boundary interface:

$$E_{1\mathrm{P}} = E_{2\mathrm{P}} . \tag{2.15}$$

The boundary condition of the normal component of electric field can be found by first investigating the boundary conditions of the electric displacement.

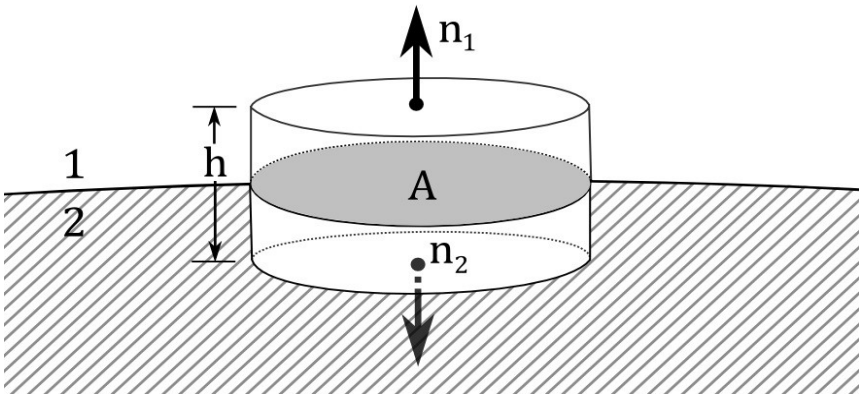

Figure 2.2: A Gaussian pill box at the interface between two media.

By integrating equation (2.3) over a cylinder-shaped volume, as in Figure 2.2, we obtain

$$\int_V \nabla \cdot \vec{\boldsymbol{D}} \, dv = \int_V \rho \, dv . \tag{2.16}$$

Applying the divergence theorem at this equation and letting h go to zero, reveals that

$$D_{1\mathrm{N}} - D_{2\mathrm{N}} = \sigma , \tag{2.17}$$

where σ is the charge density at the surface interface. If σ is not zero some complexity in the problem arises. But by demanding that the surface charge must be conserved, that $\nabla \cdot \vec{\boldsymbol{J}} = -\partial \rho / \partial t$, certain simplifications can be made [15].

Integrating this equation with the same procedure which resulted in equation (2.17) we obtain

$$J_{1N} - J_{2N} = -\frac{\partial \sigma}{\partial t}, \tag{2.18}$$

where J_{1N} and J_{2N} are the current density normal to the boundary surface inside the different media (corresponding to Figure 2.2). If we only consider monochromatic radiation, the surface charge density must vary with the same frequency as the radiation. Thus equation (2.18) can be rewritten as

$$J_{1N} - J_{2N} = j\omega\sigma . \tag{2.19}$$

Using the relation $\vec{D} = \epsilon \vec{E}$ and $\vec{J} = g\vec{E}$ and combining equation (2.17) and (2.19), we can eliminate σ and obtain

$$(\epsilon_1 + j\frac{g_1}{\omega}) E_{1N} = (\epsilon_2 + j\frac{g_2}{\omega}) E_{2N} . \tag{2.20}$$

The same integrating methods as used above on the electric field at a boundary, can be applied on equation (2.1) and (2.4). That will reveal the boundary conditions for the magnetic field, given as:

$$B_{1N} = B_{2N} \tag{2.21}$$

and

$$\frac{B_{1P}}{\mu_1} = \frac{B_{2P}}{\mu_2} . \tag{2.22}$$

2.1.3 Reflection and Transmission

Suppose we have plane monochromatic light wave which is incident at an interface between two media. The interface will split the incident wave into two waves, a reflected wave and a transmitted wave as shown in Figure 2.3.

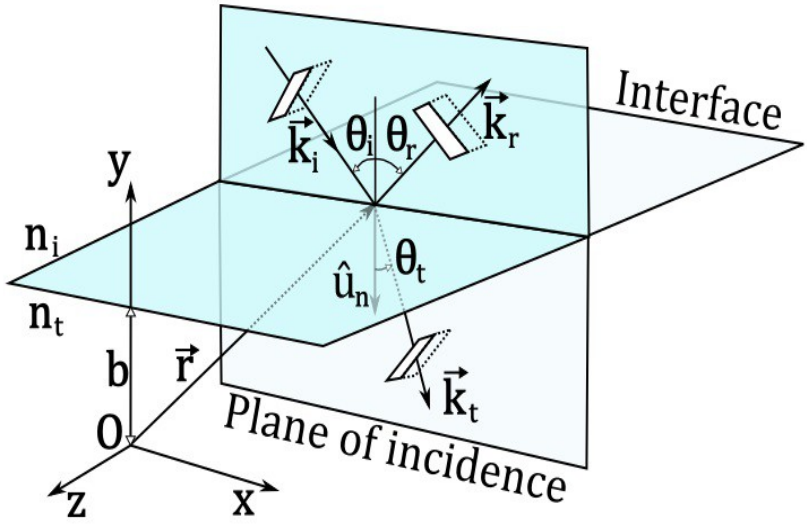

Figure 2.3: A plane wave splitting into a reflected and transmitted as it hits a interface between two media.

The incident wave is plane polarized and has the form

$$\vec{E}_i = \vec{E}_{0i} e^{j(\vec{k}_i \cdot \vec{r} - \omega_i t)} . \tag{2.23}$$

We can write the reflected and transmitted waves as

$$\vec{E}_r = \vec{E}_{0r} e^{j(\vec{k}_r \cdot \vec{r} - \omega_r t + \epsilon_r)} \tag{2.24}$$

and

$$\vec{E}_t = \vec{E}_{0t} e^{j(\vec{k}_t \cdot \vec{r} - \omega_t t + \epsilon_t)} , \tag{2.25}$$

where $k_{(r,t,i)}$ is the wavenumber of the waves, and ϵ_r and ϵ_t are phase constants relative to $\vec{E}_i$. The phases ϵ_r and ϵ_t are introduced because the position of the origin is not unique, but by aligning the coordinate system so that the origin O will be at the boundary interface ($\vec{r} = r\vec{x}$) the phases can be set to zero. This particular wave shown in Figure 2.3 only travels in the $\vec{y}$ and $\vec{x}$ direction, so we can write the wavenumbers as:

$$\vec{k}_i = k_i (\sin\theta_i \vec{x} - \cos\theta_i \vec{y}) , \tag{2.26}$$

$$\vec{\boldsymbol{k}}_r = k_r(\sin\theta_r \vec{\boldsymbol{x}} + \cos\theta_i \vec{\boldsymbol{y}}) , \tag{2.27}$$

and

$$\vec{\boldsymbol{k}}_t = k_t(\sin\theta_t \vec{\boldsymbol{x}} - \cos\theta_t \vec{\boldsymbol{y}}) . \tag{2.28}$$

If we introduce a unit vector $\vec{\boldsymbol{u}}_n$ normal to the interface; then regardless of the direction of an electric field, the cross-product between the field direction and $\vec{\boldsymbol{u}}_n$ will be perpendicular to $\vec{\boldsymbol{u}}_n$ and therefore parallel to the interface. By applying the boundary conditions described in equation (2.15), we obtain

$$\vec{\boldsymbol{u}}_n \times \vec{\boldsymbol{E}}_{0\mathrm{i}} e^{j(\vec{\boldsymbol{k}}_i \cdot \vec{\boldsymbol{r}} - \omega_i t)} + \vec{\boldsymbol{u}}_n \times \vec{\boldsymbol{E}}_{0\mathrm{r}} e^{j(\vec{\boldsymbol{k}}_r \cdot \vec{\boldsymbol{r}} - \omega_r t)} = \vec{\boldsymbol{u}}_n \times \vec{\boldsymbol{E}}_{0\mathrm{t}} e^{j(\vec{\boldsymbol{k}}_t \cdot \vec{\boldsymbol{r}} - \omega_t t)} . \tag{2.29}$$

This relation must remain at any instant in time and at any point on the interface $(y=0)$. As a consequence all the waves must have the same dependence on the variables t and r, and therefore also have the same frequency. Thus we can obtain the following relation from equation (2.29)

$$(\vec{\boldsymbol{k}}_i \cdot \vec{\boldsymbol{r}})|_{y=0} = (\vec{\boldsymbol{k}}_r \cdot \vec{\boldsymbol{r}})|_{y=0} = (\vec{\boldsymbol{k}}_t \cdot \vec{\boldsymbol{r}})|_{y=0} . \tag{2.30}$$

By using the relation $k = \omega / v_p = \omega n / c$ and inserting equation (2.26), (2.27) and (2.28) into equation (2.30) we obtain the relation:

$$n_i \sin\theta_i = n_r \sin\theta_r = n_t \sin\theta_t . \tag{2.31}$$

The relation between the angles of the incident and transmitted wave is called Snell's Law [14]:

$$n_i \sin\theta_i = n_t \sin\theta_t . \tag{2.32}$$

Since the incident and reflected wave is in the same medium, their refractive index is the same, revealing what is known as the Law of Reflection [14]:

$$\theta_i = \theta_r . \tag{2.33}$$

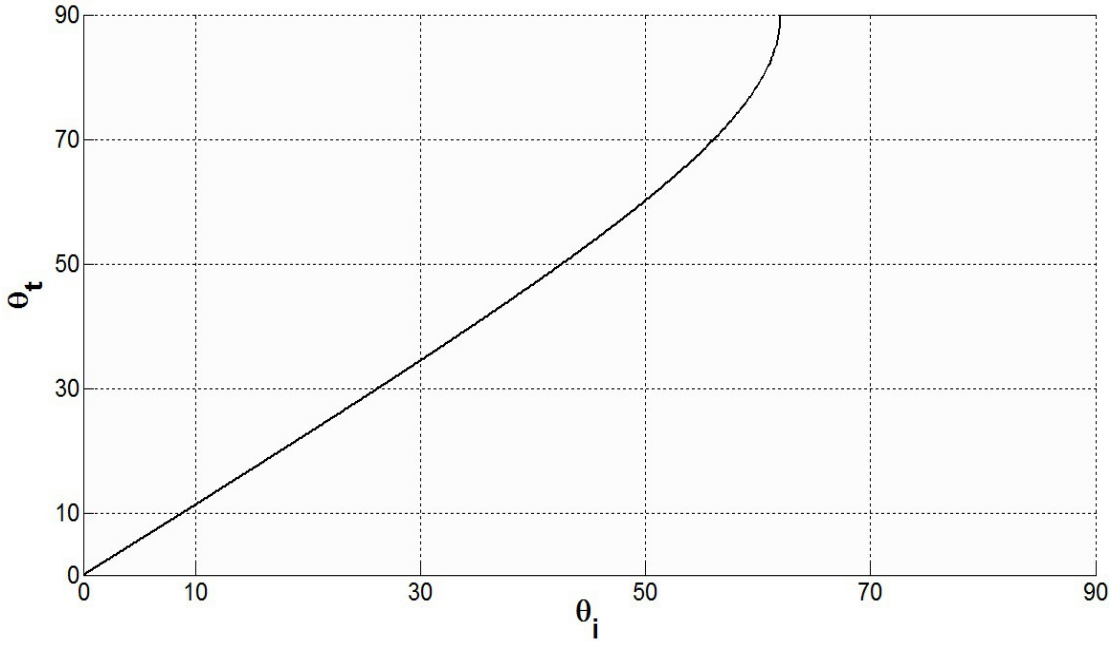

Figure 2.4: The transmission angle when n_i=1,51 and n_t=1,333 , corresponding to the refractive index of glass and water.

It can be shown that any form of light can be represented by two orthogonal linearly polarized waves [14]. So we are going to investigate the relations between the electrical wave amplitudes: the incident, reflected, and transmitted at the two extremities. That is when the electrical wave component is only either perpendicular or parallel to the plane of incidence.

First we assume that $\vec{E}$ is perpendicular to the plane of incidence and that $\vec{B}$ is parallel to it, as shown in Figure 2.5.

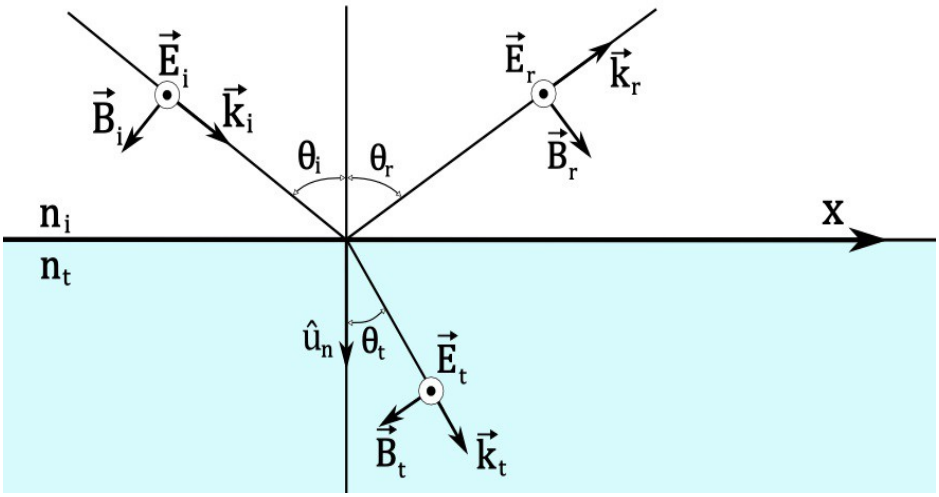

Figure 2.5: A polarized wave with the electrical component normal to the plane of incidence.

From the boundary condition in equation (2.15) we see the following relation between the electrical components

$$\vec{E}_i + \vec{E}_r = \vec{E}_t . \tag{2.34}$$

We also have to invoke the boundary conditions for the magnetic field, applying equation (2.32) gives us

$$\vec{B}_i + \vec{B}_r = \vec{B}_t . \tag{2.35}$$

We can relate the magnetic and electrical field by equation (2.70), revealing

$$\vec{k} \times \vec{E} = v_p \vec{B} . \tag{2.36}$$

By inserting this into equation (2.34) and doing the same substitution for the phase speed as done earlier, we obtain

$$n_i(\vec{k}_i \times \vec{E}_i + \vec{k}_r \times \vec{E}_r) = n_t(\vec{k}_t \times \vec{E}_t) . \tag{2.37}$$

By inserting equation (2.26), (2.27) and (2.28) we can rewrite the expression as

$$n_i \cos\theta_i (E_{0i} - E_{0r}) = n_t \cos\theta_t E_{0t} , \tag{2.38}$$

since the electrical field component in perpendicular to the xy-plane and the incident and reflected angle is equal. By using equation (2.34) to eliminate either the reflected or transmitted component from the expression. The result is two of the famous Fresnel Equations:

$$r_N \equiv \left(\frac{E_{0r}}{E_{0i}}\right)_N = \frac{n_i \cos\theta_i - n_t \cos\theta_t}{n_i \cos\theta_i + n_t \cos\theta_t} \tag{2.39}$$

and

$$t_N \equiv \left(\frac{E_{0t}}{E_{0i}}\right)_N = \frac{2 n_i \cos\theta_i}{n_i \cos\theta_i + n_t \cos\theta_t} . \tag{2.40}$$

Here the amplitude reflection coefficient is denoted r_N and the amplitude transmission coefficient is denoted t_N.

Here we assume that $\vec{E}$ is parallel and $\vec{B}$ is perpendicular to the plane of incidence. Following similar procedures as above, using the boundary conditions, it can be shown that [14]

$$(E_i - E_r)\cos\theta_i = E_t \cos\theta_t \tag{2.41}$$

and

$$n_i(E_i + E_r) = n_t E_t \tag{2.42}$$

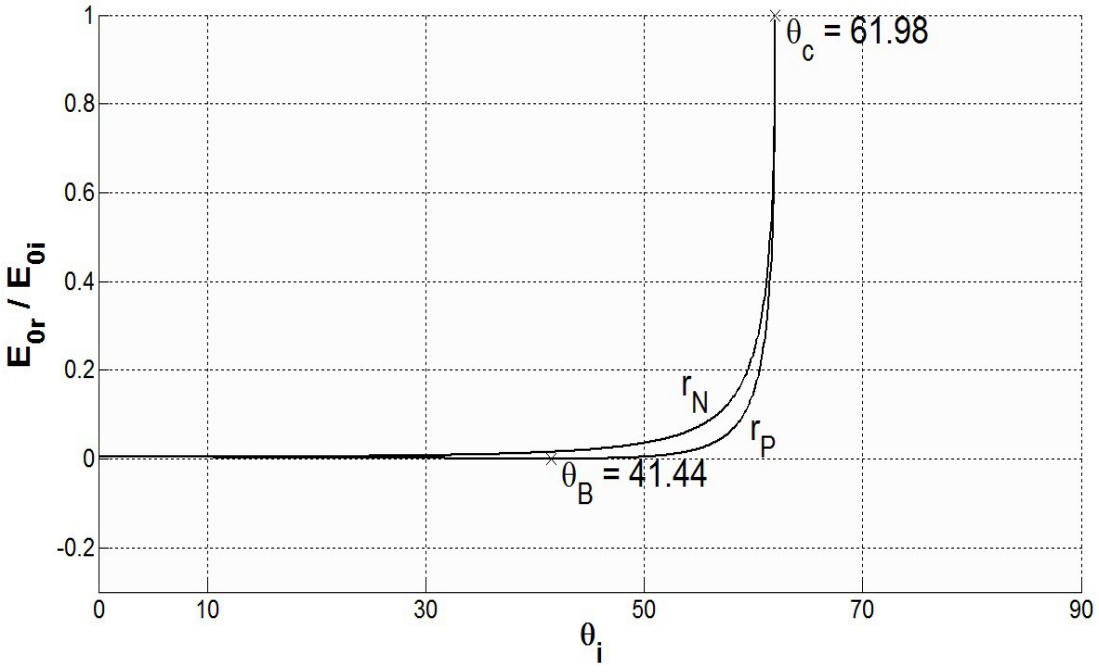

Figure 2.6: The amplitude reflection coefficients for polarized light when $n_i = 1{,}51$ *and* $n_t = 1{,}333$.

Combining the two equations above gives us the Fresnel Equations for a electrical

field which is polarized parallel with respect to the plane of incident:

$$r_P \equiv \left(\frac{E_{0r}}{E_{0i}}\right)_P = \frac{n_t \cos\theta_i - n_i \cos\theta_t}{n_i \cos\theta_t + n_t \cos\theta_i} \tag{2.43}$$

and

$$t_P \equiv \left(\frac{E_{0t}}{E_{0i}}\right)_P = \frac{2 n_i \cos\theta_i}{n_i \cos\theta_t + n_t \cos\theta_i} . \tag{2.44}$$

We can see on Figure 2.6 that there are some special cases depending on the refractive indexes and the incident angle. These special cases are known as Brewster's angle, the critical angle and the evanescent wave [14] [15].

Brewster's angle is the incident angle where there is no reflection of electromagnetic waves with parallel polarization (respect to the plane of incident). The angle is determined by Brewster's law [15]:

$$\theta_B = \tan^{-1}\left(\frac{n_t}{n_i}\right) . \tag{2.45}$$

Another special case is when there is no transmitted electromagnetic wave. This can only occur when $n_i > n_t$ and the incident angle is larger than the critical angle. Thus the critical angle is determined by:

$$\theta_c = \sin^{-1}\left(\frac{n_t}{n_i}\right) . \tag{2.46}$$

As mention above there is no transmitted wave when the incident angle is larger than the critical angle. But this assumption makes it impossible to satisfy the boundary conditions using only incident and reflected waves. Though by using the trigonometric relation $\cos\theta = \sqrt{1-\sin^2\theta}$ and introducing complex Fresnel coefficients we can show that there will be a transmitted wave penetrating into the new medium [14]. The wave advances along the boundary surface and will drop off exponentially, it can be described by:

$$\vec{E}_t = \vec{E}_{0t} \cdot e^{\pm\beta y} \cdot e^{j(k_t \vec{x} \sin\theta_i n_i / n_t - \omega t)} . \tag{2.47}$$

This transmitted wave is called the evanescent wave.

2.1.4 Reflectance and Transmittance

An important property of the electromagnetic wave that must be considered, is the transport of energy and momentum. From classical physics, electrical and magnetic fields are assumed to be continuous and store energy which also is continuous. Following this path of thinking, it is also logical to assume that an electromagnetic wave also stores energy in its extension in space. This physical attribute is often referred to as radian energy per unit volume, or energy density u [14]. In free space the energy density in the single electrical and magnetic field are given by [15]

$$u_E = \frac{\epsilon_0}{2} E^2 \tag{2.48}$$

and

$$u_B = \frac{1}{2\mu_0} E^2 . \tag{2.49}$$

From the relations $E = cB$ and $c = 1/\sqrt{(\epsilon_0 \mu_0)}$ in equation (2.10) and (2.70) it follows that

$$u_E = u_B . \tag{2.50}$$

Hence this, we conclude that the energy stream in a propagating electromagnetic wave is equally distributed between the electrical and magnetic field. Thus the total energy density in the wave can be expressed as following

$$u = u_E + u_B = \epsilon_0 E^2 = \frac{1}{\mu_0} B^2 . \tag{2.51}$$

Since electromagnetic wave is travelling trough space, it is natural to describe the rate of energy transportation in space. We let S symbolize the transport of energy per unit time across a unit area. Imaging now an electromagnetic wave travelling with speed c trough an area A, as shown in Figure 2.7. During the small time interval Δt, the energy crossing A will be contained in a cylindrical volume given by $u \cdot (c A \Delta t)$. Thus

$$S = \frac{u c A \Delta t}{A \Delta t} = u c = \frac{1}{\mu_0} EB . \tag{2.52}$$

The corresponding $\vec{S}$, known as the Poynting vector, must be

$$\vec{\boldsymbol{S}} = c^2 \epsilon_0 \vec{\boldsymbol{E}} \times \vec{\boldsymbol{B}} \,. \tag{2.53}$$

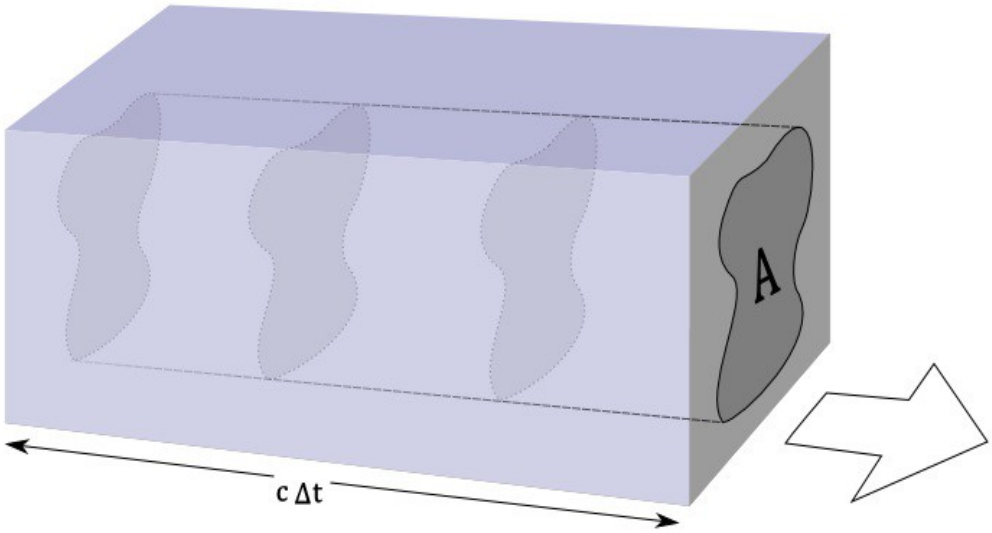

Figure 2.7: The electromagnetic energy flowing through space.

But when detecting an electromagnetic wave, the measurement cannot be done instantaneously. Most detectors average over a time period corresponding to many periods. This quantity corresponds average energy per unit area per unit time, called the irradiance and is denoted I . The irradiance can be measured by time-averaging the magnitude of the Poynting vector, symbolized by $\langle S \rangle_T$ where T is the period of the electromagnetic wave. Since the electromagnetic wave is a harmonic plane wave it can easily be shown that [14]

$$I \equiv \langle S \rangle_t = \frac{1}{T} \int_0^T \vec{\boldsymbol{S}} \, dt = c \, \epsilon_0 2 \, E_0^2 \tag{2.54}$$

or more general:

$$I \equiv \langle S \rangle_t = v_p \epsilon \, 2 \, E_0^2 \,. \tag{2.55}$$

Lets now review the example shown in Figure 2.3, where we have an incident, reflected and transmitted wave. The cross section area of these different beams at the

area A on the interface are $A\cos\theta_i$, $A\cos\theta_r$ and $A\cos\theta_t$. The power arriving or leaving the interface will accordingly be $I_i A\cos\theta_i$, $I_r A\cos\theta_r$ and $I_t A\cos\theta_t$. The reflectance R is defined to be the ratio of the reflected power to the incident power:

$$R \equiv \frac{I_r A\cos\theta_r}{I_i A\cos\theta_i}. \tag{2.56}$$

In similar manner, the transmittance T is defined as the ratio of the transmitted to the incident power:

$$T \equiv \frac{I_t A\cos\theta_t}{I_i A\cos\theta_i}. \tag{2.57}$$

By inserting equation (2.55) into (2.56) and since $v_{pi}=v_{pr}$ and $\epsilon_i=\epsilon_r$ we obtain

$$R = \left(\frac{E_{0r}}{E_{0i}}\right)^2 = r^2, \tag{2.58}$$

where r is the same amplitude reflection coefficient as first mentioned in the Fresnel equations. Inserting equation (2.55) into (2.57) and using the relation $\mu_0\epsilon=1/v_p^2$ (still assuming $\mu_i=\mu_t=\mu_0$) gives

$$R = \frac{n_t\cos\theta_t}{n_i\cos\theta_i}\left(\frac{E_{0t}}{E_{0i}}\right)^2 = \left(\frac{n_t\cos\theta_t}{n_i\cos\theta_i}\right)r^2. \tag{2.59}$$

Given that there are no absorption or other form of scattering, all the energy in the incident wave will be transferred to the reflected and transmitted wave. In other words the total energy flowing in and out of the area A per unit time must be equal, we can express this conservation of energy the following way

$$I_i A\cos\theta_i = I_r A\cos\theta_r + I_t A\cos\theta_t. \tag{2.60}$$

By multiplying both sides by c we can rewrite this expression as

$$1 = \left(\frac{E_{0r}}{E_{oi}}\right)^2 + \left(\frac{n_t\cos\theta_t}{n_i\cos\theta_i}\right)\left(\frac{E_{0t}}{E_{oi}}\right)^2 = R+T. \tag{2.61}$$

It can also easily be shown that

$$R_N+T_N = 1, \quad R_P+T_P = 1, \tag{2.62}$$

where

$$R_N = r_N^2, \quad R_P = r_P^2, \quad T_N = \left(\frac{n_t \cos\theta_t}{n_i \cos\theta_i}\right) t_N^2, \quad T_P = \left(\frac{n_t \cos\theta_t}{n_i \cos\theta_i}\right) t_P^2. \qquad (2.63)$$

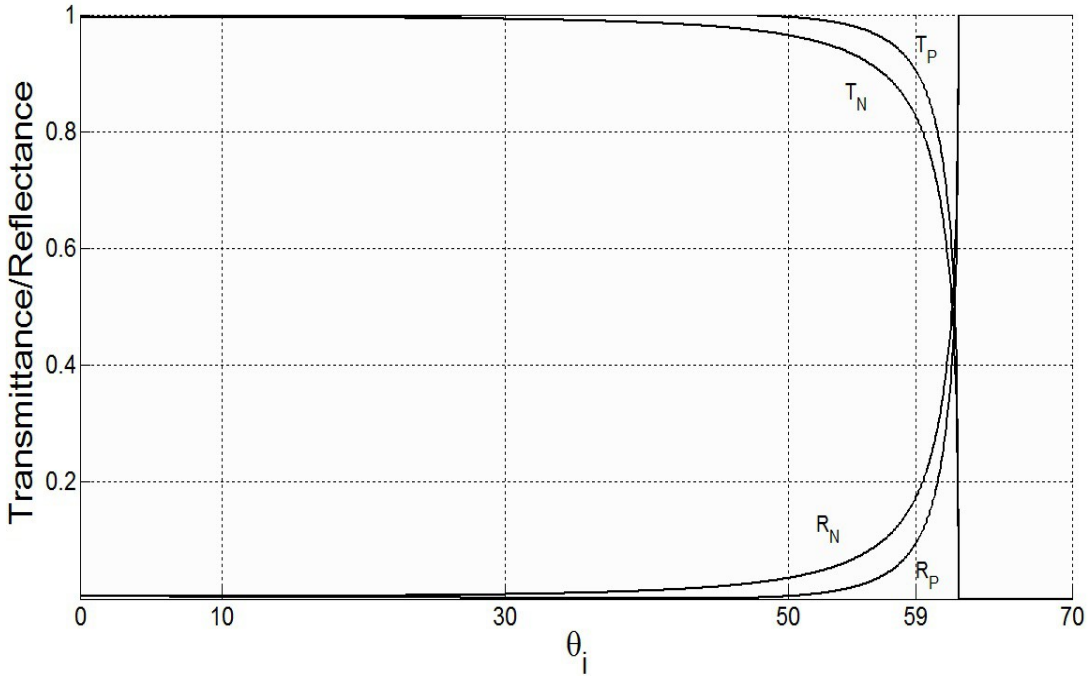

Figure 2.8: The transmittance and reflectance of a wave dependence on incident angle when $n_i = 1{,}51$ *and* $n_t = 1{,}333$.

2.1.5 Dispersion

The assumption that the relative permittivity is constant only holds for simple gasses. For most materials the permittivity, and thus also the refractive index, depends on the wavelength of the electromagnetic wave. This phenomena is called dispersion. We can look at dispersion theoretical by incorporating the atomic nature of matter and the frequency dependent aspect of that nature.

If we have a large number of atoms, the contribution of these can be averaged to represent the behavior of an isotropic dielectric medium. When the medium is subjected to an applied electric field, the internal charge distribution will be distorted corresponding to generation of electric dipole moments. When a simple charge is

displaced with the distance $\vec{x}_d$ from equilibrium state, the dipole moment is given by $\vec{p} = q\vec{x}_d$. The dipole charges will contribute to an additional electrical field component. The resultant dipole moment per unit volume is defined as the electric polarization

$$\vec{P} = \sum \vec{p} = N q \vec{x}_d , \tag{2.64}$$

when there are N dipole moments per unit volume. For most materials the polarization and electrical field can be related by [14]

$$(\epsilon - \epsilon_0)\vec{E} = \vec{P} . \tag{2.65}$$

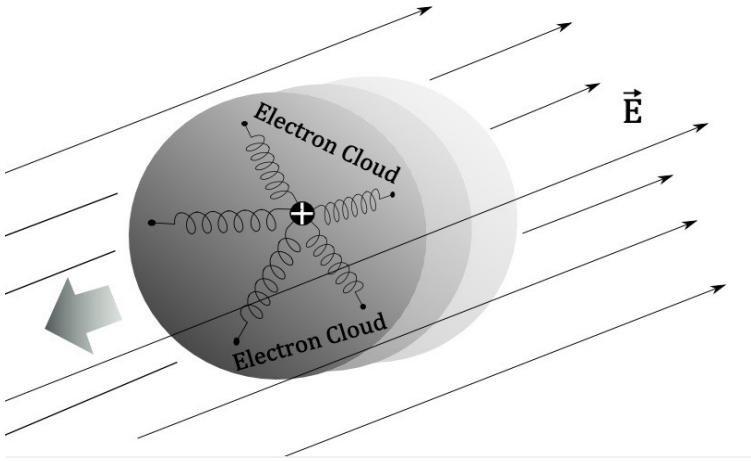

Figure 2.9: The electron cloud of an atom being displaced by an external electrical field generating a dipole.

The redistribution of charges can occur via the following mechanisms. There are molecules that have unequal sharing of valence electron and therefore have a permanent polar moment. Thermal agitation keeps molecular dipoles randomly oriented, therefore the net dipole moment of a macroscopic sample comprising many molecules is zero. But when acted upon by external electric field, the dipoles align themselves, and the dielectric takes on an orientational polarization. If there are only nonpolar molecules and atoms, the applied electric field distorts the electron field relative to the nucleus, thereby producing dipole moments called electronic

polarization. Another process that's applicable specifically to molecules is ionic polarization. Here the positive and negative ions, like for example NaCl, undergo a shift with respect to each other and induces a dipole moment. Since atoms have relative large mass and moment of inertia, they are unable to follow the varying electromagnetic field at optical frequencies. Thus, we are only concerned with electronic polarization, and a simple classical model of dispersion can be derived.

We now study an isolated atom with an electron cloud. The cloud is bounded to the positive nucleus of the atom by an electric force. We anticipate that a net force $\vec{\boldsymbol{F}}$ keeps the electron in some sort of equilibrium configuration, and when disrupted by a small perturbation, forces the system back to the equilibrium (where $\vec{\boldsymbol{F}}=0$). If the perturbation causes very small displacements, $\vec{\boldsymbol{x}}_{\boldsymbol{d}}$, from equilibrium, it is reasonably to expect the force to be linear in $\vec{\boldsymbol{x}}_{\boldsymbol{d}}$. Thus for small displacement the restoring force has the form $\vec{\boldsymbol{F}} = -k_E \vec{\boldsymbol{x}}_{\boldsymbol{d}}$, where k_E is a kind of spring constant. If the system is momentarily disturbed out of equilibrium, the system will oscillate with the natural or resonant frequency given by $\omega = \sqrt{k_E / m_e}$, where m_e is the mass of the electron. When the disturbing force is an plane harmonic electromagnetic wave, the time-varying force working on the electron are given by the Lorentz force [15]:

$$\vec{\boldsymbol{F}}_{\boldsymbol{E}} = q_e(\vec{\boldsymbol{E}}+\vec{\boldsymbol{v}}\times\vec{\boldsymbol{B}}), \tag{2.66}$$

where $\vec{\boldsymbol{v}}$ is the speed of the electron cloud. If we align the coordinate axes so that the electric field is parallel to the y-axis so $\vec{\boldsymbol{E}}=\hat{\boldsymbol{j}}\,E_y(x,t)$ we can rewrite equation (2.2) as

$$\frac{\partial E_y}{\partial x} = -\frac{\partial B_z}{\partial t}. \tag{2.67}$$

And if $E_y(x,t)$ is a harmonic plane wave we can write it as

$$E_y(x,t) = E_{0y}\cdot e^{j(\omega(t-x/c)+\phi)}, \tag{2.68}$$

where c is the speed of propagation and ϕ is the phase. By inserting this into (2.67) and simultaneous taking the integral of the resulting equation we obtain

$$B_z(x,t) = \frac{1}{c} E_{0y} \cdot e^{j(\omega(t-x/c)+\phi)} . \tag{2.69}$$

Thus we can conclude that $E_y = c\, B_z$, or more generally

$$E = v_p B . \tag{2.70}$$

Since $\vec{v} \ll c$ we can in this case simplify equation (2.66) to

$$\vec{F}_E \approx q_e \vec{E}(t) = q_e \vec{E}_0 e^{j\omega t} . \tag{2.71}$$

Including Newton's Second Law and a damping force to our oscillating system, we can describe it by:

$$q_e \vec{E}(t) - m_e \omega_0^2 \vec{x} - m_e \gamma \frac{d\vec{x}}{dt} = m_e \frac{d^2 \vec{x}}{dt^2} , \tag{2.72}$$

where the damping force $(m_e \gamma\, d\vec{x}/dt)$ is a "frictional" force, a dissipation of energy in form of random molecular motion (heat). Since the electrical field oscillates harmonically, we can "guess" a solution of (2.72) to be on the form

$$\vec{x}(t) = \vec{x}_0 e^{j\omega t} . \tag{2.73}$$

Substituting it into equation (2.72), we find that

$$\vec{x}(t) = \frac{q_e N \vec{E}(t)}{m_e(\omega_o^2 - \omega^2 + j\gamma\omega)} , \tag{2.74}$$

where there are N contributing electrons per unit volume. Combining equation (2.13), (2.64), (2.65) and (2.74) we can obtain an expression of n as a function of ω:

$$n^2(\omega) = 1 + \frac{N q_e^2}{\epsilon_0 m_e}\left(\frac{1}{\omega_0^2 - \omega^2 + j\gamma\omega}\right) . \tag{2.75}$$

This is known as a dispersion equation.

For dense substances, the effect of interactions between molecules and the local electrical field which it is immersed in must be taken account for. The electric field responsible for polarizing our molecule is called the molecular field, we will here denote it $\vec{E}_m(t)$. This is the summarized electric field produced by all external sources and by all polarized molecules in the dielectric, with exception of the contribution of the molecule we are considering.

The molecular field may be calculated by following procedures [15]: We

suppose that a thin dielectric sample surrounded by vacuum has been polarized by an electromagnetic wave, like the wave expressed by equation (2.68). We assume that the sample is so thin that the electric field component of the wave is approximately constant over the whole sample. And we therefore assume that the polarization is uniform on a macroscopic scale $(\nabla\cdot\vec{P}=0)$ and that $\vec{P}$ is parallel with the electrical field. We cut out a small spherical piece of the sample, leaving a cavity surrounding the point where the molecular field will be computed. The remaining dielectric will be treated as a continuum. Then the dielectric is put back molecule by molecule, except for the molecule at the center which we are considering. The replaced molecules are treated as individual dipoles. This procedure is only valid, if the result of the calculation is independent of the size of the cavity [15], as we will see is the case under these conditions. The molecular field can then by expressed by

$$\vec{E}_m = \vec{E}_x+\vec{E}_d+\vec{E}_s+\vec{E}_i\,, \tag{2.76}$$

where $\vec{E}_x$ is the electric field due to the electromagnetic wave, $\vec{E}_d$ is the depolarizing field due to polarization charge on the outside surface of the dielectric, $\vec{E}_s$ is due to polarization charge on cavity surface S and $\vec{E}_i$ is due to all the dipole charges inside the cavity. We are calling the macroscopic electric field in the dielectric $\vec{E}$. Since the normal component of the dielectric displacement $\vec{D}$ is continuous across the interface between the vacuum and dielectric,

$$\vec{D} = \epsilon_0\vec{E}+\vec{P} = \epsilon_0\vec{E}_x\,. \tag{2.77}$$

The depolarizing field is clearly given by $\vec{E}_d = -\vec{P}/\epsilon_0$, combining this with equations (2.76) and (2.77) yields

$$\vec{E}_m = \vec{E}+\vec{E}_s+\vec{E}_i\,. \tag{2.78}$$

The field $\vec{E}_s$ can be found by taking the integral of the polarization charge over the complete spherical surface. $d\vec{E}_s$ can be expressed by using spherical coordinates and taking the polar direction of $\vec{P}$:

$$d\vec{E}_s = \frac{-P\cos\theta}{4\pi\epsilon_0 r^3}\vec{r}\,da\,, \tag{2.79}$$

where $\vec{r}$ is the vector from the surface to the center of the sphere as shown in Figure 2.10.

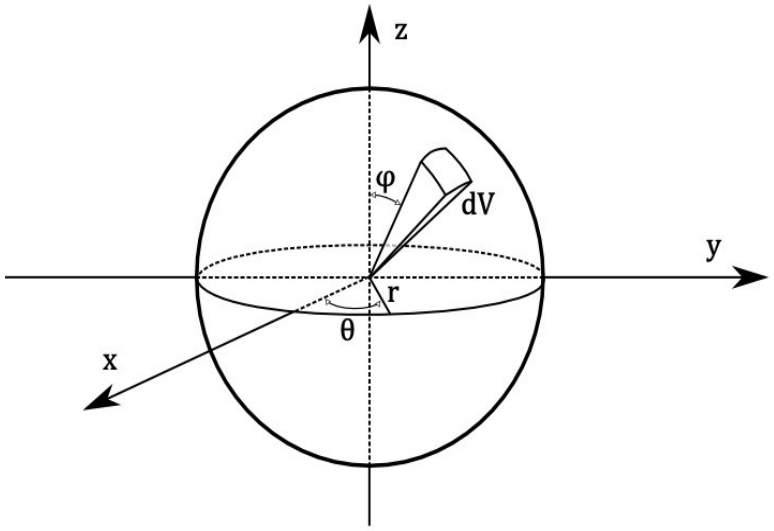

Figure 2.10: Integration of a spherical surface.

Taking the whole surface integral of this gives us

$$\vec{E}_s = \frac{1}{4\pi\epsilon_0}\vec{P}\int_0^{2\pi} d\phi \int_0^{\pi} \cos^2\theta \sin\theta \, d\theta = \frac{1}{3\epsilon_0}\vec{P}. \tag{2.80}$$

The field $\vec{E}_i$ due to the electric dipoles inside the cavity, vanishes for several important cases. A random distribution of dipoles ensures that $\vec{E}_i = 0$ [15]. This assumption holds for our situation. This and using the relation $\vec{P} = (K-1)\epsilon_0 \vec{E}$ reduces equation (2.78) to

$$\vec{E}_m = \vec{P}\left(\frac{1}{\epsilon_0(K-1)} + \frac{1}{3\epsilon_0}\right). \tag{2.81}$$

With simple algebra this can be rearranged to

$$\frac{\vec{P}}{\vec{E}_m} = 3\epsilon_0 \frac{K-1}{K+2}. \tag{2.82}$$

So by combining equation (2.75) and (2.82) we get a more valid dispersion equation

$$\frac{n^2-1}{n^2+2} = \frac{N q_e^2}{3\epsilon_0 m_e}\left(\frac{1}{\omega_0^2 - \omega^2 + j\gamma\omega}\right). \tag{2.83}$$

At frequencies increasingly above resonance the oscillator displacements will be approximately 180 degrees out of phase with the driving force. Hence the

resulting electric polarization will have the same phase as the applied electric field. Therefore will both the dielectric constant and the refractive index be less than 1. In similar manner the polarization will be nearly in phase with the applied electric field at frequencies below resonance, causing the refractive index will be greater than 1. Experiments have shown that most substances will actually undergo multiple transitions form $1>n$ and $n<1$, as the illuminating frequency increases [14]. This implicates that the system resonates at several frequencies. Thus it is reasonable to do a generalization by suppose that there are N molecules per unit volume, each with w_k oscillators having resonance frequencies ω_{0k}, where $k = 1,2,\ldots$. Thus we can extend equation (2.75) to

$$\frac{n^2-1}{n^2+2} = \frac{N q_e^2}{3\epsilon_0 m_e}\sum_k \left(\frac{w_k}{\omega_{0k}^2-\omega^2+j\gamma_k\omega}\right), \tag{2.84}$$

where w_k are weighting factors known as oscillator strengths that must satisfy the requirement $\sum_k w_k = 1$. This is essentially the same result as one would derived from a quantum mechanical treatment, with exception of the interpretation of some terms [14].

For calculating the dispersion in practical optical applications, the Sellmeier dispersion formula is used [16]:

$$n^2 = 1+\sum_{k=1}^{m}\frac{B_k\lambda^2}{\lambda^2-C_k}. \tag{2.85}$$

Here B_k and C_k are constants found empirically. This equation is a result of the same theoretical procedures as above, assuming frequency dependent oscillating dipoles. The equation is limited to situations in which absorption is negligible $(\omega_{0i}^2-\omega^2 \gg \gamma_i\omega)$, which is the case for colorless, transparent materials [14]. So the Sellmeier formula can be derived from equation (2.75), by using the relation $\lambda = 2\pi c_p/\omega$ and implement the weighting factor w_k and resonance frequency ω_{0k}. This gives us

$$n^2(\omega) = 1+\frac{N q_e^2 w_k}{2\pi c_p \epsilon_0 m_e}\sum_k \left(\frac{\lambda_{0k}^2\lambda^2}{\lambda^2-\lambda_{0k}^2}\right). \tag{2.86}$$

Thus the constants in the Sellmeier formula can be expressed as

$$B_k = \frac{N q_e^2 \lambda_{0k}^2 w_k}{2\pi c_p \epsilon_0 m_e} \quad , \quad C_k = \lambda_{0k}^2 \, . \tag{2.87}$$

Since N is the number of molecules per unit volume, and the density of the molecules depends on pressure and temperature, it is obvious that the dispersion also will depend on these parameters. A theoretical description could be made but not with sufficient accuracy, therefore empirical models are used in practice.

2.2 Refractive Index Measurement

There are several ways to approach a setup for measurements of refractive indices. For in situ usage, a sensor apparatus have to be accurate, robust and fairly immune to environmental changes. A simple method which has the potential to fulfil the mentioned requirements is refractometry. A refractometer is exploiting the phenomena described by equation (2.31) (Snell's law), by measuring the displacement magnitude of a laser beam being refracted by the measurand. The displacement of the refracted beam will be directly proportional to the refractive index. Figure 2.11 shows the principle of the refractometer and can be used as a basic for a general estimation of a sensors range and resolution [7].

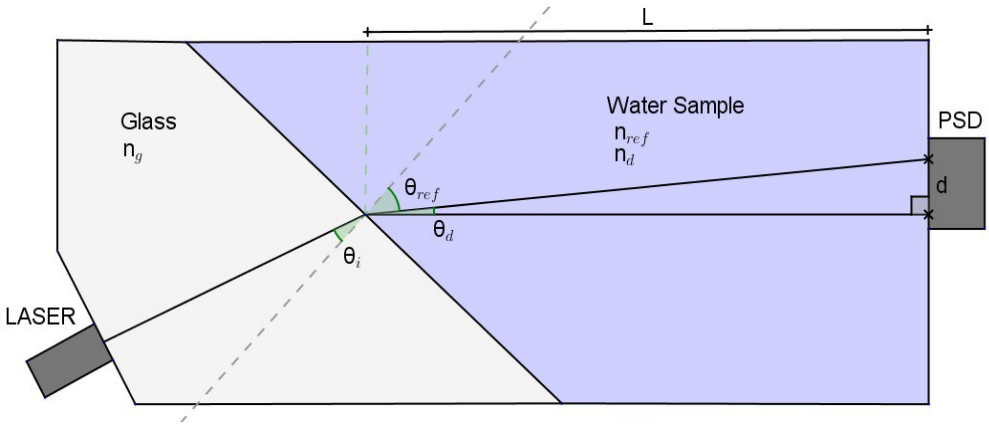

Figure 2.11: Principle of a refractometer (this figure is made for visualisation purposes and is not accurate).

By using a known water sample with the refractive index n_{ref} as a reference, a seawater sample with refraction index n_d will give a spatial detection displacement

d relative to the reference sample. The displacement d can then be related to n_d by combining equation (2.31) with simple trigonometric, which yields

$$\frac{d}{L} = \tan\theta_d = \tan\left(\sin^{-1}\left(\frac{n_g}{n_d}\sin\theta_i\right) - \sin^{-1}\left(\frac{n_g}{n_{ref}}\sin\theta_i\right)\right). \quad (2.88)$$

If the seawater sample has a maximum value of salinity and the reference sample is pure water, d will be the displacement range of the apparatus. Thus the range and resolution will depend on the laser-path length L, the incident angle θ_i of the laser at the glass-water interface, the refractive index of the glass n_g and of the properties of the PSD. Ideally one would want to achieve as low resolution as possible thus d, and therefore L should be as large as possible according to equation (2.88) and (2.89). Also should θ_{ref} be as close as possible to the critical angle between the two media. But for in situ application the construction must be a compromise between measurement quality and sensor practicality and efficiency.

Assuming that the refractometer is constructed such that the maximum displacement, D, does not exceed the detection range of the PSD, then a intrinsic resolution of refractive index may be determined by

$$\partial n = N\frac{\partial D}{D}, \quad (2.89)$$

where ∂D is the resolution of the PSD and $N = n_{max} - n_{min}$ is the range of the refractive index.

Considering that a basic refractometer (illustrated in Figure 2.11) is desired to measure refractive indices of the whole salinity scale, corresponding to $N = 0.0072$ at indoor pressure and temperature, with a resolution of $dn = 10^{-6}$. If a PSD detector with $\partial D = 0.675$ μm is used, then the minimal displacement range can be found to be $D = N\frac{\partial D}{\partial n} = \frac{0.0072 \cdot 0.675}{10^{-6}} = 4860$ μm. Using N-BK7 glass with $n_g = 1.515$ and setting a sensor size limit corresponding to $L = 100$ mm, the incident angle must be a minimum of $\theta_i = 61.24$ degrees according to equation (2.88). These parameters may be used as guide lines when designing the actual experiment setup.

There are several methods developed for measurement of refractive index,

and most of them are based on the theory and phenomena described in section 2.1 [17]. But other approaches than the refractometer seems to be too inaccurate, to bulky or sensitive to environment to be used in situ [7]. Still are some other techniques are worth mentioning since they have given valuable reference data.

One technique is the minimum deviation method, which is based on measuring the angle of minimum deviation for monochromatic light passing a prism. One variant of this method is using a hollow prism containing the liquid measurand. Figure 2.12 illustrates a simple setup, where the angle of deviation θ is at a minimum if I_1 and I_2 are equal. Applying Snell's law yields an equation relating the refractive index of the glass container (n_g) to the refractive index of the measurand (n) when the setup is situated at minimum deviation:

$$n = n_g \frac{\sin\left(0.5(\alpha+\theta)\right)}{\sin\left(0.5\,\alpha\right)} . \tag{2.90}$$

The procedure of the measurement consists of rotating the prism while the incidence of the light is constant. An PSD measures the varying displacement of the outgoing light. The output will behave like an oscillator having its peak values when the angle of minimum deviation occurs. This method has an advantage of being able of detecting large ranges of refractive indices and has been able to produce measurement with accuracy of $2.5\cdot10^{-4}$ RIU [19].

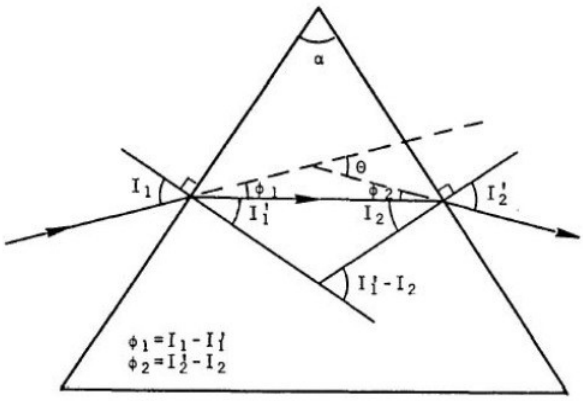

Figure 2.12: Reflection through a prism, measuring the minimum angle of deviation. [18]

Interferometric techniques are also successfully used for measurement of refractive indices, using the principle of superposition in wave nature [17] [19]. Often is a beam splitter used to split the monochromatic light source into two beam,

which will have two different paths. At the end the two beams are superimposed on each other right before detection. The detected wave will have a detectable phase difference, related to the different path lengths. Because of this ability the interferometric instruments probably have the highest potential for high sensitivity measurement, potentially up to $3 \cdot 10^{-8}$ RIU. The drawbacks of this system is very high sensitivity to geometric variations, extremely small movements of any components may give signals with magnitude many orders greater than those of the changes in refractive indices.

2.3 Conductivity Measurement

Conductivity has the unit siemens per meter (S/m) and is a measure for how well a solution conducts electricity [1]. The measurement is done by calculating the resistance of the liquid sample by inducing an ionic current through it. The sample can be thought of as a resistive element in an electric circuit setup, as shown in Figure 2.13. The ionic current depends on the total amount and flowing path of charge carriers in the measurand. The current path is determined by the sensor geometry, referred to as cell constant which has the unit of 1/cm (length/area). Dividing the liquid resistance by the cell constant results in conductivity, which is the reciprocal of resistivity. Conductivity measurements can be done in two different ways, inductive and contacting. [1]

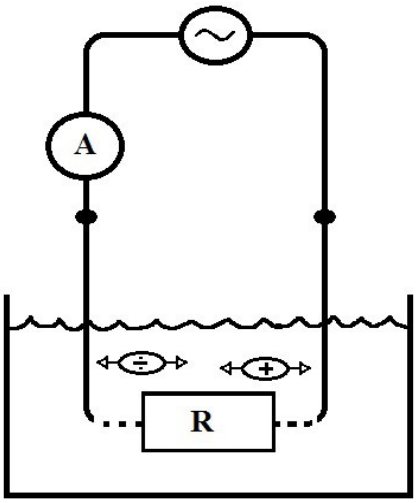

Figure 2.13: A conductivity measurement setup: an ammeter measures the current in a circuit where an AC voltage source is connected to two electrodes submerged in the measurand liquid.

An inductive sensor consists of two wire-wound metal toroids, a driver and a receiver coil, encased in a protective plastic body [1]. One toroid, the driver coil, uses an alternating voltage which induces a voltage in the surrounding liquid. This voltage causes an ionic current, proportional to the liquid conductance, to induce an electronic current in the receiver coil which is measured. The inductive sensor is ideal when the measurand is highly conductive. Since there is no need for direct contact to the liquid, samples containing high levels of suspended solids or which are highly corrosive can be measured with uppermost accuracy.

A contacting conductivity sensor consists of metal electrodes in direct contact with the measured liquid [1]. Most sensors uses two electrodes, usually made of stainless steel or titanium, though 4 electrodes can be used to give a wider measuring range. The sensor applies an alternating voltage to its electrodes. The resulting electric field causes ions in the liquid to move back and forth producing the measured current.

The most common way of in situ salinity measurements is via a CTD (conductivity, temperature and depth) sensor [20]. The sensor consists of elements sensing temperature, pressure and conductivity, as described above. Since

conductivity is nonspecific and is only a measure of the total concentration of ions in a solution, this method cannot be used to measure absolute salinity. Therefore a new unit-less measure quantity was adopted called practical salinity, referred to as S_P. Practical salinity is defined on the Practical Salinity Scale of 1978 in the terms of the conductivity ratio, denoted K_{15}, between the sample and a standard potassium chloride (KCl) solution both at the temperature of 15 °C and one standard atmosphere pressure [8]. The standard solution contains a mass fraction of KCl equal to $32{,}4356 \cdot 10^{-3}$. Practical Salinity is defined only in the range $2 < S_P < 42$ and is per definition equal 35 when $K_{15} = 1$:

$$S_P = \sum_{i=0}^{5} a_i (K_{15})^{\frac{i}{2}}. \tag{2.91}$$

where the coefficients a_i are given in appendix B. A more complex equation, applicable for oceanographic temperatures and pressures, is described in appendix B. A transformation equation for Practical Salinity to Absolute Salinity is given by

$$S_A \approx S_R = u_{PS} S_P,\ u_{PS} \overset{\text{def}}{=} \frac{35{,}16504}{35}\ \text{gkg}^{-1}, \tag{2.92}$$

where the reference seawater sample (has $S_A = S_R$) has the salinity composition described in appendix C. The accuracy of the salinity transformation will depend on the composition deviation of the measured sample versus the reference sample, though it is estimated (Millero 2008) that the absolute uncertainty of u_{PS} is minimum $\pm 0{,}007$ gkg^{-1} [8].

2.4 Instrument Components

In the next sub-sections, a thorough description of the different components used in the measurement setup is given.

2.4.1 Semiconductor Diodes

Semiconducting materials are characterized by having a temperature dependent energy gap (~ 1 eV for Si at room temperature) between their valence band and

conduction band, making them capable of acting like a conductor at high temperature and as an insulator at low temperatures. At room temperature pure semiconductors have a relative low conductivity. But by adding small amounts (0,0001 ppm) of a suited substance, called dopant, the conductivity of the semiconductor can be increased significantly [21]. If the dopant has an excessive amount of electrons after filling the valence band of the semiconductor, the superfluous electrons will increase the conductivity. This is referred to as n-doping. P-doping is when the semiconductor is contaminated with a substance containing less electrons than the semiconductor. Here "electron holes" will occur, acting as a positive charge carrier. A junction of a p-doped and n-doped semiconductor will, due to recombination of electron and electron-holes, have a depletion region at their interface. This region will be polarized and therefore have a electrical potential difference, thus the name semiconductor diode. This voltage difference is determined by the production materials of the semiconductor diode. The diode can be used for both detection and emission of light, by letting the energy gap of the voltage barrier be in the same range as the energies of light photons [22].

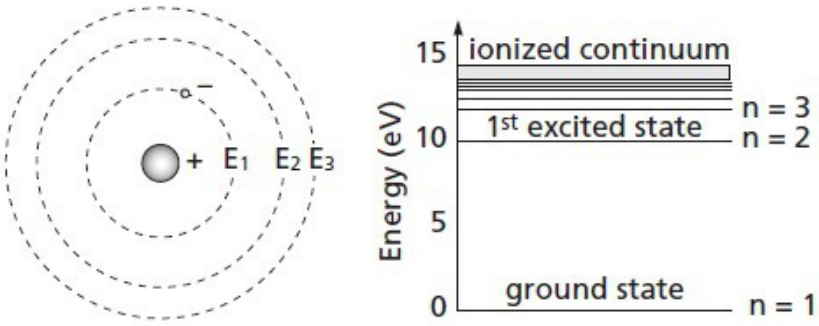

Figure 2.14: The Bohr atom and a simple energy-level diagram [24].

The energy of each photons are determined by the equation [23]

$$E = hf, \tag{2.93}$$

where h is Planck's constant and f is the frequency of the photon. By using the relations between frequency and wavelength of a electromagnetic wave in vacuum,

$c = \lambda f$, equation (2.93) can be rewritten as

$$E = \frac{hc}{\lambda} . \tag{2.94}$$

An atom has several energy states, which describes how strongly the electrons are bound to the atom. These energy states of the atom is described by quantum physics, and one energy state can only be occupied by one electron at the time. Niels Bohr was the first to describe atom's energy state with his simple model, shown in Figure 2.14. For an atom to absorb a photon, the energy of the photon must exactly match the difference between two energy states for the atom. Similar, an atom will emit a photon when an excited electron decays to a lower energy states. The energy of the photon will match the energy difference between the two states. In a semiconductor diode an electron will jump from the conducting band to the valence band or vice versa, when the diode either emits or absorbs a photon. The working photons will have the wavelength determined by

$$\lambda = \frac{hc}{\Delta E} . \tag{2.95}$$

where $\Delta E = E_c - E_v$ is the energy gap between the conducting band and the valence band.

Laser diode

A laser is a device that produces collimated light beams which are coherent, monochromatic and of high intensities [24]. A laser diode converts electricity to light directly, via the recombination process of electron and electron-holes when electrons are injected into the depletion region of the semiconductor. This process is very energy efficient, practical laser diodes may reach 50% power conversion rate which is at least an order of magnitude larger than most other laser types. Efficiency in addition to small size and low cost has made the laser diode the favourite choice in newer applications.

The most important characteristic of a laser diode is perhaps the responsivity, described by the L/I curve [25]. The curve shows the power of output light versus the input current to the device, revealing the operating range of the laser and it's

efficiency. The threshold current, denoted I_{th}, is the exact current value at which stimulated radiation occurs. At currents lower than the threshold current, there will only be small amounts of random spontaneous emissions. Another parameter influencing the slope of the L/I curve is referred to as external differential quantum efficiency (E.Q.E.). This is a percentage measurement of the amount of injected electron hole pairs converted to emitted photons. Since no real devices have an E.Q.E of 100 percentage, heat accumulation will occur in the apparatus. The wavelength of emitted photons, the threshold current, and the L/I curve slope are all temperature sensitive, as shown in Figure 2.15.

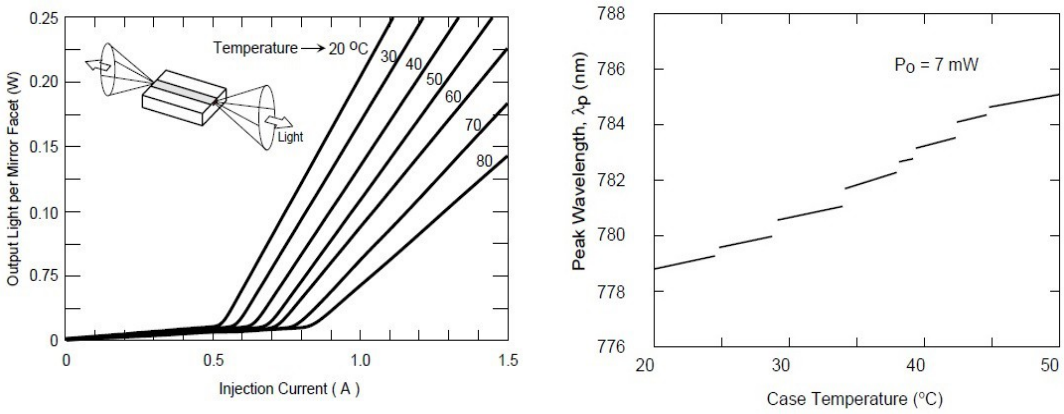

Figure 2.15: Temperature effects on the L/I curve and the peak wavelength of a laser diode [25].

Temperature sensitivity is limited by implementing distributed feedback structures or Bragg reflector structures in the laser and by using robustly made semiconductor crystals [26]. Because of these temperature effects it is clear that the system needs to be in thermal equilibrium before measurement sampling. A pulsed current source should also be considered for avoiding noise related to heating and keeping the temperature as low as possible. Lower temperature will give a better power conversion rate.

Photodiode

The photodiode generates a current related to the incident light [27]. This photocurrent consists of optical generated charge carriers generated in the depletion region and within a diffusion length from the depletion region. Silicon

semiconductors have a band gap energy of approximately 1,12 eV at room temperature, which according to equation (2.95) means that only light with wavelength of 1100 nm or shorter can be detected.

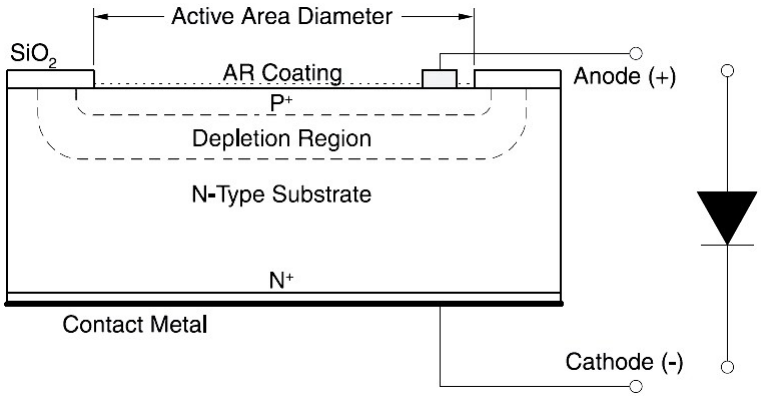

Figure 2.16: A planar diffused silicon photodiode [28].

The range of detectable wavelengths are dependent of the depth of the different layers of the semiconductor, shown in Figure 2.16, since light is absorbed exponentially with the penetrated distance. Most photodiodes can detect light with wavelengths in the interval between 400 nm and 1100 nm. The photodiode have the similar characteristics as the laser diode, like E.Q.E. and responsivity, which are all effected by temperature [28]. Therefore, the importance of thermal equilibrium during measurements must once again be emphasized. It is also beneficial (a lower Johnson noise and more stable shunt resistance) in respect to noise, to keep the temperature as low as possible when operating the photodiode. Thus using a pulsed laser when measuring may be beneficial and should be examined.

To determine a spatial position of a incident light, the position sensitive detector (PSD) must either utilizes the lateral photo effect or use several separated photodiode elements [29]. When using the lateral photo effect, the photodiode has been implemented with a thin homogeneous resistivity layer at the top of the p-layer with two or four (for detecting in 1 or 2 spatial dimensions) contacts attached to it. At the center of gravity of the incident light, a voltage arises, which in turn generates currents that flow through the contacts. The currents at the contacts will be proportional to the displacement of the incident light in respect to the center of the detector, since the resistivity of the current path is proportional to the path length.

Therefore will measurements of these currents reveal the actual displacement.

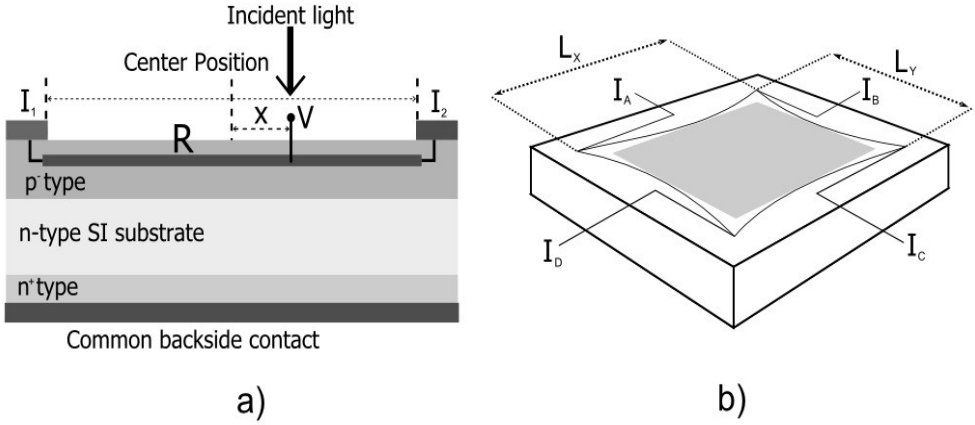

Figure 2.17: a) Schematic cross section of a Lateral Effect Photodiode.

b) 2D lateral effect sensor commonly called a "pin cushion" sensor. [28] [51]

In compliance with Figure 2.17 a), the currents at the two contacts can be expressed as

$$I_1 = \frac{V}{\int_0^{L/2+x} R \cdot dx} = \frac{V}{R(L/2+x)} \tag{2.96}$$

and

$$I_2 = \frac{V}{\int_{L/2+x}^{L} R \cdot dx} = \frac{V}{R(L/2-x)}. \tag{2.97}$$

Rearranging the equations above, gives the displacement of the light spot as

$$x = \frac{L}{2}\left(\frac{I_2 - I_1}{I_1 + I_2}\right). \tag{2.98}$$

For a 2-dimensional detector where four contacts are used, as shown in Figure 2.17 b), the displacement is expressed by:

$$x = \frac{L_x}{2}\left(\frac{(I_A + I_C) - (I_B + I_D)}{I_A + I_B + I_C + I_D}\right) \tag{2.99}$$

and

$$y = \frac{L_y}{2}\left(\frac{(I_A+I_B)-(I_C+I_D)}{I_A+I_B+I_C+I_D}\right). \tag{2.100}$$

The lateral effect sensor measure the incident light beam position independently of the beam shape and size, which maybe be useful for non-circular beams.

A quadrant detector consists of four photodiode elements separated by a small gap, with separated anode contacts and with a common cathode [27]. The incident light spot position will be determined by comparing the photo currents generated at the different segments. Since all the segments must be illuminated for acquiring a continuous position the detected range is limited by the incident beam's geometry. If the entire spot is only positioned at one segment, the position information will be quantized in steps corresponding to the segment sizes. It is only known that the spot reside somewhere on one element. The detected position will be based on the power distribution of the incident beam, thus it is important to know the beam's shape and density distribution when using the quadrant PSD. When determining the beam position, the photo currents are normalized, giving normalized coordinates via the following equations:

$$x = \frac{(A+C)-(B+D)}{A+B+C+D} = \frac{X_{Diff}}{\mathrm{SUM}} \tag{2.101}$$

and

$$y = \frac{(A+B)-(C+D)}{A+B+C+D} = \frac{Y_{Diff}}{\mathrm{SUM}}. \tag{2.102}$$

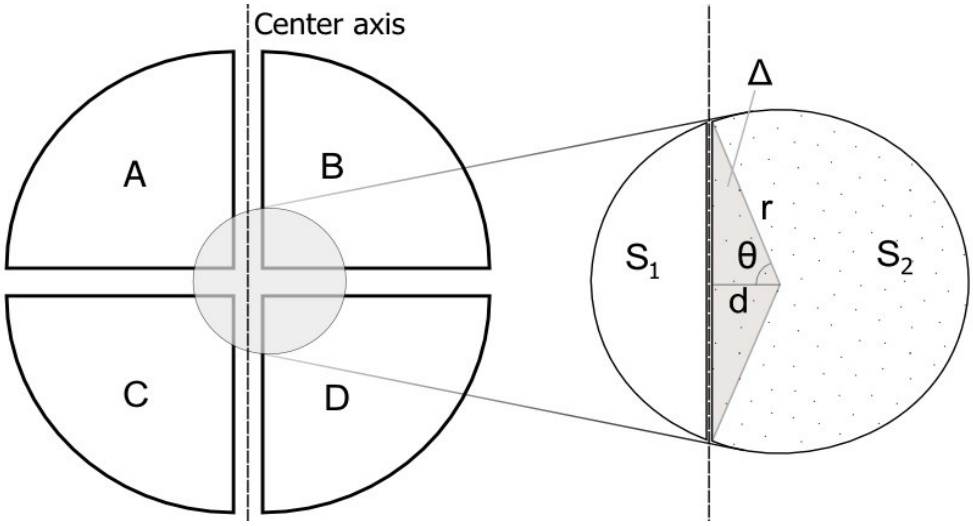

Figure 2.18: A circular beam illuminating a quadrant detector. [52]

The detector output can only be used directly if the incident beam is perfectly square shaped and homogeneous distributed. In other cases the output coordinates must be interpreted in coherence with the beam geometry. In most cases a circular beam geometry is used. The actual displacement can then be found by calculating the area of the circle-sections of each side of the center axis, assuming that the beam is homogeneous distributed. As shown in Figure 2.18 where only movements in x-direction are considered, the area of the circle-sections are given by (Seg is the area of the circles segment determined by θ [rad])

$$S_1 = Seg - \Delta = r^2\left(\theta - \sin(\theta)\cos(\theta)\right) \tag{2.103}$$

and

$$S_2 = \pi r^2 - S_1 . \tag{2.104}$$

Thus a relation, plotted in Figure 2.19, between the actual displacement and the output of the PSD can be written as

$$\frac{X_{Diff}}{\mathrm{SUM}} = \frac{S_1 - S_2}{S_1 + S_2} = \frac{2}{\pi}\left[\cos^{-1}\left(\frac{d}{r}\right) - \frac{d}{r}\sin\left(\cos^{-1}\left(\frac{d}{r}\right)\right)\right], \tag{2.105}$$

where the relation $\theta = \cos^{-1}(d/r)$ has been used.

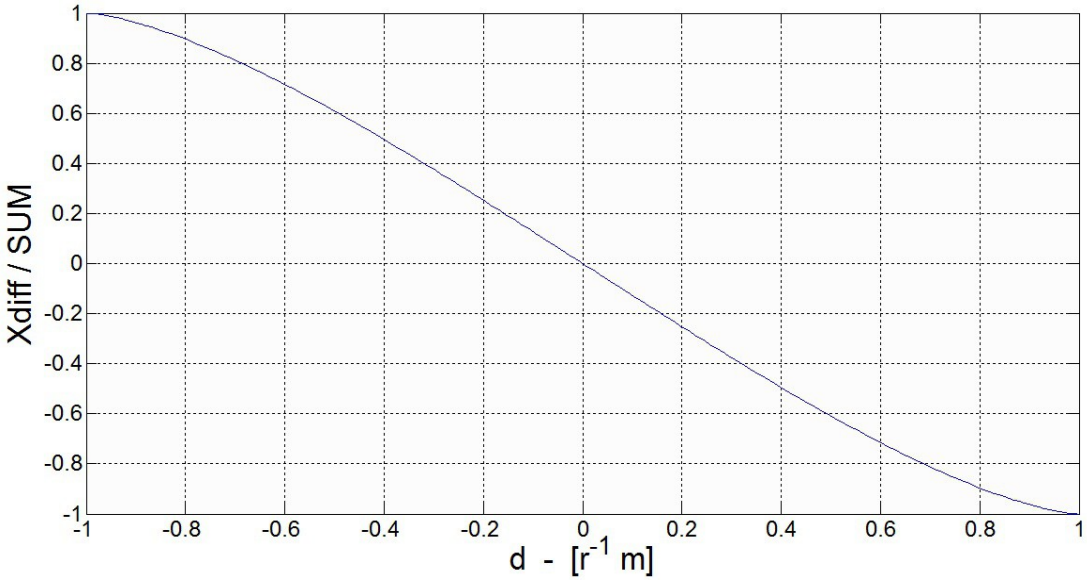

Figure 2.19: Real displacement of a circular beam versus quadrant PSD output displacement.

2.4.2 NTC Thermistor

Thermistors are resistive elements made from semiconductor material having a resistance strongly related to temperature [30]. This R-T relation is explained by band gap theory as mentioned in section 2.4.1 . The internal heat in the semiconductor makes electrons jump from the valence band to the conducting band, causing the resistance to decrease. Thus the name negative temperature coefficient (NTC) thermistor. The R-T relation is highly non-linear and is most often modelled by the Steinhart-Hart equation [31]

$$\frac{1}{T} = C_1 + C_2 \ln(R) + C_3 \ln(R)^3 , \qquad (2.106)$$

where T is absolute temperature in Kelvin, R is the thermistor resistance in ohms and C_1, C_2 and C_3 are thermistor constants. By finding the thermistor constants with proper calibration, the Steinhart-Hart model is expected to give a temperature accuracy of $\pm 0.02\,°C$. Since resistance can not be measured directly, the thermistor has to be connected to an electrical circuit. A popular way to measure the resistance is to implement the thermistor in a deflection bridge, which can be configured to give an linear voltage output in a given temperature range.

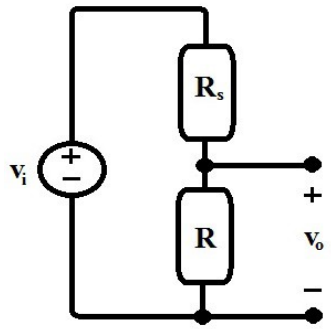

Figure 2.20: A simple voltage divider circuit.

The simplest way of measuring the thermistor resistance is using a voltage divider circuit [32]. Though by using a voltage divider the output will still be nonlinear, the output range slope can be controlled to some extent by the voltage source and the supplemented resistance. Using a setup as shown in Figure 2.20, the measured output voltage will relate to the thermistor resistance in the following way:

$$v_o = v_i \frac{R}{R+R_s}, \tag{2.107}$$

where v_o is the voltage over the thermistor, v_i is the source voltage, and R_s is the resistance of the supplemented resistor element. Combining the equations above gives a direct expression for temperature:

$$T = \frac{1}{C_1 + C_2 \ln\left(\frac{R_s}{\frac{v_i}{v_o}-1}\right) + C_3 \ln\left(\frac{R_s}{\frac{v_i}{v_o}-1}\right)^3}. \tag{2.108}$$

2.4.3 N-BK7 glass

The dispersion of optical glasses is governed by the Sellmeier equations described in 2.1.5 . Figure 2.21 shows the dispersion in N-BK7 glass where equation (2.85) is used, with coefficients values given in appendix A. For light with wavelength 635 nm the refractive index is 1.515, with a gradient of

$\frac{dn[RIU]}{d\lambda[\mu m]} = -3.4 \cdot 10^{-5}\ [\mu m^{-1}]$. According to equation (2.88) a drift in laser wavelength with magnitude of 1 nm will cause a displacement error of 6.7 μm in the basic refractometer setup described in 2.2. Thus the wavelength of the operating laser should be known accurate to a level of less than 0.1 nm, corresponding to a negligible error of 0.67 μm caused by dispersion in the glass.

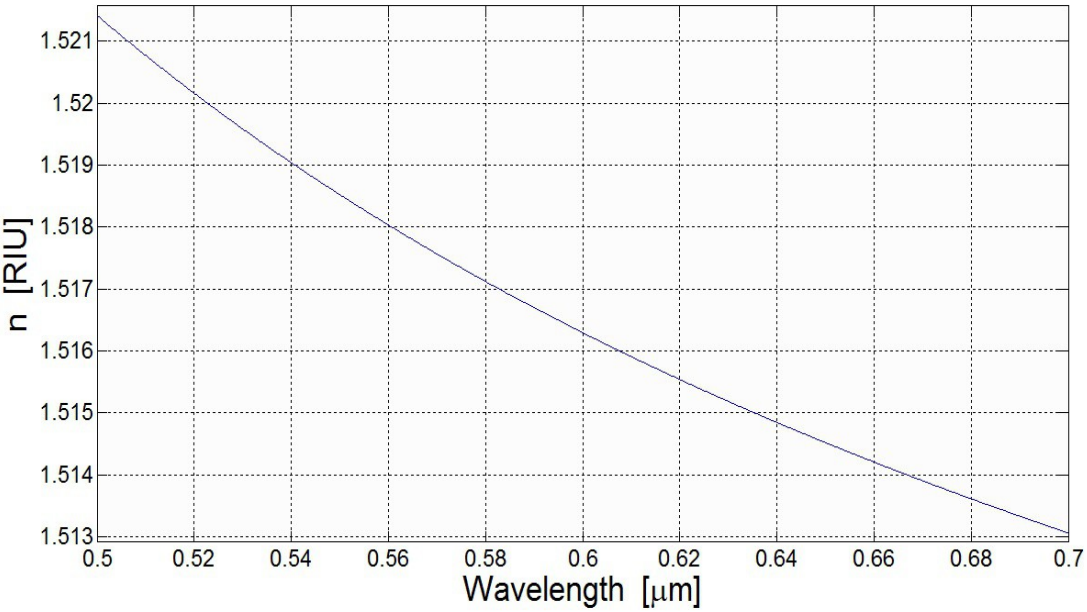

Figure 2.21: RIU of N-BK7 glass where λ *is in the interval* $[0.5,0.7]$ *μm.*

The dispersion of optical glass is also temperature dependent to some degree. The following temperature dependent equation of dispersion is empirically derived [33]:

$$\frac{dn(\lambda,T)}{dT} = \frac{n^2(\lambda,T_0)-1}{2n(\lambda,T_0)}\left(D_0+2D_1\Delta T+3D_2\Delta T^2+\frac{E_0+2E_1\Delta T}{\lambda^2-\lambda_{TK}^2}\right), \qquad (2.109)$$

where n is the refractive index given by equation (2.88) at standard temperature $T_0=15^\circ C$, $\Delta T=T-T_0$, and D_i, E_i, and λ_{TK} are constants (given in appendix A). Figure 2.22 shows the refractive indices of N-BK7 glass over the oceanographic temperature range for light with 635 nm wavelength. The temperature gradient at 23 °C is $\frac{dn[RIU]}{dT[^\circ C]} = 1.37 \cdot 10^{-6}\ [^\circ C^{-1}]$, thus it is only necessary with compensation for avoiding error in the basic refractometer setup if temperature deviates with more than one degree Celsius.

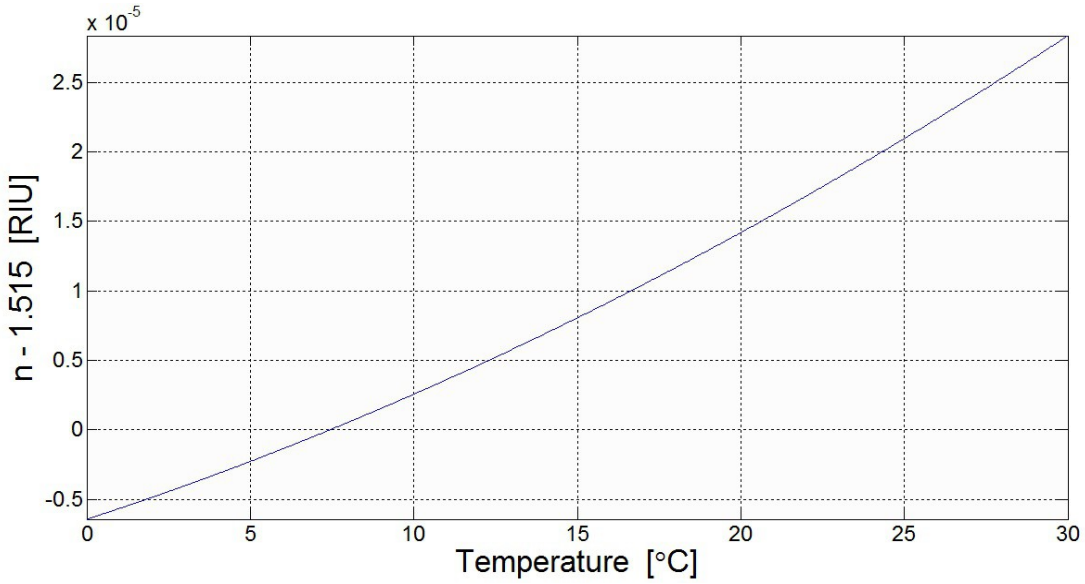

Figure 2.22: RIU of N-BK7 glass where $\lambda = 0.635$ *μm and temperature varies over the oceanographic range 0 – 30* °C.

Lens

Lenses are optical devices with curved shaped surfaces, making them able to either converge or diverge the light beam paths. Their attributes make them ideal to focus or collimate light. Most lenses are spherical shaped and described by their focal length, referred to as f . The focal length is a measure of how strongly the lens converges or diverges light. The ray path, shown in Figure 2.23, can with some approximation (setting $t = 0$) be described by [34]

$$\frac{n_m}{s_a} + \frac{n_m}{s_b'} = (n_l - n_m)\left(\frac{1}{R_a} - \frac{1}{R_b}\right) \tag{2.110}$$

where R_a and R_b are the curvature radiuses of the lens. Simplifying by setting $s = \infty$ yields

$$\frac{n_m}{f} = (n_l - n_m)\left(\frac{1}{R_a} - \frac{1}{R_b}\right) \tag{2.111}$$

called the *lens-maker's equation*. This equation will be used to determine

characteristics of the lens used in the refractometer setup.

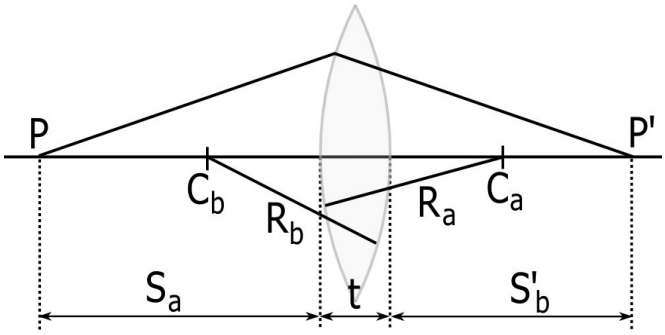

Figure 2.23: A paraxial beam travelling through a double-convex lens.

2.5 Seawater

Realisation of new optical measurement techniques for oceanography requires an accurate algorithm relating the refractive index of seawater to salinity, temperature, pressure and wavelength. One result of this demand was a 27-term index of refraction algorithm N_{MS}, elaborated in appendix A, for pure- and sea-water was developed by Millard and Seaver [35]

$$N_{MS}(T,p,S,\lambda) = N_I(T,\lambda) + N_{II}(T,\lambda,S) + N_{III}(p,T,\lambda) + N_{IV}(S,p,T). \tag{2.112}$$

The algorithm based on experimental data covers the range of 500 – 700 nm in wavelength, 0 – 30 °C in temperature, 0 – 40 psu in salinity and 0 – 11 000 decibar in pressure. The accuracy of this algorithm varies from 0,4 ppm for pure water at atmospheric pressure to 80 ppm at high pressure, preserving the accuracy of the experimental data set. The impact of the different input parameters can be investigated by varying one of them while the others are held constant.

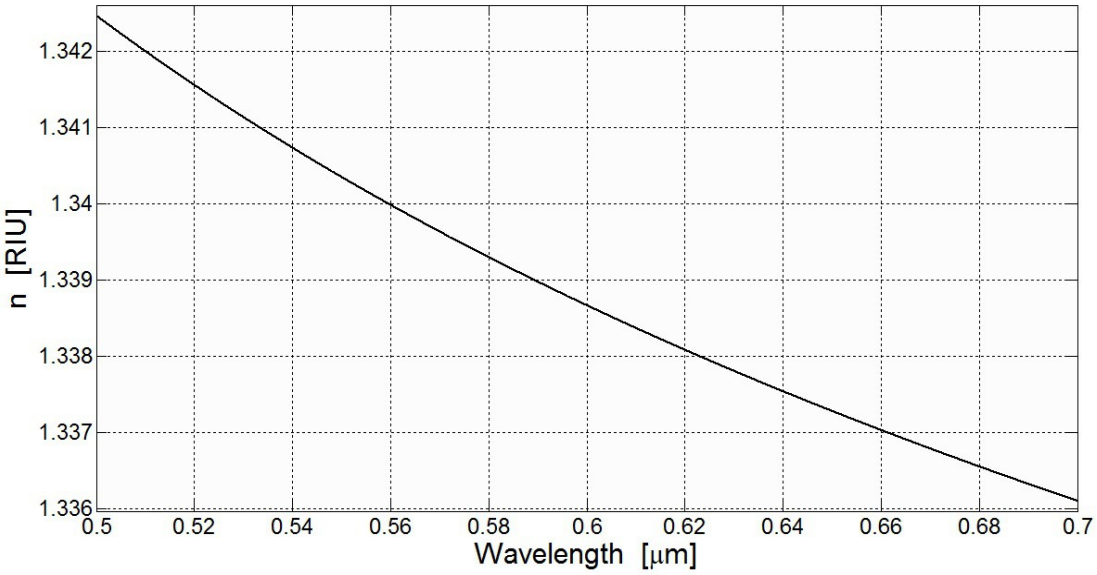

Figure 2.24: RIU of seawater when $T = 23\ °C$, $p = 0$ *db,* $S = 35$ *psu and* λ *is in the interval* $[0.5, 0.7]$ *μm.*

Figure 2.24 shows the refractive index of seawater at constant pressure, salinity and temperature while the wavelength of light varies. The RIU gradient with respect to wavelength is at 23 °C, 35 psu, 0 db and 635 nm is

$$\frac{dn[RIU]}{d\lambda[nm]} = 2.67 \cdot 10^{-5}\ [nm^{-1}].$$

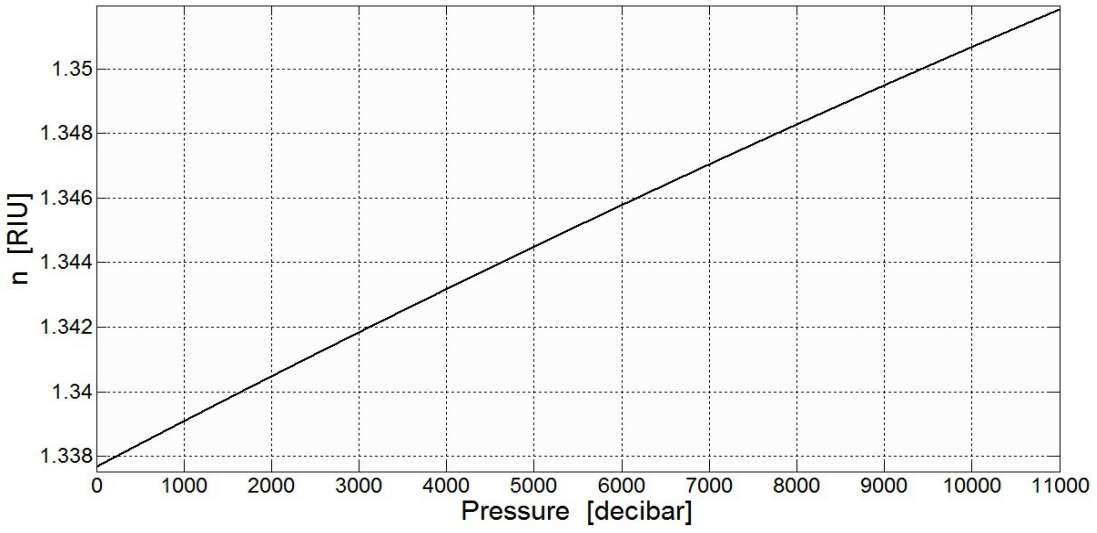

Figure 2.25: RIU of seawater when $T = 23\ °C$, $\lambda = 0.635$ *μm,* $S = 35$ *psu and* p *is in the interval* $[0, 11000]$ *db.*

At Figure 2.25 the refractive index are shown with varying pressure and with constant values for salinity, temperature and wavelength. The RIU versus pressure gradient is equal $\frac{dn[RIU]}{dp[db]} = 1.45 \cdot 10^{-6} \ [db^{-1}]$ at sea level where the pressure is 1 standard atmospheric pressure (10.13 decibar). Daily fluctuation in pressure at sea-level rarely exceeds 5 mb [36], which results in a change of $7 \cdot 10^{-8}$ RIU. Pressure changes can therefore be considered as negligible in respect to the refractive index of seawater at sea level pressure.

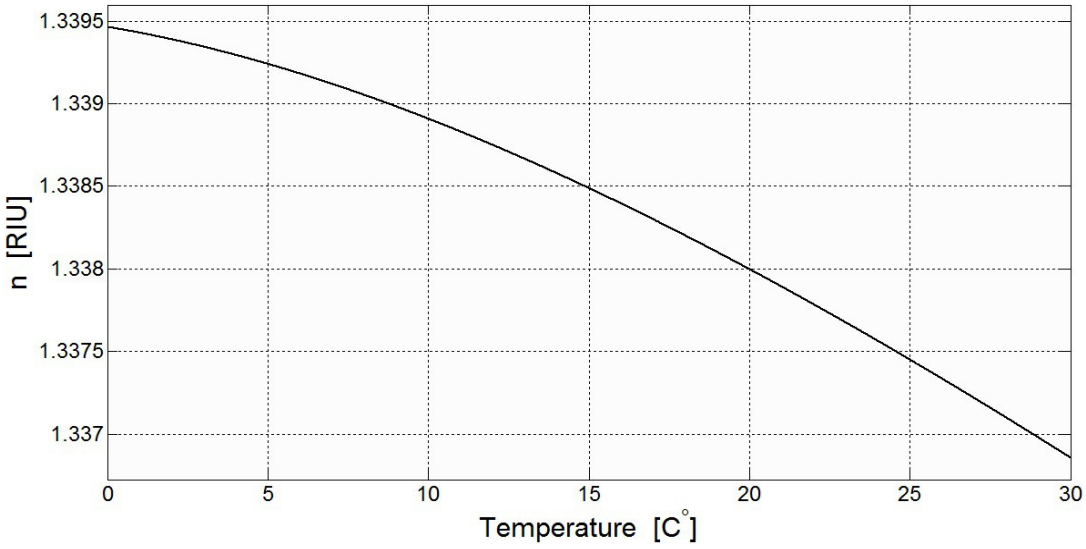

Figure 2.26: RIU of seawater when $\lambda = 0.635$ *µm,* $p = 0$ *db,* $S = 35$ *psu and* T *is in the interval* $[0, 30]$ *°C.*

The refractive index dependence on temperature is shown in Figure 2.26. The RIU gradient with respect to temperature at 23 °C, 1 atm pressure and 635 nm wavelength is $\frac{dn[RIU]}{d\,T[^{\circ}C]} = -1.1 \cdot 10^{-4} \ [^{\circ}C^{-1}]$.

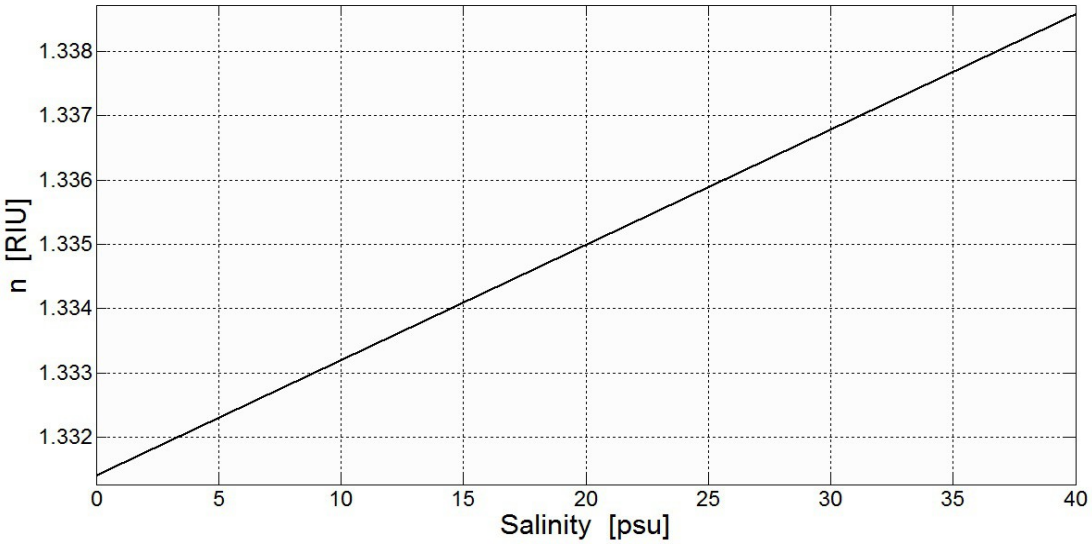

Figure 2.27: RIU of seawater when $T = 23\ °C$, $p = 0$ *db,* $\lambda = 0.635$ *μm and* S *is in the interval* $[0, 40]$ *psu.*

Figure 2.27 shows how variances in salinity impact the refractive index of seawater. The RUI gradient with respect to practical salinity at 23 °C temperature, 635 nm wavelength and 0 db pressure is $\frac{dn[RIU]}{dS[psu]} = 1.8 \cdot 10^{-4}$ and is approximately constant over the complete salinity range.

To estimate how uncertainties in the different parameters affect the accuracy of the refractive index, the following equation can be used [37]:

$$\sigma_n^2 = \left(\frac{\partial n}{\partial S}\right)^2 \sigma_S^2 + \left(\frac{\partial n}{\partial T}\right)^2 \sigma_T^2 + \left(\frac{\partial n}{\partial p}\right)^2 \sigma_p^2 + \left(\frac{\partial n}{\partial \lambda}\right)^2 \sigma_\lambda^2 . \qquad (2.113)$$

The combination of equation and the findings above suggest that when estimating seawater salinity with a accuracy of 10^{-2} psu (corresponding to 10^{-6} RIU) via refractive index measurement the wavelength, temperature and pressure should be known with accuracies of 0.02 nm, 0.003 °C and 0.4 db. Here it should be noted that the inaccuracy of the algorithm is discarded.

The water sample in this experiment will consist of distilled water with added potassium chloride in order to simulate seawater. As shown in Figure 2.27, the relation between salinity and RIU of seawater is approximately linear at an indoor environment. Since salt in seawater normally consists of 85% sodium chloride [8], it

is safe to assume that a potassium chloride solution will behave similar to seawater. Thus applying the Millard-Seaver algorithm for estimating RIU of a sodium chloride solution should give sufficient accuracy, at least at low salinity levels. The algorithm can be added a extra term, $\frac{dN_{MS}}{dS_{NaCl}} \cdot S_{NaCl} = a_{NaCl} \cdot S$, compensating for drift at higher salinity. If necessary the linear compensation term can be determined and used during the experiment. Inserting the term into equation (2.112) yields

$$N_{MS}(T, p, S, \lambda) = N_I(T, \lambda) + N_{II}(T, \lambda, S) + N_{III}(p, T, \lambda) + N_{IV}(S, p, T) + a_{NaCl} \cdot S \quad (2.114)$$

2.6 Biofouling

Biofouling is the growth of organism on structures immersed in seawater [38]. The fouling is unavoidable, and growth starts immediately after submersion and is generally divided into five main stages. At the very start of submersion there is adsorption of organic and inorganic macromolecules forming the primary film. During the middle stage the bacterial attachment is consolidated through extracellular polymer production, forming microbial film. Eventually the attachment of large marine invertebrates on the surfaces occurs.

Many oceanographic in situ sensors today are placed on piers, buoys or underwater structures and are intended for long term measurements. But most marine sensors are affected by short-term biofouling, which may disrupt the quality of measurements in less than a week. Even sensors designed with especially low fouling potential may be useless within two weeks of operation [39] [40]. Thus extra precautionary means must be made in effort to avoid fouling, leading to spending unnecessary resources on maintenance of equipment. Today (2010) there are commercially only three available biofouling protection systems for oceanographic sensors [38]:

- Purely mechanical devices such as wipers

- "Uncontrolled" biocide generation systems
- "Controlled" biocide generation systems

A mechanical protection system must be adapted to the instrument in early stages of design. This type of protection is very effective when properly integrated, and the wipers are in good condition and adapted to the geometry of the sensor. The disadvantage of this protection system is mainly the mechanical complexity, like for example ensuring motion robustness and water tightness at the axles.

"Uncontrolled" biocide generation systems are based on copper corrosion mechanism [38]. The dissolved copper ion interferes with enzymes on cell membranes and prevents cell division.

A "controlled" biocide generation system is based on chlorine evolution, either by bleach injection or electrolysis chlorination [38]. Using the bleach injection method, a reservoir for chlorine solution and pump are needed.

A combination of theses systems may also be beneficial. One existing system, "Copper shutter", uses a shutter mechanism driven by a motor that opens for measurements and closes for biofouling protection over optical windows [38]. The darkness reduces biofouling when the system is closed, and also allows biocide concentration to accumulate.

When choosing protection system for sensor it is important that the system does not affect the measurement or the environment. The system should also be reliable at all conditions, without consuming too much energy affecting the endurance of the monitoring.

3 Experiment setup

In this chapter the process of design and construction of the refractometer setup is described. The function and configuration of the setup is also reviewed.

Figure 3.1 shows a photograph of the refractometer setup were a glass tube is used as sample container and optical measurement window. The setup is working primarily by sending a laser beam through the glass tube, where it is refracted by the water sample, and then determining the laser beam displacements with a lateral PSD. All the separate parts in the setup are glued together, and all non-optical parts are handmade in PVC (polyvinyl chloride).

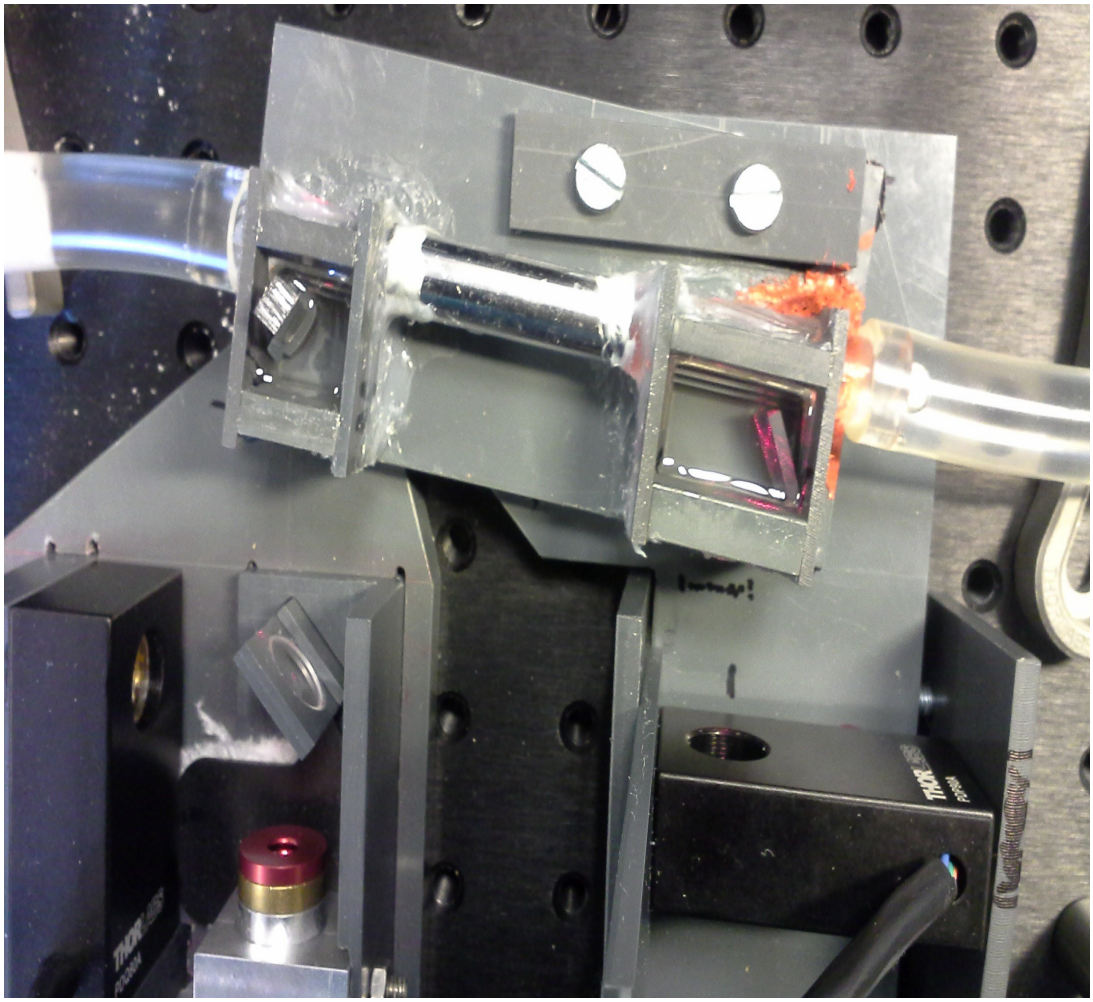

Figure 3.1: A picture of the main refractometer.

3.1 Design and construction

The priority when designing the refractometer was high robustness and practically for in situ usage. That implies long-term measurement without maintenance. A major concern for all sensors in marine environment is biofouling. Biofouling, elaborated in section 2.6, is growth of organisms and will occur on all surfaces contacting seawater. The growth starts instantaneously after submersion and corrupts measurements. Optical sensors are especially exposed because of their dependence of clean surfaces, and are therefore dependent on some sort of protection if undergoing long term operation. For optical sensors, the most efficient protection systems against biofouling are mechanical cleaning devices given that they are implemented properly. In this respect an embodiment with a sample house formed as a cylinder is preferred. A cylindrical sample container could easily be implemented with a cleaning device, such as a rotating wiper. Stress and strain due to pressure and temperature variations is also a concern that must be considered. In this aspect having cylindrical geometries will also be advantageous. Compared to box shaped geometries, expansion will be more symmetrical and linear and thus easier to predict for cylindrical geometries.

A drawback with using curved surfaces is the enhanced complexity of accurate computing and designing the optical beam path because of optical aberrations [14]. This problem can to some extent be relieved by assuming that the radius of the laser beam is infinitely small. Another major drawback of choosing an optical embodiment carved with an inner cylinder is their commercial availability. Only cylindrical tubes of glass were found available in actual sizes and varieties. Cylindrical tubes have parallel inner and outer surfaces, thus are the possible angles of a light beam limited. A laser beam traversing from the outer surface has the largest possible incident angle onto the inner surface equal to the critical angle between the cylinder and the surrounding medium. The problem is illustrated at Figure 3.2. The laser source will always be kept in space filled with air, and the critical angle of an air-glass surface is ($n_{glass} \approx 1.5$) $\theta_c = \sin^{-1}(n_{air}/n_{glass}) = 41.8$ degrees according to equation (2.46). If restricting the sensor size to ~100 mm as the basic refractometer setup in section 2.2, the critical angle must be a around 60 degrees. This is

impossible if the beam path goes directly from the laser source into the cylindrical glass tube. A possible solution to this issue is the application of a compensating medium at the glass surfaces, allowing the needed propagation angle of ~60 degrees inside the glass.

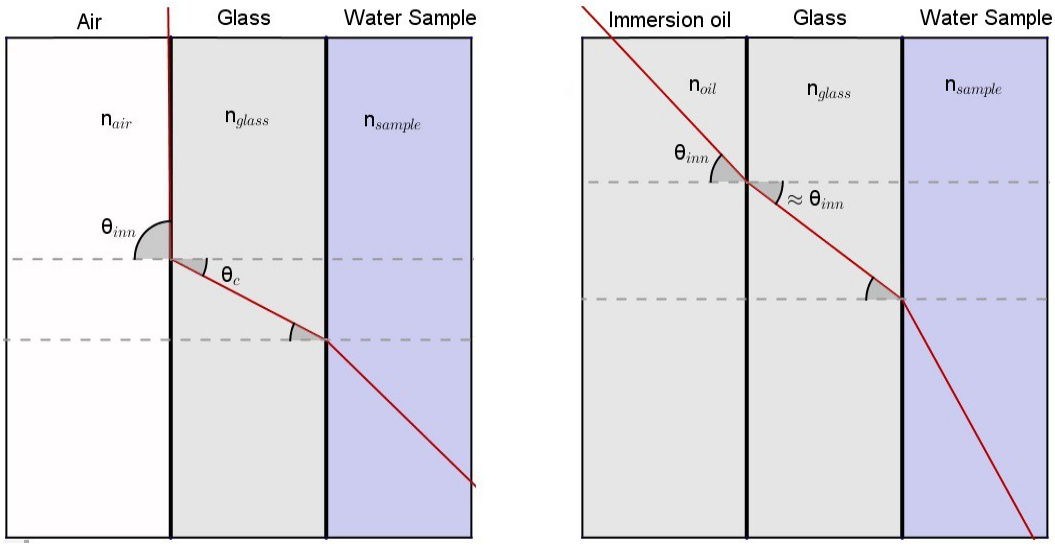

Figure 3.2: The possible angle of transmitted beam is limited when using parallel surfaces. A compensating medium, as immersion oil, will remove this restriction.

3.1.1 Refractometer design

After considering all the arguments above, a cylindrical glass tube was chosen as sample container. Mostly because of the high priority of robustness and biofouling protection of the sensor. The tube was made of N-BK7 glass and has an inner radius of 8 mm, a thickness of 1 mm and length of 115 mm. N-BK7 glass is ideal for this application because of its robustness and low thermal expansion coefficient [41]. The cylinder dimensions were imported into CaRMetal [42], an interactive geometry software which was used to create the optical design of the setup. In CaRMetal the optimal angles and positions of the different components were found after rigorous trials.

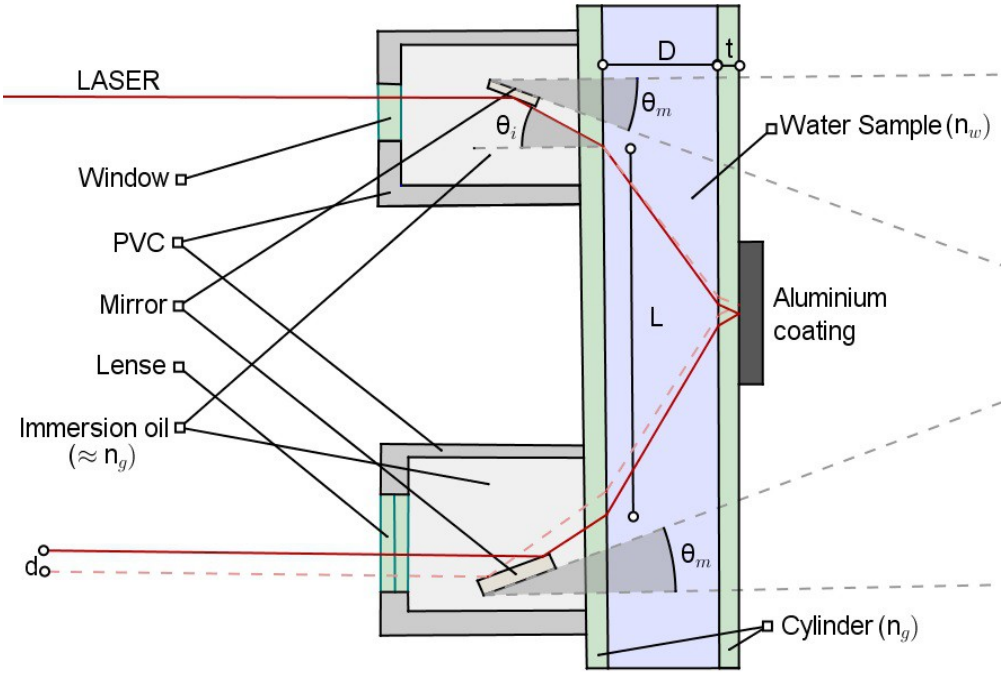

Figure 3.3: Schematic drawing of the main refractometer, not accurate. True scale drawings are shown in appendix D.

Table 3.1 : Optical parts in the main setup

Optical components	Characteristics	Model and manufacturer
Glass cylinder	N-BK7, length 115 mm, inner radius 4 mm, thickness 1 mm.	?
Window	Broadband window	Thorlabs WG40530-A
Lens	N-BK7 Plano Convex Cylindrical Lens, f = 13.7 mm	Thorlabs LJ1909L1-A
Mirrors	Broadband mirrors, various sizes	Thorlabs
Immersion oil	n_e =1.518 at 23 °C	Olympus IMMOIL-F30CC

Figure 3.3 shows a cross section of the main setup, where surface curvatures of the cylinder are neglected. At the middle of the outer surfaces of the cylinder there is a aluminium coating, which reflects the laser beam keeping it inside the cylinder. The coating has a thickness around 100 nm, and was evaporated onto the glass by a Temescal FC-2000 system [43].

The two chambers are filled with an immersion oil [44] having approximately equal refractive index as the cylinder, letting the laser beam transverse into the cylinder without changing direction. The usage of the immersion oil is only intended for microscopy applications at room temperature. All known information about the optical behavior of the used oil is shown in Figure 3.4.

Figure 3.4: The immersion oil used in the main setup.

Immersion oils degrade over time and should not be exposed to light for longer period. It is therefore clear that usage of immersion oil is not a viable solution for an in situ sensor. It was used in this thesis since desired shapes of glass containers were not available.

The laser diode used in this thesis has a beam with radius of 0.55 mm, which means that the rays at the center and edge of the beam spot will have a substantial incline deviation when hitting the cylinder surface. The beam will therefore be spread when traversing through the cylinder, though to achieve measurements with maximum resolution the beam spot should be focused to a minimum size. Thus a lens is implemented, used as a window between the immersion oil and air surrounding the detector. For minimal sensor size, the lens should have as short focal length as possible. The final lens characteristics were based on simulations performed in CaRMetal.

3.1.2 Theoretical estimation of detection

In compliance with Figure 3.3 a theoretical estimation of detected displacement can be calculated for the refractometer setup. By assuming that the immersion oil has

exactly the same refractive index as the glass cylinder, the distance L which the beam traverses vertically in the sample is determined by

$$L = 2 \cdot D \cdot \tan\left[\sin^{-1}\left(\frac{n_g}{n_w} \cdot \sin\theta_i\right)\right] + 2 \cdot t \cdot \tan\theta_i \,. \tag{3.1}$$

To relate the displacement to a specific refractive index value, a known reference value is needed. Using pure water as a reference sample, n_{ref}, a new relative ΔL can be expressed as

$$\Delta L = 2 \cdot D\left(\tan\left[\sin^{-1}\left(\frac{n_g}{n_{ref}} \cdot \sin\theta_i\right)\right] - \tan\left[\sin^{-1}\left(\frac{n_g}{n_w} \cdot \sin\theta_i\right)\right]\right) . \tag{3.2}$$

The actual displacement detected by the PSD can be expressed as

$$d = \frac{\Delta L}{\left(\frac{\tan\theta_i}{\tan\theta_m} - 1\right)} . \tag{3.3}$$

The relation between the detected displacement and RIU value of the sample are shown in Figure 3.5, and can be used to calibrate the actual setups. The input parameters to the graphs in Figure 3.5 are set to be the same as the drawing sketches in appendix D: $\theta_i = 58.1^{\circ}$, $D = 8$ mm, and $\theta_m = 29.2^{\circ}$. In the actual experiment both the incident laser angle and refractometer position were fine tuned, and are therefore not known exactly. Though equation (3.3) can be interpolated with the measurement results to calibrate and find precise characteristics of the refractometer.

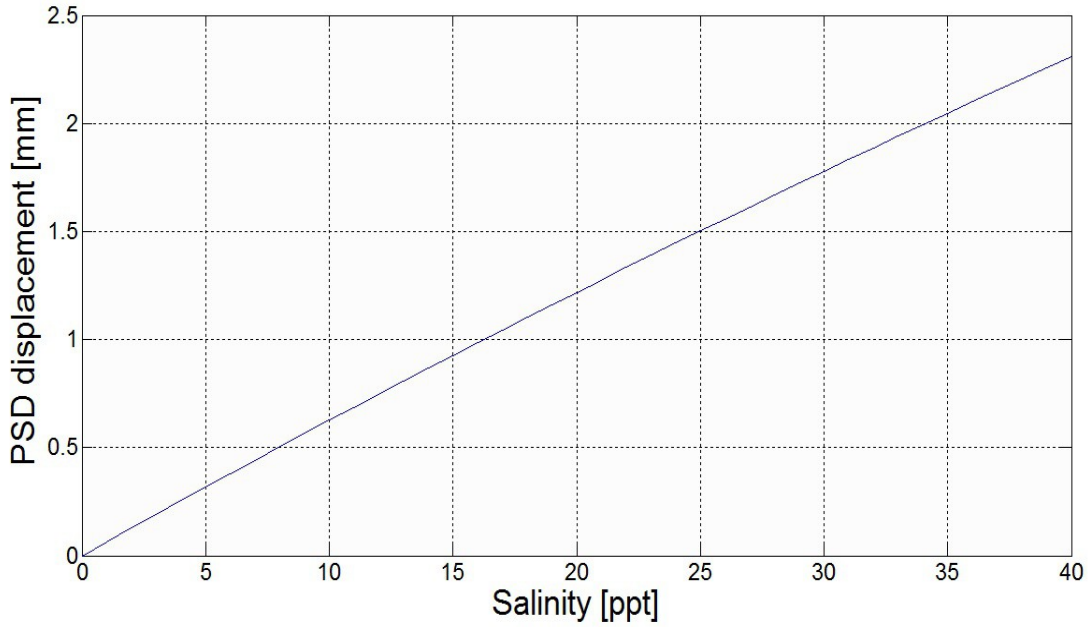

Figure 3.5: The theoretical estimated beam displacements related to the refractive indices of seawater, correlating to the whole salinity range. Parameter values used: $\theta_i = 58.1^{o}$, $\theta_m = 29.2^{o}$, $D = 8$, $n_g = 1.515$, *and* $n_{ref} = 1.3314$.

During experimental measurements it is possible to rotate the laser, when the desired angle is found the laser will be locked to a fixed direction. During long measurement sessions the incident laser angle may deviate slightly despite being in a fixed position. Therefore it is interesting to see how sensitive the measurements are to changes in the incident laser beam angle θ_i. Figure 3.6 shows a plot of the measured displacement while θ_i varies with 0.2 degrees.

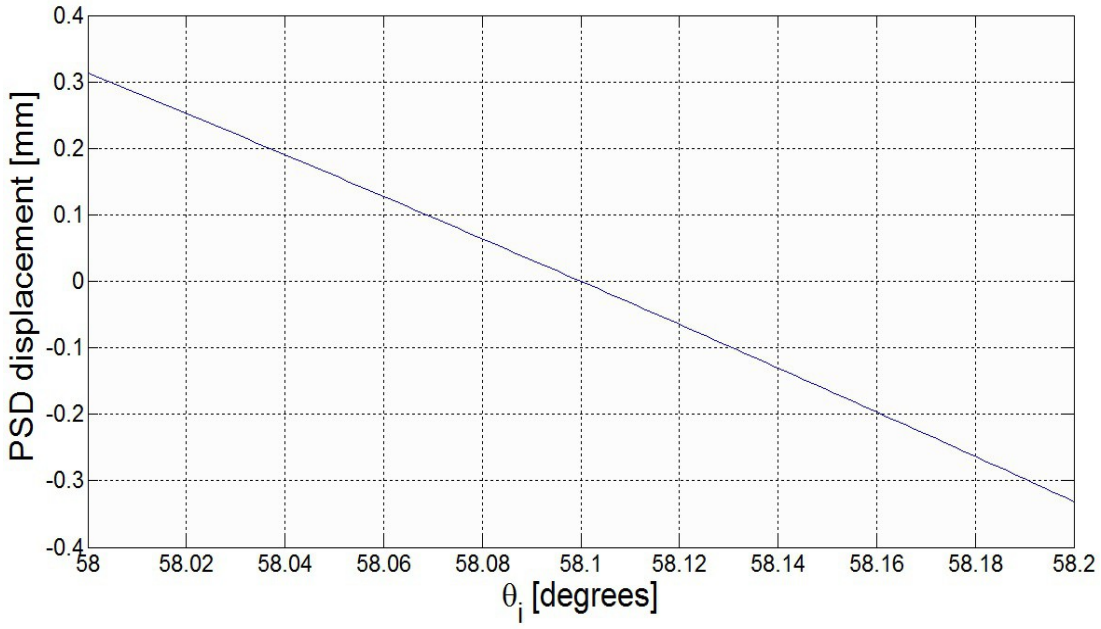

Figure 3.6: The theoretical estimated beam displacements related to changes in the incident angle when using a pure water sample. Parameter values used: $n_w = 1.3314$, $\theta_m = 29.2^{o}$, $D = 8$, *and* $\theta_i = [58, 58.2]^{o}$.

At Figure 3.6 we observe that the displacement vary with 3.5 mm when the incident angle varies wary with 0.2°. Thus the refractometer has a incident angle related gradient, $\frac{\partial \theta_i[degrees]}{\partial d[mm]} = -3.25[mm]$.

It may also be interesting to see how the mechanical parameters effect the measured displacements. In oceanographic environment pressure and temperature changes will cause stress and strain to the embodiment, changing its geometry. By varying D in equation (3.2) a change in diameter of the glass cylinder can be simulated, the resulting effect on the measured displacement is shown in Figure 3.7.

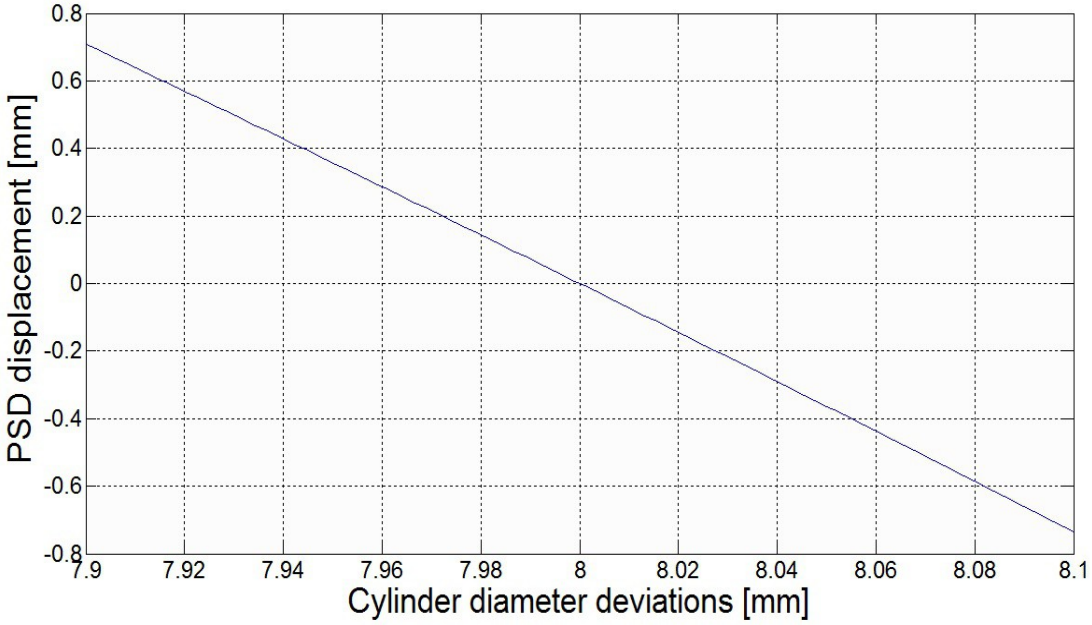

Figure 3.7: The theoretical estimated beam displacements related to changes in the cylinder radius when using a pure water sample. Parameter values used: $n_{ref}=1.3314$, $\theta_m=29.2^{o}$, $\theta_i=58.1^{o}$, *and* $D=[7.9, 8.1]$.

At Figure 3.7 we observe that the displacement vary with 10.1 mm when the cylinder diameter vary with 2 mm. Thus the refractometer has a diameter related gradient,

$$\frac{\partial D[mm]}{\partial d[mm]} = -5.05[mm].$$

3.2 Configuration

The arrangement of the whole setup is shown in Figure 3.8. Because all the non-optical parts are handmade, it is virtually impossible to directly construct the setup with necessary accuracy. Therefore some parts of the setup are possible to tweak:

- The laser source can be rotated around hit point at the first mirror, letting θ_i able to be fine tuned.
- The detector can be freely positioned to wherever giving the best detection signal.

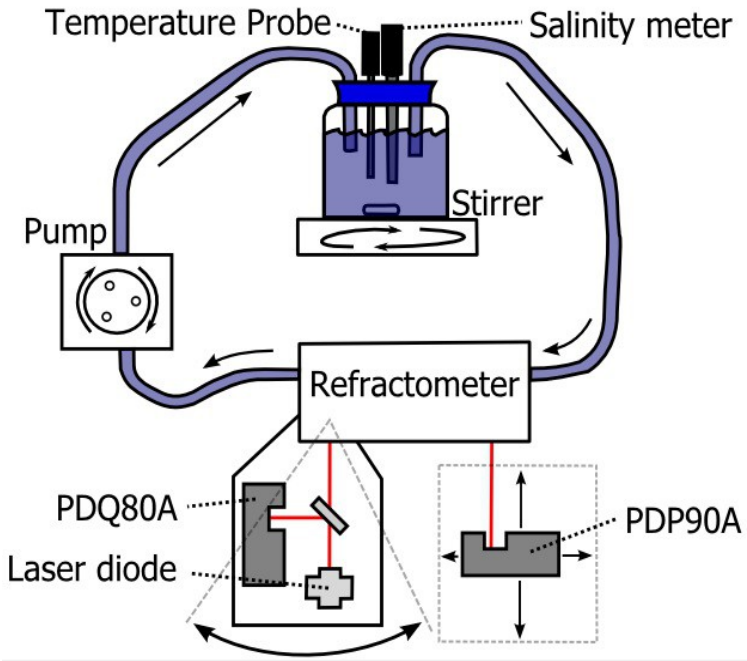

Figure 3.8: Schematic drawing of the overall measurement setup.

Table 3.3 : Components used during the experiments

Components	Model and manufacturer
Pump	Manostat Vera Varistaltic Pump Plus
Magnetic stirrer	Jenway 1000 Hotplate & Stirrer
Temperature probe	Vernier Temperature Probe
Salinity meter	Vernier Salinity Meter
Laser diode	Edmund Optics VHK Laser Diode 0.95mW
Lateral effect PSD	Thorlabs PDP90A
Quadrant PSD	Thorlabs PDQ80A
Beam splitter	Thorlabs 10:90 UVFS BS plate

In addition to the refractometer setup, a quadrant PSD, a salinity meter, and a temperature probe were used. The quadrant PSD was used to verify measurements taken by the lateral PSD, to ensure that measured displacements are caused by

refraction in the setup only. The measurements done by salinity meter and thermometer were used as reference data. When making a sample, a known quantity of water and salt was stirred together in a bottle, this way the salinity value could be determined precisely. The sample was thoroughly stirred and circulated through the refractometer, and measurement sessions where started after the salinity meter stabilized.

The salinity reference values are measured by the Vernier Salinity Sensor (SAL-TBA). The measurements are performed via the conductivity method described in section 2.3. The sensor output unit is absolute salinity, spanning the range from 0 to 50 ppt. With the accompanying acquisition gear, the sensor has a resolution of 0,02 ppt and a accuracy of $\pm 1\%$ ($\pm$ 0,5 ppt) of full-scale reading [45]. The temperature reference data is measured by the Vernier Stainless Steel Temperature Probe. The sensor uses a 20 kΩ NTC thermistor, described in section 2.4.2 , and have a range of -40 to 135 °C and accuracy of $\pm$ 0.2 °C [46].

An important parameter when collecting data is the sampling rate. If the sampling frequency is to low, different periodical signals may be undistinguishable. This phenomenon is referred to as aliasing. To reconstruct a continuous signal exactly the sampling rate must be at least twice as high as the frequency of the signal, this is known as the Shannon Sampling Theorem [47]. The measurement signal in this experiment is only noticeable affected by temperature changes, which are relative slow. Therefore the pace of sampling needs only to match the pace of noticeable temperature changes. For the salinity measurements conducted in this thesis the sampling frequency is set to 5 Hz, which is sufficient.

During this thesis the measurements samples are collected by acquisition gear accompanying the different detectors. For the salinity and temperature meters from Vernier, the Vernier LabQuest 2 apparatus was the interface between sensor and computer. The PHD 100 photo detector hub was used as acquisition device for the PSD. The data was analysed in MATLAB [48], a software specialized in numerical computation, visualization and programming.

4 Experimental results

In this chapter the raw data collected during the experiments are presented and analysed. The data are compared to theoretical estimations and used to characterise the instrument in terms of performance.

The measurement data presented in this thesis is to some degree be pre-analysed. The actual raw data has been divided and averaged to the data values presented in this thesis. Considerations around general measurement statistics are covered in appendix E.

4.1 Noise characteristics

In order to describe the refractometer precisely and to understand limiting factors of the performance, the noise influencing measurements must be mapped. The first step of the measurement system is the data acquisition card. The voltage noise addition originating from the data acquisition electronics is $< 1 \cdot 10^{-5}$ V according to manufacturer, and is therefore neglected.

Detector noise

To determine detector noise, the output from the PSD was measured in a dark environment. The measurements consists of 10 000 samples taken with 66.7 Hz, which are split in 100 batches. Figure 4.1 and Figure 4.2 shows the mean and standard deviation of the different batches.

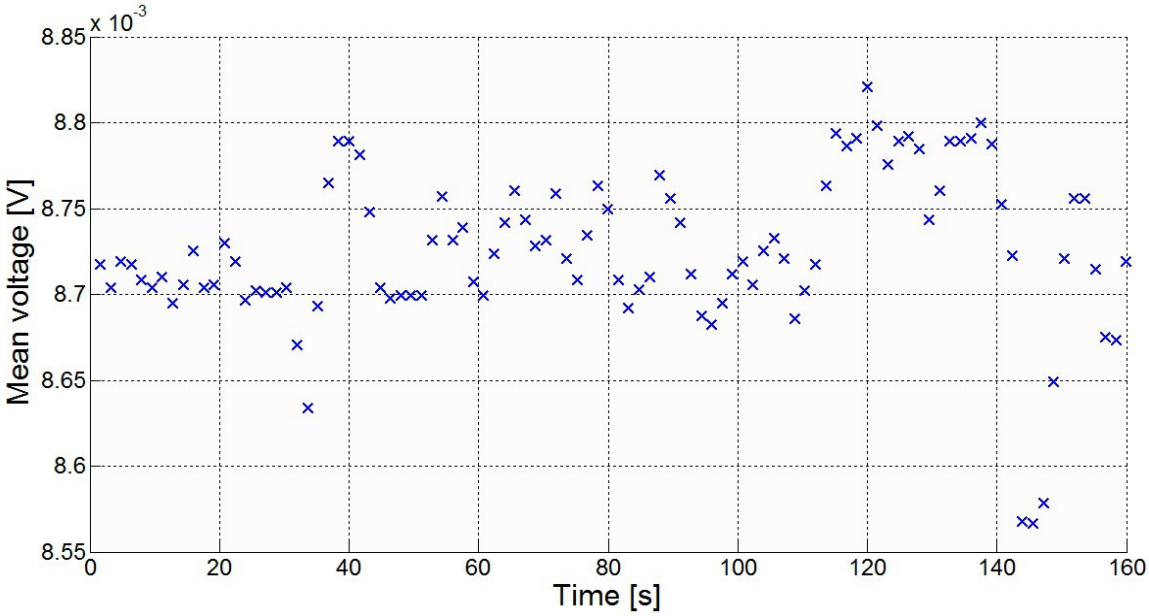

Figure 4.1: Mean values of signal from the PSD versus time.

The data plot in Figure 4.1 has an average value of $8.73 \cdot 10^{-3}$ V. The distribution of the plot looks fairly random, indicating that the noise in the signal is random.

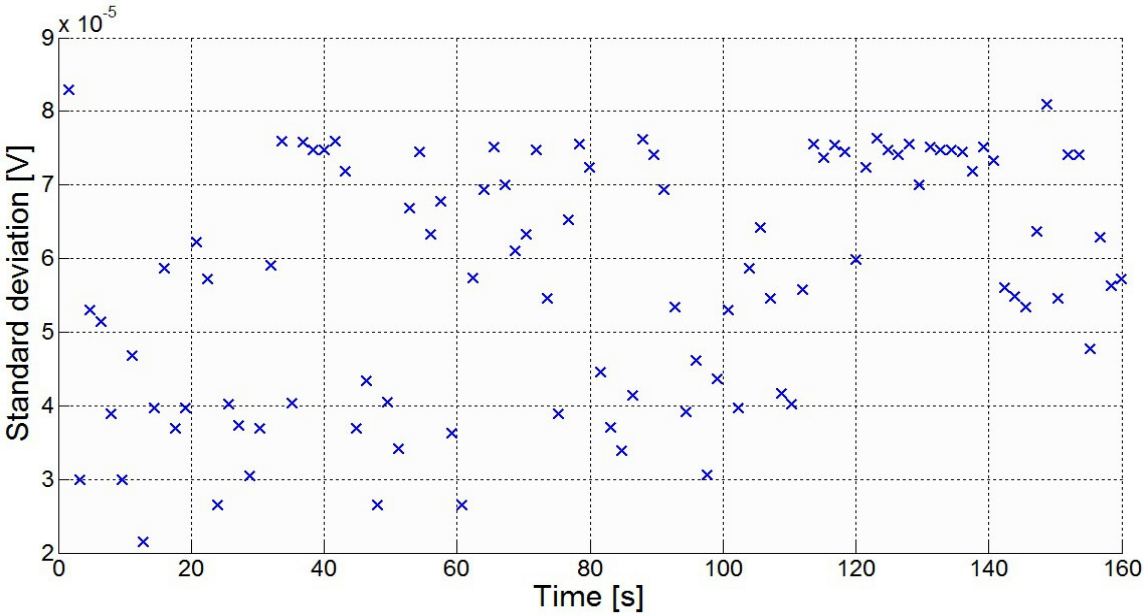

Figure 4.2: The standard deviation of signal values from the PSD versus time.

The data plot in Figure 4.2 has an average value of $4.58 \cdot 10^{-5}$ V and looks randomly distributed.

Laser noise

To determine noise from the laser, the same measurement procedure as for the detector was performed. Since the laser beam is converted to a voltage signal via the PSD, the noise in the measurement data will be the sum of both laser and detector. The mean and standard deviation of the different measurement batches are shown in Figure 4.3 and Figure 4.4.

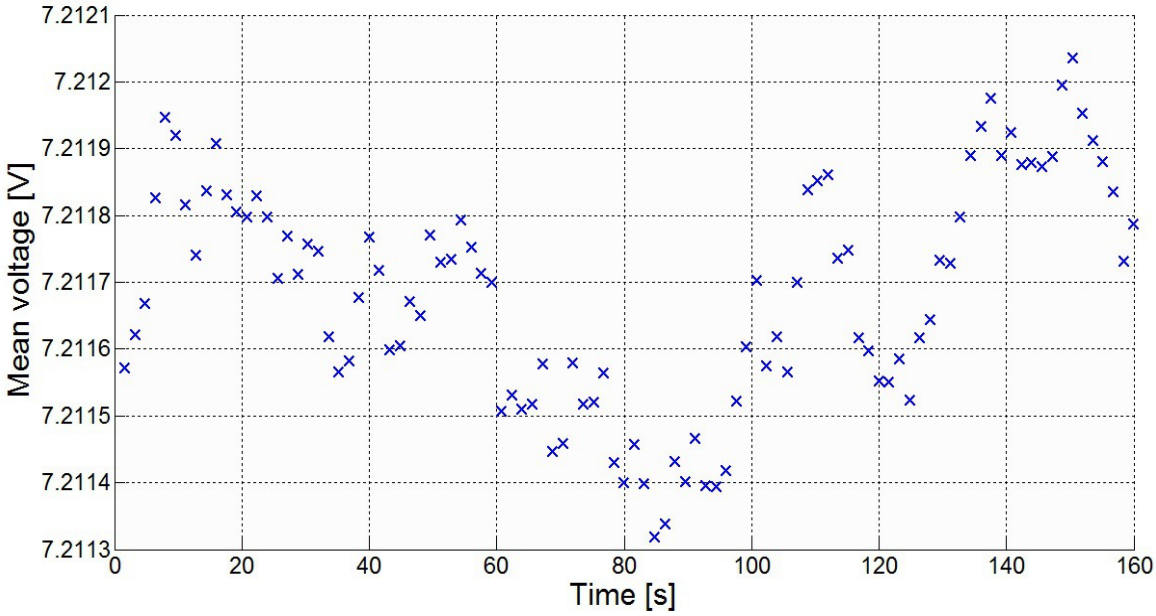

Figure 4.3: Mean values of signal from the detected laser beam versus time.

The data plot in Figure 4.3 have an average value of 7.21 V. The distribution of the plot looks fairly random, indicating that the noise in the signal is random.

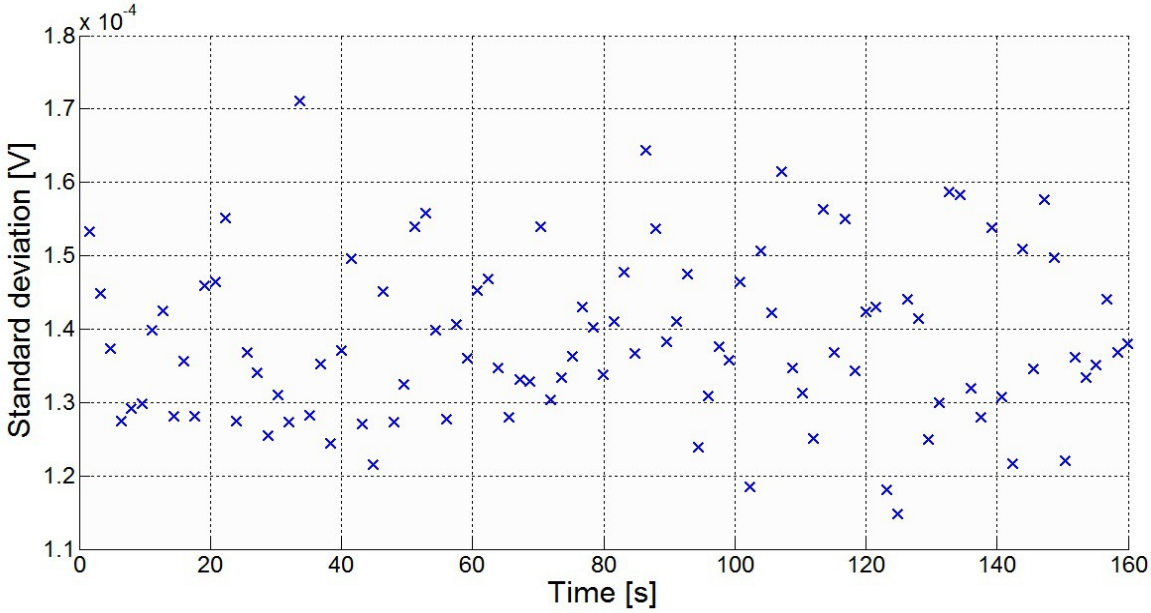

Figure 4.4: The standard deviation of signal values from the detected laser beam versus time.

The data plot in Figure 4.4 have an average value of $1.69 \cdot 10^{-4}$ V and looks randomly distributed.

Refractometer noise

Also the refractometer instruments must be investigated for noise. Even if there is no extra noise added by the instruments it is expected that laser intensity will decrease after passing through the instrument. This decrease in signal strength from the laser will decrease the signal to noise ratio. Measurements of instrument signal are represented similar as above, in mean and standard deviations of 100 batches. The measurements performed with the main instrument setup are shown in Figure 4.5 and Figure 4.6.

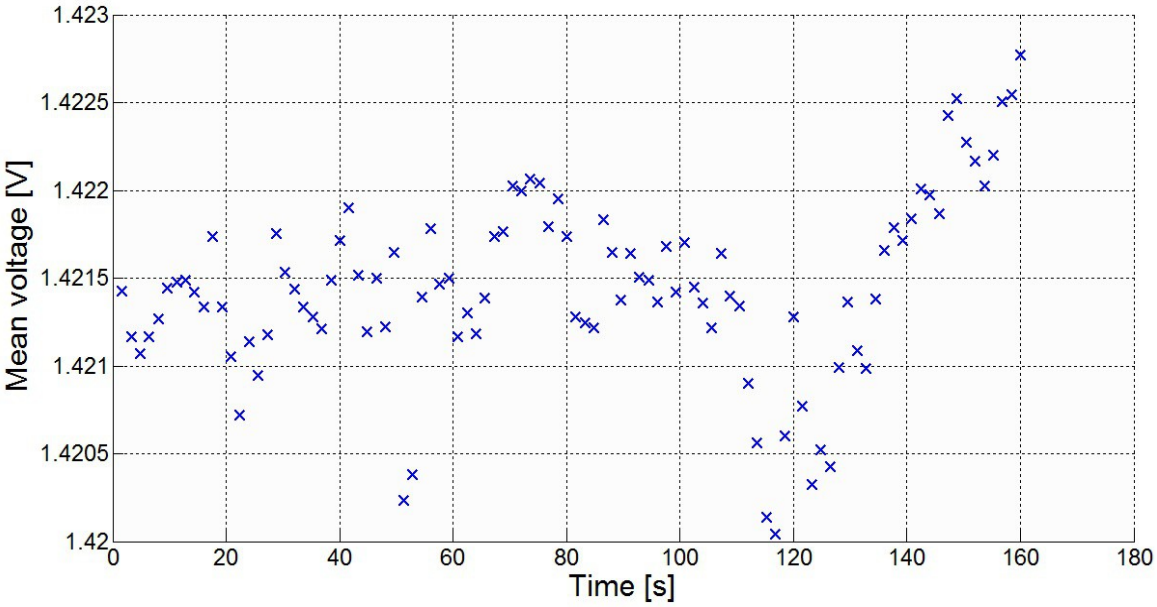

Figure 4.5: The mean values of the signal from the main setup versus time.

The data plot in Figure 4.5 has an average value of 1.42 V. The distribution of the plot looks fairly random, indicating that the noise in the signal is random.

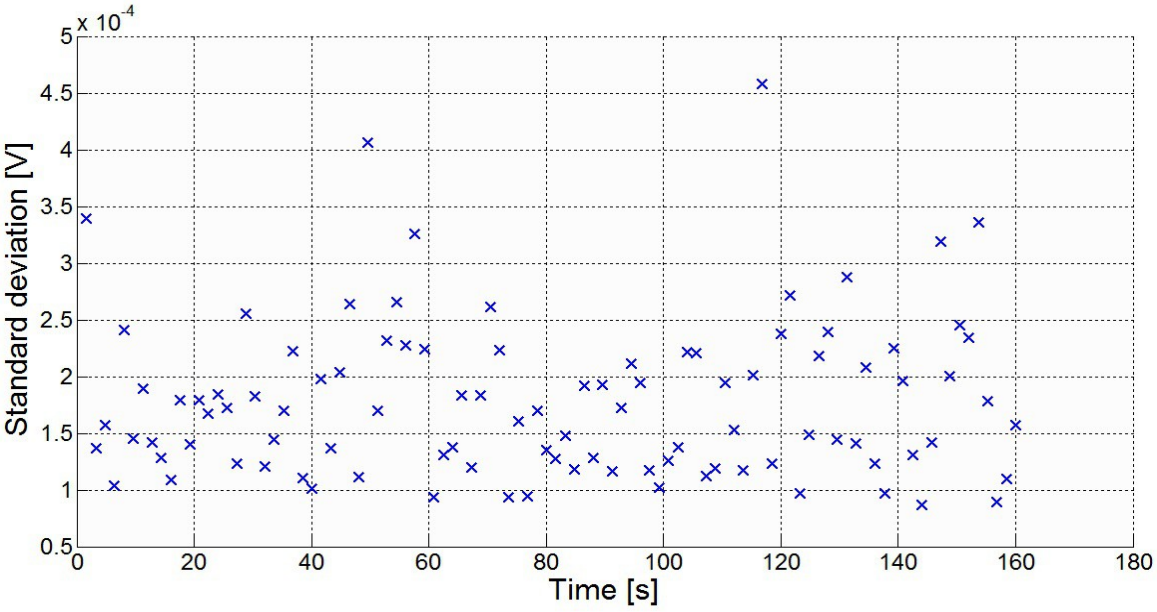

Figure 4.6: The standard deviation of signal values from the main setup versus time.

The data plot in Figure 4.6 has an average value of $5.21 \cdot 10^{-4}$ V and looks randomly distributed.

In many instruments the noise in measurement makes it hard to specify a quantized resolution value, therefore the smallest detectable change is often given in

form of sensitivity. Sensitivity is expressed as the ratio of the signal of a standard sample to the rms (root square mean) noise level, referred to as SNR (signal to noise ratio) [49].

The measurement system in this thesis is divided into three parts; the detector, the laser and the refractometer setup. From the measurements we found that the mean and noise of the different system elements to be:

Table 4.1 : Signal analysis of the setup

Element	Mean signal strength [V]	Signal noise [V]
Detector	$8.73 \cdot 10^{-3}$	$4.58 \cdot 10^{-5}$
Detector and laser	7.21	$1.69 \cdot 10^{-4}$
Detector, laser and main setup	1.42	$5.21 \cdot 10^{-4}$

If there is no correlation between the noise from theses different parts, the noise of each element can be found by [37]

$$\sigma_{tot}^2 = \sum_i \sigma_i^2 . \tag{4.1}$$

The SNR of the signal can be found by [48]

$$SNR \stackrel{\text{def}}{=} \frac{signal\ level}{rms\ noise\ level} = \frac{\overline{x}}{\sigma} . \tag{4.2}$$

By using equations (4.1) and (4.2) the following measurement system characteristics are found;

Table 4.2 : Noise and SNR analysis of setup

Element	Signal noise [V]	SNR
Detector	$4.58 \cdot 10^{-5}$	$1.90 \cdot 10^{2}$
Laser	$1.63 \cdot 10^{-4}$	$4.43 \cdot 10^{4}$
Main setup	$4.93 \cdot 10^{-4}$	$2.89 \cdot 10^{3}$

Total setup	$5.21 \cdot 10^{-4}$	$2.73 \cdot 10^{3}$

The noise measurement indicates that a short-term measurement with the refractometer setup can be made with an accuracy of $3.66 \cdot 10^{-4}$ parts per unit. This corresponds to an displacement accuracy of 3.3 μm since the total measurement range of the PSD is 9 mm, which again corresponds to a RIU accuracy of $1.00 \cdot 10^{-5}$. The actual accuracy of the refractometer setup will be determined later by salinity measurements.

4.2 Measurement of temperature variations

Since measurements of different salinities are time consuming, it is unreasonable to expect constant temperature during the measurements. Therefore measurements with different sample temperature were conducted to see how temperature changes affects the sensor, measurements were made with pure water only. The water sample was cooled down to a temperature of 4 °C in a refrigerator and was heated slowly by a hot plate to 31 °C while measuring the displacement. Though in order to avoid condensation on any optical surfaces, the measurement was not started until the water temperature reached at least 7 °C. Since the measured displacements are dependent on the how the detector is aligned, further considerations must be made when interpreting the measured displacement. When comparing the measurement values to theoretical estimations, based on the model described in section 3.1.2 , the following equation be used:

$$d' = d_0 - L, \tag{4.3}$$

where d' is the theoretical displacement used in further calculations, d_0 is a constant correlating to a reference position, and L is the length described by equation (3.1).

Figure 4.7 shows a plot of measured displacements versus temperature, included two theoretical fits. The green function is a theoretical fit where the immersion oil and the cylinder glass is assumed to have equal refractive index, the red theoretical function uses a temperature dependent value for the refractive index

of the immersion oil (only valid in the range [10 , 28] °C).

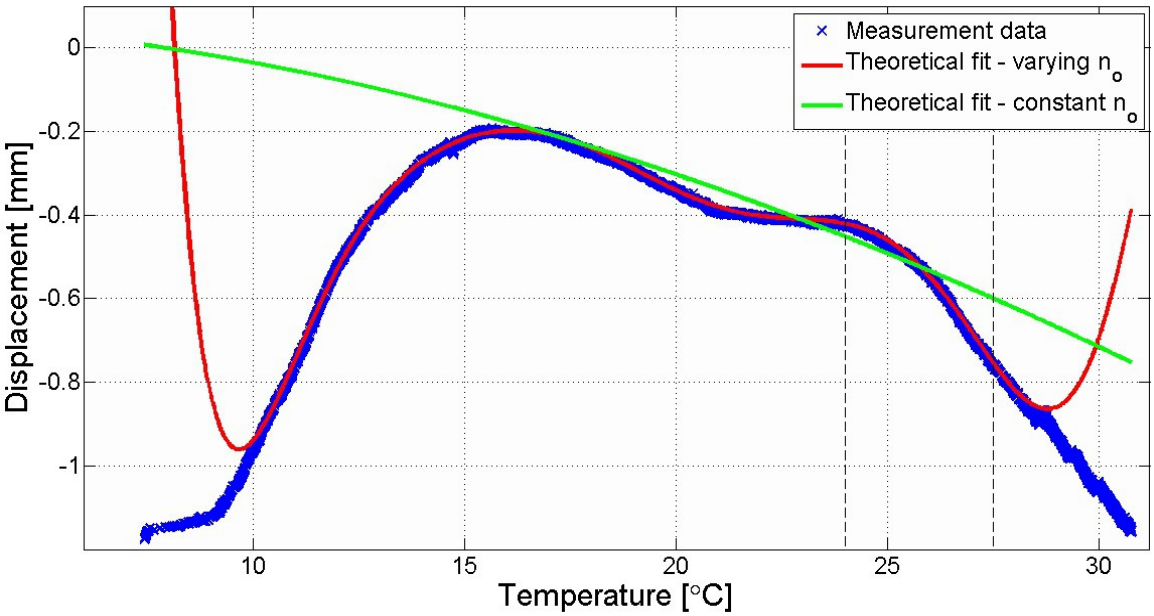

Figure 4.7: Expected displacement calculated from two fits and the measured displacement versus temperature where pure water is used.

We see there are large deviation between the measurement data and the green theoretical fit. This deviation is assumed caused by changes in the refractive index of the immersion oil due to temperature, making the assumption of a constant incident angle θ_i in Figure 3.3 faulty. This assumption is by far confirmed by temperature measurements performed with a reference setup, elaborated in appendix F. A correction can be made by including refraction at the interface between oil and glass cylinder in Figure 3.3. Thus we can rewrite equation (3.1) as

$$L = 2 \cdot D \cdot \tan\left[\sin^{-1}\left(\frac{n_g}{n_w} \cdot \sin\theta_i\right)\right] + 4 \cdot t \cdot \tan\left[\sin^{-1}\left(\frac{n_o}{n_g} \cdot \sin\theta_i\right)\right], \tag{4.4}$$

where θ_i now is the incident beam angle onto the cylinder glass and n_o is the refractive index of the immersion oil.

The three plots in Figure 4.7 are calibrated to intersect at 23 °C, since it is at that temperature the refractive index of the immersion oil is known. When calculating the theoretical estimated displacement the following parameters have

been used; $D=8$ mm, $t=1$ mm, $d_0=35.9$ mm, $\theta_i=58.6°$, and $\theta_m=29.2°$. The refractive index of the pure water sample n_w is found by the Millard-Seaver algorithm, equation (2.114). The refractive index of the N-BK7 cylinder glass is determined by equation (2.85) and (2.109), using the measured temperature as input parameter. The green plot uses the relation $n_g=n_o$. The red function uses a temperature dependent value for the refractive index of the immersion oil n_o. The values of n_o are determined by a polynomial function describing the refractive index versus temperature:

$$n_o(t) = p_1 \cdot t^9 + p_2 \cdot t^8 + p_3 \cdot t^7 + \ \ldots \ + p_2 \cdot t + p_{10} \ [mm] \tag{4.5}$$

where the different constant are given in appendix A. A fitting toolbox in Matlab was used to construct the polynomial based on n_o values found numerically. A plot of the polynomial and the numerically determined values of n_o are showed in Figure 4.8. A script in Matlab was used to find the a n_o value for each displacement measurement, by using equation (4.4) and simply searching though a large range of n_o ($=[1.517-1.521]$) and finding the value giving the smallest displacement difference.

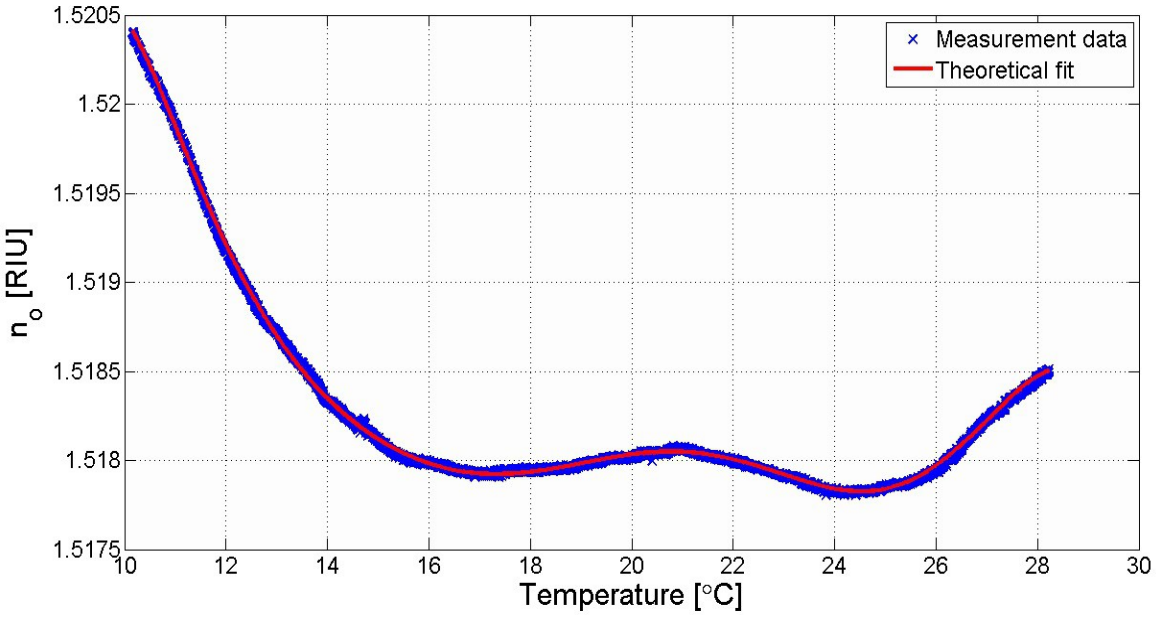

Figure 4.8: Estimated refractive index of the immersion oil versus temperature.

There are also other interesting observations made in Figure 4.7. At higher

temperature there are some discontinuities in the displacement measurements, which are better viewed in Figure 4.9. These discontinuities are hard to compensate for in data analysis and will most certainly decrease the accuracy of measurements. The discontinuities are assumed to be caused by additional reflections inside the refractometer setup. Figure 4.10 shows a fringe pattern in the detected laser spot. If one of the side peaks in the laser spot transverse in- and out-side of the detection area, there are bound the be displacement discontinuities.

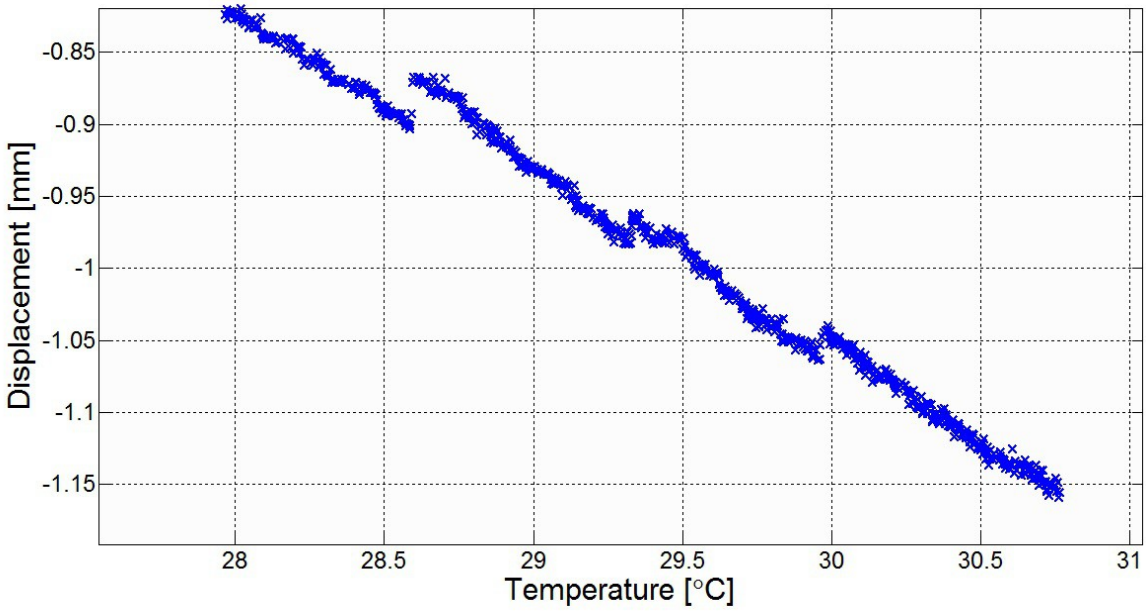

Figure 4.9: Discontinuities in the displacements detected with the main setup.

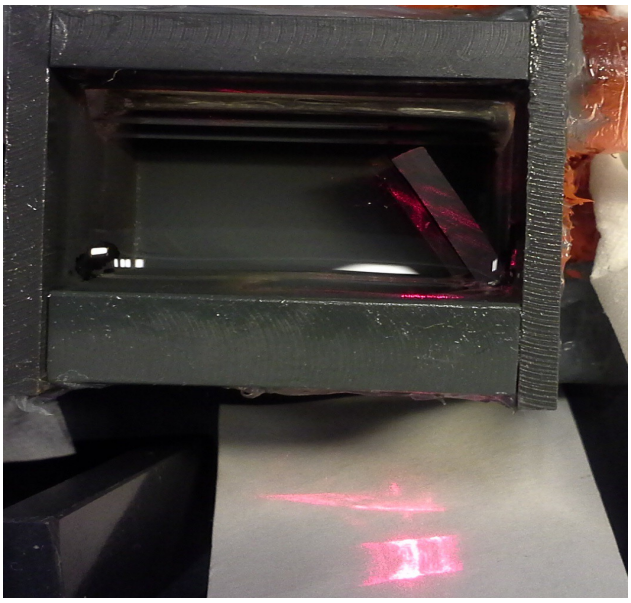

Figure 4.10: Fringe pattern in the detected laser spot in the main setup.

4.3 Results from salinity measurements

The salinity measurements consist of four equal series. In each series six different sodium chloride solutions is measured, increasing linearly from 0 to 40 ppt. Each series started with pure water, which was added an amount of *NaCl* corresponding to ~6.5 ppt. The value and accuracy of the different salinities were decided by the Vernier Salinity Meter. A batch of 1200 samples was taken with sampling rate of 10 Hz for each solution. The mean and standard deviation of each batch are plotted versus salinity. Salinity was measured with sampling rate of 2 Hz. Temperature was also measured with 2 Hz, and will be used when analysing the result.

The measurements are conducted with the refractometer setup and consist of four series of measurement conducted on six different solution spanning the whole oceanographic salinity range. Figure 4.11 shows the measurement data with a linear best fit equation found in Matlab:

$$d_{fit}(S) = -0.06383[mm\,kg/g]\cdot S + 0.6426[mm], \tag{4.6}$$

where d_{fit} is the estimated beam displacement and is S water salinity. Standard deviations of the measurement data are shown in Figure 4.12. The different temperature values during the experiment are plotted in Figure 4.13.

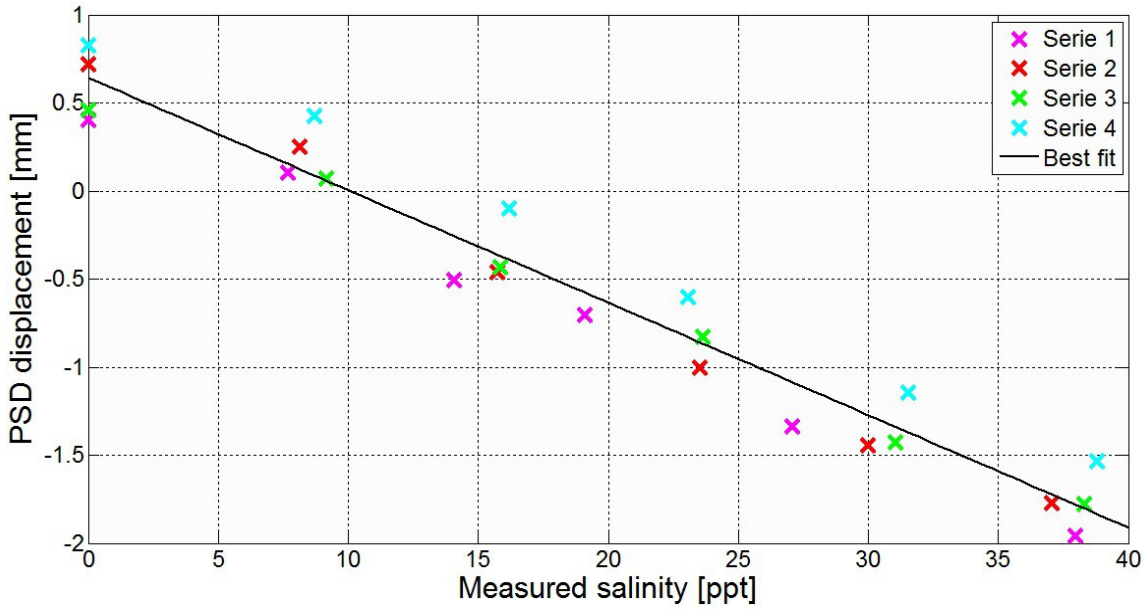

Figure 4.11: The measured laser displacement versus the measured salinity, when using the main setup.

The measurement data plotted in Figure 4.11 indicates a displacement range of around 2.4 mm. The linear fit has an error estimation of 0.1895 mm.

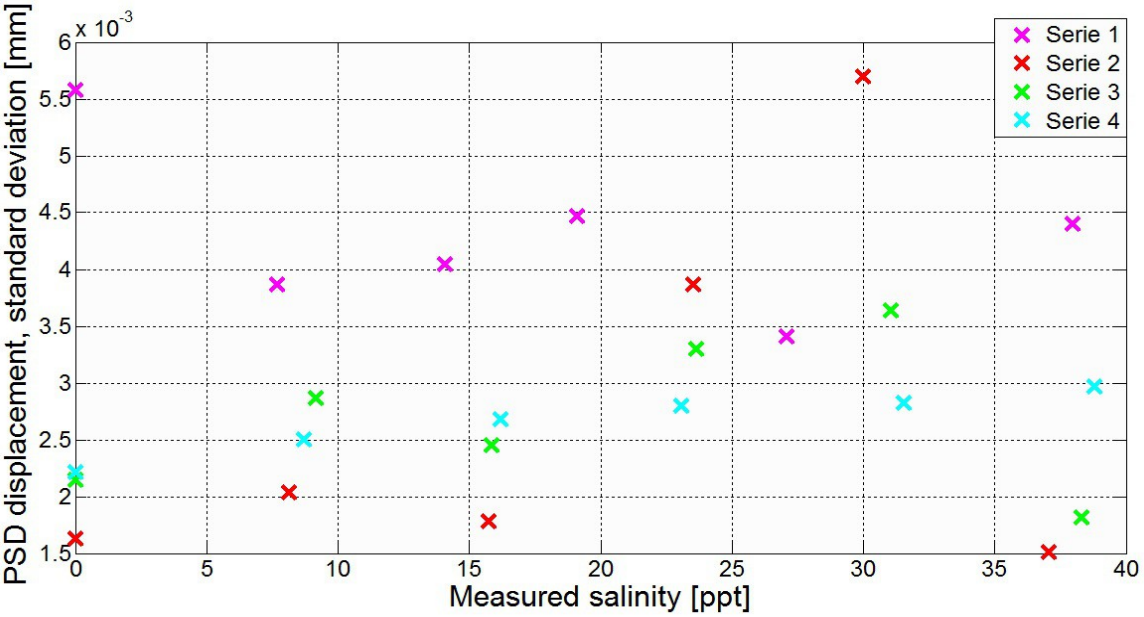

Figure 4.12: The standard deviation of the measured laser displacement when using the main setup, plotted versus salinity of water sample.

The standard deviations in Figure 4.12 have a mean value of $3.1 \cdot 10^{-3}$ mm.

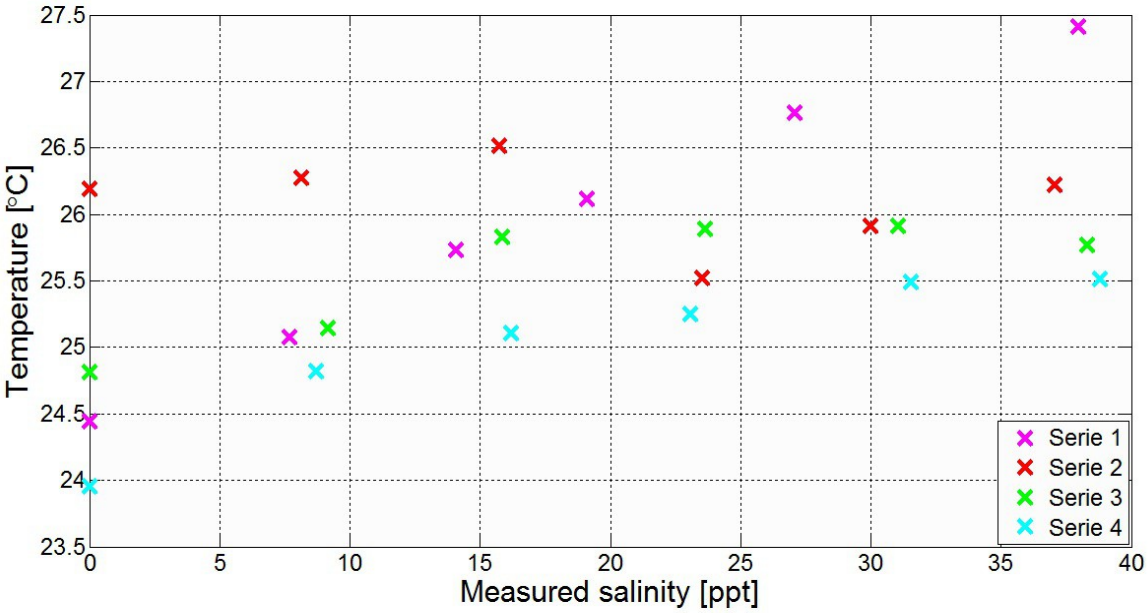

Figure 4.13: The temperature during measurement, plotted against the salinity of water sample.

The temperature plot in Figure 4.13 has a mean value of 25.65 °C.

The standard deviations shown in Figure 4.12 indicates that short-term accuracies of the measurements are at least ~3 μm, corresponding to $1.5 \cdot 10^{-5}$ RIU. The linear fit in Figure 4.11 has an error estimation of 0.1895 mm, corresponding to $5.7 \cdot 10^{-4}$ RIU. This implies that there are repeatability issues with the instrument which decreases the overall measurement accuracy. One possible reason for the increased measurement uncertainties is temperature differences in the samples. The different temperatures during the measurements are plotted in Figure 4.13, spanning over 3.5 °C and have a mean value of 25.65 °C. To investigate the temperature effect, we can look at displacement and temperature deviations relative to the linear displacement fit d_{fit} and the mean temperature. By subtracting the theoretical estimating displacement from the measured displacement and subtracting the mean temperature from the measured temperature, we can see if there is any correlation between the temperature and displacement deviations. Figure 4.14 shows the plot of the deviations included a best fit function, which can be used to compensate for the temperature variations during measurements if the correlation is significant.

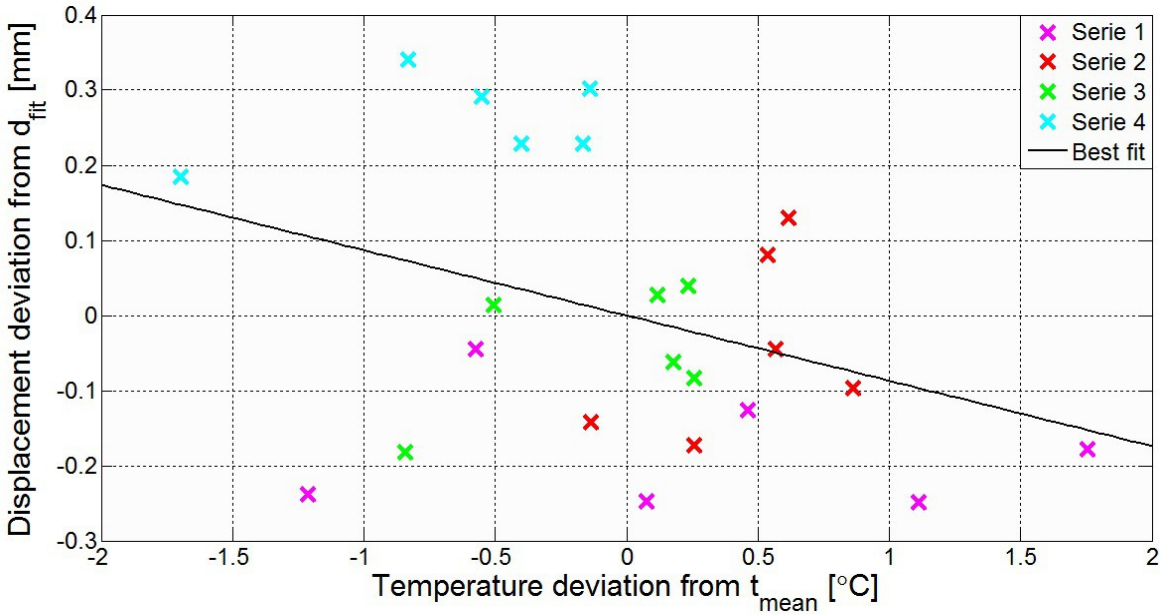

Figure 4.14: Deviations in temperatures and displacements.

The deviations in Figure 4.14 looks randomly distributed. The linear fit function in Figure 4.16 was found by Matlab and has the form:

$$\Delta d = -0.08694[mm/^{\circ}C]\cdot\Delta t + 1.225\cdot 10^{-5}[mm], \qquad (4.7)$$

where $\Delta d = d_{measured} - d_{fit}$ and is $\Delta t = t_{measured} - t_{mean}$. The function has an error estimation of 0.1770 mm, which corresponds to $5.31\cdot 10^{-4}$ RIU and is almost the same displacement error as found with equation (4.6). This implies that the repeatability issues to the instrument are mainly caused by mechanisms that are not related to the sample temperature. It should be mentioned that we only know the temperature of the water samples. The increased uncertainties may still be caused by heating processes in the laser or detector housing.

Above a pure analytical analysis of the measurement data is given. The measurement data can also be analysed with theoretical models described earlier. Since both displacements and refractive indices will depend of both salinity and temperature, comparison between these two parameters will be complex. To compare the data to the actual salinity measured by the Vernier Salinity Meter, the measured displacements are first converted to refractive indices, then to salinities. This estimated salinity can easily be compared to the actual salinity.

To convert a measured displacement to a refractive index value, an inverted

version of equation (4.4) will be used. The refractive index of N-BK7 n_g is given by combining equation (2.85) and (2.109), resulting in a temperature dependent algorithm. The refractive index of immersion oil is determined by equation (4.5). The estimated salinity is found by inverting the Millard-Seaver algorithm, equation (2.114). Figure 4.15 shows the estimated salinity plotted against the measured salinity. When calculating the estimated salinity the following parameters in equation (4.4) have been used; $D=8$ mm, $t=1$ mm, $\theta_i=58.1$ °, $\theta_m=29.2$ °, and $d_0=35.74$ mm.

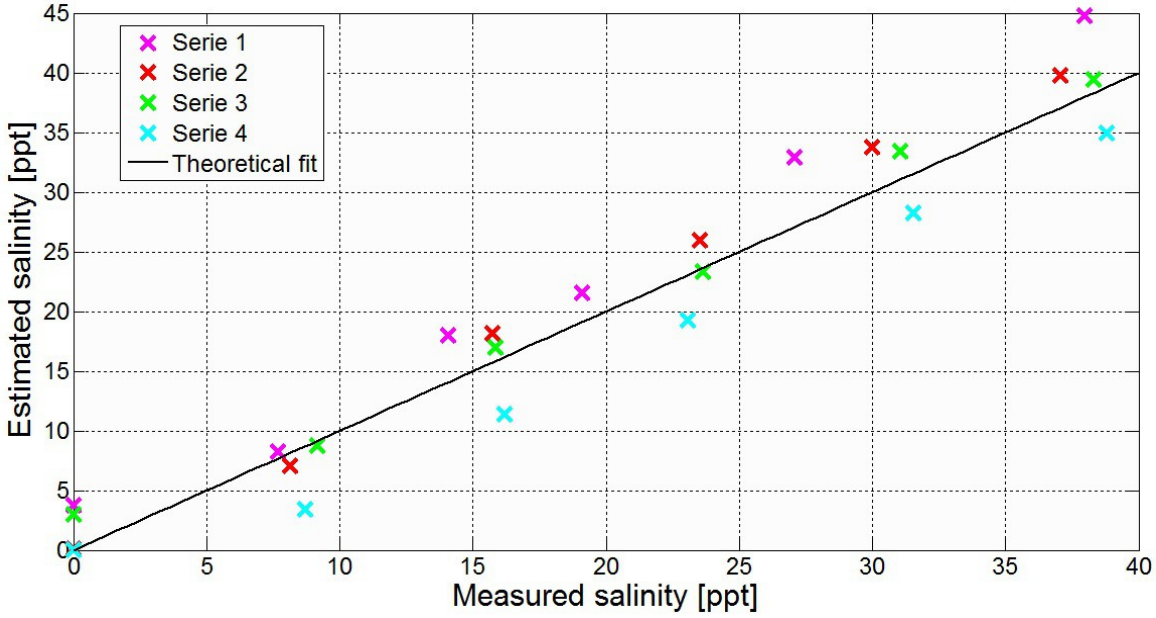

Figure 4.15: Estimated salinity, based on temperature and displacement, versus measured salinity. The following parameters are used: $D=8$ *mm*, $t=1$ *mm*, $\theta_i=58.1$ °, $\theta_m=29.2$ °, and $d_0=35.74$ *mm*.

To find the accuracy of the estimated values, the difference between the theoretical fit and the measurement data has been statistical analysed. This analysis reveals a error with a mean of $\overline{E}=2.4$ ppt and a standard deviation of $\sigma_E=1.6$ ppt, thus a salinity measurement accuracy of 1.63 ppt. This accuracy corresponds to an intrinsic refractive index accuracy of $2.9\cdot10^{-4}$ RIU.

As shown above, neither analytical nor theoretical analyses can compensate for the large displacement variations experience at the different measurement series. It has been concluded that temperature independent processes mainly cause these displacement variations. A plausible reason that may cause extra displacement is small changes in the position and direction of the tweakable components in the instrument. As shown in section 3.1.2 , minor changes in θ_i can give large displacements. Drifts in the laser and detector caused by heating processes may also cause deviations in displacement measurements.

5 Discussion and conclusion

In this chapter is the performance of the instrument setup discussed. The measurement data are treated and compared to theoretical estimations. Also is some suggestions for further work on this subject mentioned and a more ideally instrument setup is introduced.

5.1 Conclusion

In this work, a refractometer has been constructed and tested experimentally by measuring refractive indices of *NaCl* solutions corresponding to salinities covering the whole oceanographic range. The refractometer was designed mainly for high robustness and easy implementation for in situ usage, but was also desired cover the whole salinity range and to have a precision level of 10^{-6} RIU.

The experimental results revealed that the instrument was able to short-term measurements with an accuracy of $1.5 \cdot 10^{-5}$ RIU, but poor repeatability of the instrument decreased the overall accuracy to $2.9 \cdot 10^{-4}$ RIU. The increased uncertainties is considered to be caused by either small displacements in the tweakable components in the setup or by slow drifts in the laser/detector caused by heating processes.

Since the refractometer setup constructed in this thesis is not viable for further development and application to an in situ sensor, a more ideally setup design has been proposed in the next subsection. If the repeatability problems experienced during this thesis are avoided, the new design should be able to met all the requirements mentioned in section 1.1.

5.2 Ideal sensor

The refractometer setup in this thesis has shown that having a cylindrical water chamber is not a direct obstacle when constructing a refractometer. Having this geometry gives great advantages in terms of robustness and implementation of anti-biofouling systems. It has also been shown short term measurements of displacements caused by salinity can be performed with accuracy of at least 5 μm. With this in mind a more ideal sensor setup has been designed.

Figure 5.1 shows a sketch of a cross section of the ideal sensor. As we see there are no usage of immersion oil and no place where detection of extra light reflection can occur. Thus the problems causing poorer measurement accuracy at the main setup are avoided. With the exact geometrical setup as shown in Figure 5.1, a refractive index change in the water sample from $n_w = 1.345$ to $n_w = 1.355$ will give a displacement change of the detected laser spot of 5.48 mm. If the displacement measurement accuracy is 5 μm, this corresponds to an intrinsic refractive index accuracy of $9.1 \cdot 10^{-7}$ RIU. The drawback of this setup is that the total measurement range is decreased to ~0.0013 RIU. This problem can be solved by having a mechanical feedback control system attached to the two mirrors. This way the incident angle θ_i can be change continuously in coordination with the refractive index of the water sample, thus increasing the detection range of the sensor to cover the whole oceanographic range.

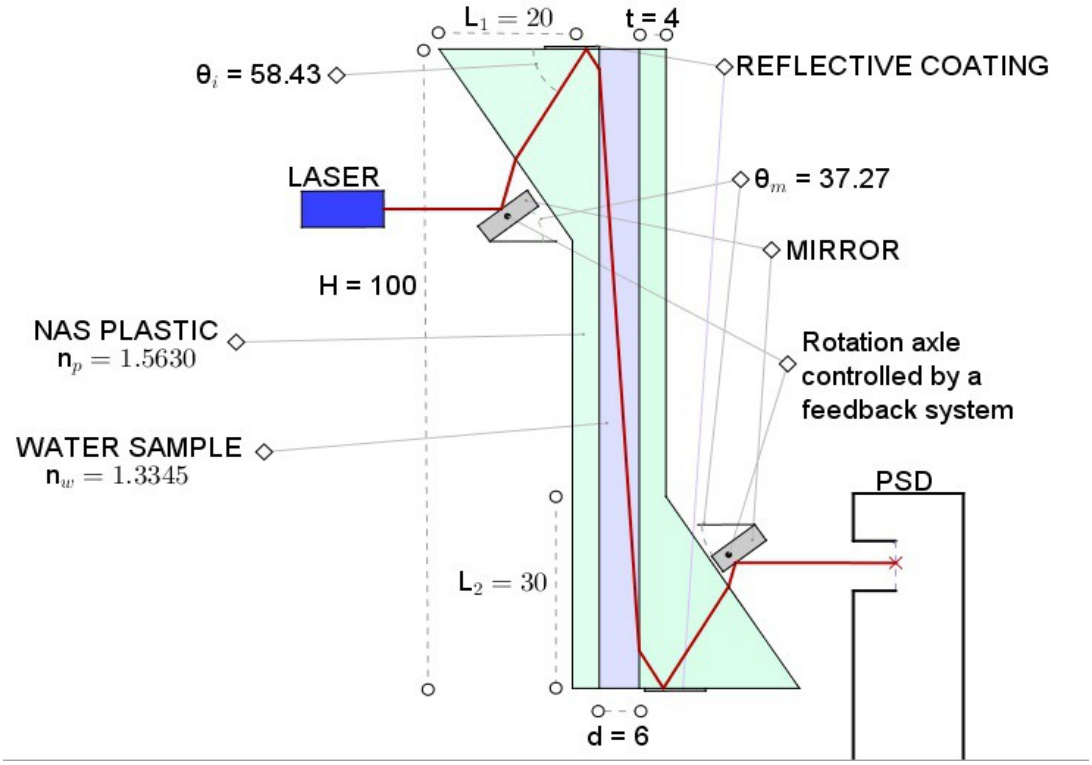

Figure 5.1: Sketch of an ideal sensor setup.

The geometrical construction of the component shown if Figure 5.2 may be to complex to be made of glass. Fortunately there has been great development of quality optical products made of plastic [50]. Plastics optics already has advantages compared to glass products; lower cost, higher impact resistance, lighter weight and more configuration possibilities. At this specific construction the plastic type SAN (styrene acrylonitrile) look most promising, having a refractive index of 1.563 at 25 °C for light with wavelength of 589 nm. The NAS plastic is also scratch and chemical resistant and having acceptable thermal expansion.

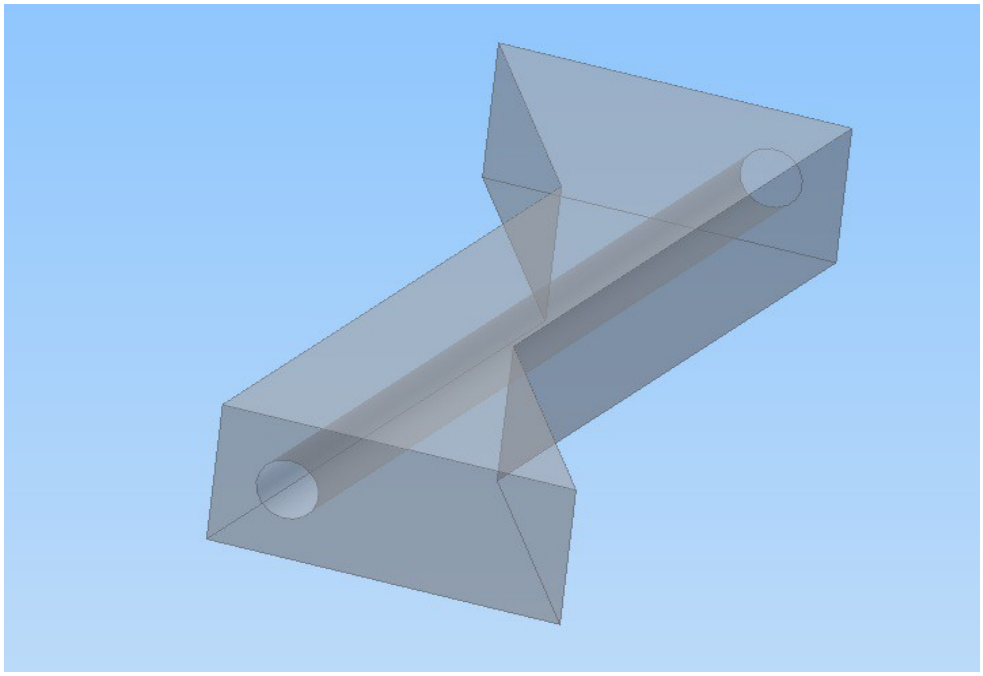

Figure 5.2: A 3D model of the preferred sample house.

5.3 Further work

A natural next step of investigation of the work done in this thesis is to constructed the refractometer setup suggested in section 5.2. The refractometer should be manufactured by a high precision machinery, providing firmly fixed, accurate positioning and direction of instrument components. This way some of the repeatability noise experienced during this thesis may be prevented.

Using a pulsed voltage source to drive the instrument electronics is also worth to investigate. This will lower the overall power consumption of the instrument, which will have a limited power source during in situ operation. Having a low duty pulsed voltage source will also decrease heating in laser/detector housing significantly, which may prevent some of the repeatability noise experienced during this thesis.

Implementation of a protection system against biofouling should also be investigated. For example could a small rotating wiper device be implemented to the sample house. If the rotation speed of the wiper matches the measurement frequency of the instrument, the wiper could continuously clean the house without disrupting the measurements. In this way one could prevent the growth of the primary biofilm, which is the first step of biofouling.

Bibliography

[1] *Theory and Application of Conductivity*, Emerson Process Management. Last checked: 14.06.2013. http://www2.emersonprocess.com/siteadmincenter/PM%20Rosemount%20Analytical%20Documents/Liq_ADS_43-018.pdf.

[2] Ulrich Lüttge and André Läuchli. *Salinity: Environment - Plants - Molecules.* Kluwer Academic Publishers, 2002.

[3] Ruth Francis-Floyd. *The Use of Salt in Aquaculture*. Institute of food an Agricultural Sciences. Last checked: 01.08.2013. http://edis.ifas.ufl.edu/pdffiles/VM/VM00700.pdf.

[4] Roswell W. Austin and Georgia Helikas. *The index of refraction of seawater.* University of California, San Diego, 1976.

[5] Raymond W. Schmitt. *Salinity and the Global Water Cycle.* Oceanography, 21(1):12-19, 2008.

[6] Robert H. Stewart. *Introduction To Physical Oceanography.* Texas A & M University, 2008.

[7] Philippe Grosso, Marc Le Menn, Jean-Louis De Bougrenet De La Tocnaye, Zong Yan Wu and Damien Malarde. *Practical versus absolute salinity measurements: New advances in high performance seawater salinity sensors*. Deep-Sea Research I 1(57):151–156, 2010.

[8] IOC, SCOR and IAPSO. *The international thermodynamic equation of seawater – 2010*: Calculation and use of thermodynamic properties. Intergovernmental Oceanographic Commission, Manuals and Guides No. 56, UNESCO (English), 2010.

[9] Anssi Mäkynen. *Position-Sensitive Devices and Sensor Systems for Optical Tracking and Displacement Sensing Applications*. Academic dissertation, University of Oulu, 2000.

[10] Timothy Boyer and Sydney Levitus. *Quality Control and Processing of Historical Oceanographic Temperature, Salinity, and Oxygen Data*. National Oceanographic Data Center, 1994.

[11] SCOR/IAPSO Working Group 127. *Certified Research and Development Need - CRDN Refraction Index of Seawater*, 2009. Last checked: 01.08.2013. http://www.io-warnemuende.de/tl_files/staff/rfeistel/download/CRDN_RI_2007.pdf.

[12] M. Le Menn, J. L. de Bougrenet de la Tocnaye, P. Grosso, L. Delauney, P. Brault, C. Podeur and O. Guillerme. *Advances in measuring ocean salinity with an optical sensor.* Measurement Science and Technology 22(11):1–8, 2011.

[13] Øyvind Tengesdal. *Measurement of seawater refractive index and salinity by means of optical refraction*. Master thesis. University of Bergen, 2012.

[14] Hugene Hecht. *Optics*, 4.ed. San Francisco, Calif.: Pearson Addison Wesley, 2002.

[15] John R. Reitz, Frederick J. Milford and Robert W. Christy. *Foundations of Electromagnetic Theory*, 4.ed. Reading, Massa.: Addison-Wesley Publishing Company, 1993.

[16] Tom Tiwald. *Sellmeier Dispersion.* Last checked: 20.08.2013. http://www.jawoollam.com/Newletters/TechNotes/sellmeier_dispersion.pdf.

[17] Shyam Singh. *Refractive Index Measurement and its Applications*. Physica Scripta 65:167–180, 2002.

[18] B. W. Grange, W. H. Stevenson and R. Viskanta. *Refractive index of liquid solutions at low temperatures: an accurate measurement.* Applied Optics 15: 858–859, 1976.

[19] Thomsa H. Barnes, Kenji Matsumoto, Tomoaki Eiju, Kyofumi Matsuda and Noatake Ooyama. *Grating interferometer with extremely high stability, suitable for measuring small refractive index changes*. Applied Optics 30(7):745–751, 1991.

[20] Gregory C. Johnson, John M. Toole and Nordeen G. Larson. *Sensor Correction for Sea-Bird SBE-41CP and SBE-41 CTDs**. Journal of Atmospheric and Oceanic Technology 24:1117-1130, 2007.

[21] Øivin Holter, Finn Ingebretsen and Hugo Parr. *Fysikk og energiressurser.* 2. ed. Oslo: Universitetsforlaget, 1998.

[22] Lidia Łukasiak and Andrzej Jakubowski. *History of Semiconductors*. Journal of Telecommunications and Information Technology, 1, 2010.

[23] Paul A. Tipler and Ralph A. Llewellyn. *Modern Physics.* 5. ed.: New York: W.H. Freeman and Company, 2008.

[24] Melles Griot. *Introduction to Laser Technology.* Last checked: 14.06.2013. https://www.cvimellesgriot.com/products/Documents/TechnicalGuide/Basic_Laser_Principles.pdf.

[25] Kamran S. Mobarhan. *Test and Characterization of Laser Diodes: Determination of Principal Parameters*. Last checked: 18.08.2013. http://www.ele.uva.es/~pedro/optoele/lasers/LD_parameters_Newport.pdf.

[26] Matthias Pospiech and Sha Liu. *Laser Diodes an Introduction*. University of Hannover, 2004. Last checked: 07.05.2013. http://www.matthiaspospiech.de/files/studium/praktikum/diodelasers.pdf .

[27] Henrik Andersson. *Position Sensitive Detectors - Device Technology and Applications in Spectroscopy*. Doctor thesis. Mid Sweden University, 2008.

[28] OSI Optoelectronics. *Photodiode Characteristics and Applications*. Last checked: 07.06.2013. http://www.osioptoelectronics.com/application-notes/AN-Photodiode-Parameters-Characteristics.pdf.

[29] Date Jan Willem Noorlag. *Lateral-photoeffect position-sensitive detectors*. Rotterdam University, 1982.

[30] BetaTHERM Sensors. *NTC Thermistor theory*. Last cheked: 19.05.2013. http://www.beta.dk/betathermkatalog/teoridel.pdf.

[31] ILX Lightwave Corporation. *Thermistor Calibration and the Steinhart-Hart Equation*. Last checked: 18.08.2013. http://assets.newport.com/webDocuments-EN/images/AN04_Thermistor_Calibration_IX.PDF

[32] James W. Nilsson and Susan A. Riedel. *Electric Circuits*. 9. ed.: Pearson Education, inc. 2011.

[33] Schott AG Company. *Optical Glass Data Sheets*. Last checked: 28.03.2013. http://www.schott.com/advanced_optics/us/abbe_datasheets/schott_datasheet_all_us.pdf.

[34] Egil Lillestøl, Ola Hunderi and Jan R. Lien. *Generell fysikk for universiteter og høgskoler – Bind 2 Varmelære og elektromagnetisme*. 2. ed.: Universitetsforlaget, 2006.

[35] R.C. Millard and G. Seaver. *An index of refraction algorithm for seawater over*

temperature, pressure, salinity, density and wavelength. Deep-Sea Research 37(12):1909–1926, 1990.

[36] Roland A. Madden. *Estimates of the Natural Variability of Time-Averaged Sea-Level Pressure*. Monthly Weather Review 104(7):942–952, 1976.

[37] John P. Bently. *Principles of Measurement Systems.* 4. ed.: Essex, England: Pearson Education Limited, 2005.

[38] L. Delauney, C. Compère and M. Lehaitre. *Biofouling protection for marine environmental sensors*. Ocean Sci. 6:503–511, 2010.

[39] Ilker Fer and David Peddie. *Near surface oceanographic measurements using the SailBuoy*. Last cheked: 20.08.2013. http://sailbuoy.no/files/CMR-12-A10266-RA-2%20Near%20surface%20oceanographic%20measurements%20using%20the%20SailBuoy.pdf.

[40] Raymond W. Schmitt and Robert A. Petitt. *A fast response, stable CTD for gliders and AUVs*. Last checked: 11.07.2013. http://www.neilbrownoceansensors.com/pdf/Schmitt_Petitt_MTS_06.pdf.

[41] CVI Melles Griot. *Material Properties*. CVI Melles Griot 2009 Technical Guide 2(1):4.14-4.24, 2009.

[42] Carmetal dynamic cad software. Last checked: 14.08.2013: http://db-maths.nuxit.net/CaRMetal/index_en.html.

[43] Ferro Tec. *Temescal Precision Coating Solutions*. Last checked: 26.07.2013. http://www.temescal.net/downloads/temSystemsBrochure.pdf

[44] Olympus Immersion Oil - IMMOIL-F30CC (n = 1.518). Last checked: 19.07.2013. http://www.olympusamerica.com/seg_section/uis2/seg_uis2_immersionoil.asp?

intCmp=seg_rdir_oil.

[45] Vernier. Salinity Sensor user manual. Last checked: 26.07.2013. http://www.vernier.com/files/manuals/sal-bta.pdf.

[46] Vernier. Stainless Steel Temperature Probe user manual. Last checked 26.07.2013. http://www.vernier.com/files/manuals/tmp-bta.pdf.

[47] James H. McClellan, Ronald W. Schafer and Mark A. Yoder. *Signal Processing First*. USA: Pearson Education, inc. 2003.

[48] Mathworks. Matlab Data Sheet. Last checked: 27.07.2013. http://www.mathworks.com/products/datasheets/pdf/matlab.pdf.

[49] Photon Technology International. *The Measurement of Sensitivity in Fluorescence Spectroscopy*. Last checked: 08.12.2012. http://www.pti-nj.com/LaserStrobe/TechNotes/MeasurementSensitivity.pdf.

[50] Kent Kogler. *Selection of Plastic for Optical Applications*. Last checked: 13.08.2013. http://ammtiac.alionscience.com/pdf/1999MaterialEase8.pdf.

[51] Thorlabs. PDQ80A data sheet. Last checked: 02.05.2013. http://www.thorlabs.de/catalogpages/V21/1587.PDF.

[52] Thorlabs. PDQ90A data sheet. Last checked: 02.05.2013. http://www.thorlabs.de/catalogpages/V21/1586.PDF.

[53] Gerhard Bohm, Günter Zech. *Introduction to Statistics and Data Analysis for Physicists*. Verlag Deutches Elektronen-Synchrotron, Hamburg, 2010.

Appendix A - Optical equations of state

A.1 Sellmeier dispersion equation of N-BK7

The refractive index n of N-BK7 glass used in this thesis is determined by the Sellmeier equation [16]:

$$n^2 = 1+\sum_{k=1}^{m}\frac{B_k\lambda^2}{\lambda^2-C_k},$$

where λ is the wavelength of light, and B_k and C_k are constants found empirically. During measurements with varying temperature, an additional equation was used to determined the refractive index [16]:

$$\frac{dn(\lambda,T)}{dT} = \frac{n^2(\lambda,T_0)-1}{2n(\lambda,T_0)}\left(D_0+2D_1\Delta T+3D_2\Delta T^2+\frac{E_0+2E_1\Delta T}{\lambda^2-\lambda_{TK}^2}\right),$$

where T_0 is standard temperature of 15 ºC, $\Delta T = T-T_0$ is the temperature difference, and D_i, E_i, and λ_{TK} are constants. The numerical values of the different constants used are:

Table A.1 : Dispersion coefficients

B_1	1.03961212	D_0	$1.86\cdot10^{-6}$
B_2	0.231792344	D_1	$1.31\cdot10^{-8}$
B_3	1.01046945	D_2	$-1.37\cdot10^{-11}$
C_1	0.00600069867	E_0	$4.34\cdot10^{-7}$
C_2	0.0200179144	E_1	$6.27\cdot10^{-10}$
C_3	103.560652	$\lambda_{TK}[\mu m]$	0.17

A.2 Millard and Seaver algorithm for seawater

The Millard and Seaver algorithm gives the refraction index of seawater,

based on the input parameters: temperature T [ºC], pressure p [db], practical salinity S [psu], and wavelength λ [μm] [35].

$$N_{MS}(T,p,S,\lambda) = N_I(T,\lambda) + N_{II}(T,\lambda,S) + N_{III}(p,T,\lambda) + N_{IV}(S,p,T).$$

The algorithm was constructed by applying the least-squares regression method on four individual experimental data sets. These data sets consists of a total of 428 data points covering the range from 0 to 30°C, 0 to 11 000 decibar pressure, and 0 ppt and 35 psu salinity. The two first data sets (region I and II) was measured at atmospheric pressure via the minimum deviation prism method, given at 0,6 ppm and 30 ppm accuracy for pure and sea waters. The two other sets (region III and IV), for pure and sea waters at elevated pressure, was measured via interferometer methods with 100 ppm and 60 ppm accuracy. Because of the variating accuracies of the data the algorithm also variates in accuracy, ranging in standard deviation in RIU from $1{,}2\cdot10^{-7}$ to $26{,}5\cdot10^{-6}$.

Region I

$$N_I(T,\lambda) = A0 + L2\cdot\lambda^2 + LM2/\lambda^2 + LM4/\lambda^4 + LM6/\lambda^6 + T1\cdot T + T2\cdot T^2 + T3\cdot T^3 + T4\cdot T^4 + TL\cdot T\cdot\lambda + T2L\cdot T^2\cdot\lambda + T3L\cdot\lambda\cdot T^3$$

Table A.2.1 : N_{MS} - Region I coefficients

$A0$	1.3280657	$T2$	-0.0000030738272 $[^\circ C^{-2}]$
$L2$	-0.0045536802 $[\mu m^{-2}]$	$T3$	0.000000030124687 $[^\circ C^{-3}]$
$LM2$	0.0025471707 $[\mu m^2]$	$T4$	$-2.0883178\cdot10^{-10}$ $[^\circ C^{-4}]$
$LM4$	0.000007501966 $[\mu m^4]$	TL	0.000010508621 $[^\circ C^{-1}\mu m^{-1}]$
$LM6$	0.000002802632 $[\mu m^6]$	$T2L$	0.00000021282248 $[^\circ C^{-2}\mu m^{-1}]$
$T1$	-0.0000052883907 $[^\circ C^{-1}]$	$T3L$	$-1.705881\cdot10^{-9}$ $[^\circ C^{-3}\mu m^{-1}]$

Region II

$$N_{II}(T,\lambda) = S0\cdot S + S1LM2\cdot S/\lambda^2 + S1T\cdot S\cdot T + S1T2\cdot S\cdot T^2 + S1T3\cdot S\cdot T^3 + STL\cdot S\cdot T\cdot\lambda$$

Table A.2.2 : N_{MS} - Region II coefficients

$S0$	0.00019029121	$S1T2$	$8.9818478 \cdot 10^{-9}$ $[^{\circ}C^{-2}]$
$S1LM2$	0.0000024239607 $[\mu m^2]$	$S1T3$	$1.2078804 \cdot 10^{-10}$ $[^{\circ}C^{-3}]$
$S1T$	-0.00000073960297 $[^{\circ}C^{-1}]$	STL	$-3.589495 \cdot 10^{-7}$ $[^{\circ}C^{-1}\mu m^{-1}]$

Region III

$$N_{III}(p,T,\lambda) = P1 \cdot p + P2 \cdot p^2 + PLM2 \cdot p/\lambda^2 + p/\lambda^2 + PT \cdot p \cdot T + PT2 \cdot p \cdot T^2 + P2T2 \cdot p^2 \cdot T^2$$

Table A.2.3 : N_{MS} - Region III coefficients

$P1$	0.0000015868383 $[db^{-1}]$	PT	$-9.4834486 \cdot 10^{-9}$ $[^{\circ}C^{-1}db^{-1}]$
$P2$	$-1.574074 \cdot 10^{-11}$ $[db^{-2}]$	$PT2$	$1.0100326 \cdot 10^{-10}$ $[^{\circ}C^{-2}db^{-1}]$
$PLM2$	$1.0712063 \cdot 10^{-8}$ $[db^{-1}\mu m^2]$	$P2T2$	$5.8085198 \cdot 10^{-15}$ $[^{\circ}C^{-2}db^{-2}]$

Region IV

$$N_{IV}(S,p,T) = P1S \cdot p \cdot S + PTS \cdot p \cdot T \cdot S + PT2S \cdot p \cdot T^2 \cdot S$$

Table A.2.4: N_{MS} - Region IV coefficients

$P1S$	-0.0000000011177517 $[db^{-1}]$	$PT2S$	$-1.5460458 \cdot 10^{-12}$ $[^{\circ}C^{-2}db^{-1}]$
PTS	$5.7311268 \cdot 10^{-11}$ $[^{\circ}C^{-1}db^{-1}]$		

A.2 Algorithm for immersion oil

During the experiment it was observed that the immersion oil used in the thesis had a refractive index dependent on temperature. By measuring displacements with the refractometer while the temperature was the only varying parameter, a refractive index value of the immersion oil was found numerically to each single displacement measurement. The following polynomial was found in Matlab, and was used as a temperature dependent algorithm for the immersion oil:

$$n_o(t) = p_1 \cdot t^9 + p_2 \cdot t^8 + p_3 \cdot t^7 + \ ... \ + p_2 \cdot t + p_{10}$$

Table A.3: n_o - Polynomial coefficients

p_1	$7.961 \cdot 10^{-6}$ $[^\circ C^{-9}]$	p_6	$7.861 \cdot 10^{-5}$ $[^\circ C^{-4}]$
p_2	$-1.325 \cdot 10^{-5}$ $[^\circ C^{-8}]$	p_7	-0.0007034 $[^\circ C^{-3}]$
p_3	$-8.761 \cdot 10^{-5}$ $[^\circ C^{-7}]$	p_8	-0.0001105 $[^\circ C^{-2}]$
p_4	$6.377 \cdot 10^{-5}$ $[^\circ C^{-6}]$	p_9	0.0002568 $[^\circ C]$
p_5	0.000352 $[^\circ C^{-5}]$	p_{10}	1.518

Appendix B – PSS 78 algorithm

Practical salinity is defined on the Practical Salinity Scale of 1978 (Unesco (1981, 1983)) in the terms of the conductivity ratio, denoted K_{15} , between the sample and a standard potassium chloride (KCl) solution both at the temperature of 15 °C and one standard atmosphere pressure [8]. The standard solution contains a mass fraction of KCl equal to $32{,}4356 \cdot 10^{-3}$. Practical Salinity is defined only in the range $2 < S_P < 42$ and is per definition equal 35 when $K_{15} = 1$:

$$S_P = \sum_{i=0}^{5} a_i (K_{15})^{\frac{i}{2}}$$

Table B.1 : PSS-78 coefficients

a_0	0.0080	a_3	14.0941
a_1	-0.1692	a_4	-7.0261
a_2	25.3851	a_5	2.7081

Appendix C – Seawater composition

Seawater compositions definition for reference salinity of the standard ocean [8]:

Table C.1 : The sea salt composition

Solute	Mass fraction (Sum = 1)
Na^+	0.3065958
Mg^{2+}	0.0365055
Ca^{2+}	0.0117186
K^+	0.01134945
Sr^+	0.0002260
Cl^-	0.5503396
SO_4^{2-}	0.0771319
HCO_3^-	0.0029805
Br^-	0.0019134
CO_3^{2-}	0.0004078
$B(OH)_4^-$	0.0002259
F^-	0.0000369
OH^-	0.0000038
$B(OH)_3$	0.0005527
CO_2	0.0000121

Appendix D – Statistical analyses

The goal of an experimental measurements is to give a numerical value to a characteristic of either an object or a system. In most cases the measurement data will be randomly distributed around the true value of the measurand, with a spread dependent on the measurement accuracy. Thus it is necessary to have standard guidelines of how to efficiently represent measurement data.

A standard way of representing the measurement data is by the *mean value*, which can be visualized as the center of gravity of the data distribution. The mean value $\overline{x}$ is defined by [53]

$$\overline{x} = \frac{1}{N}\sum_{i}^{N} x_i ,$$

where N is the sum of a sequence of x_1, x_2, … x_i samples.

The variance of the data distribution is often referred to as the accuracy of the mean value. This variance is often given as standard deviation σ_x of the measurement data, defined as [x]

$$\sigma_x = \sqrt{\frac{1}{N}\sum_{i}^{N} (x_i - \overline{x})^2} .$$

Appendix E – Reference refractometer

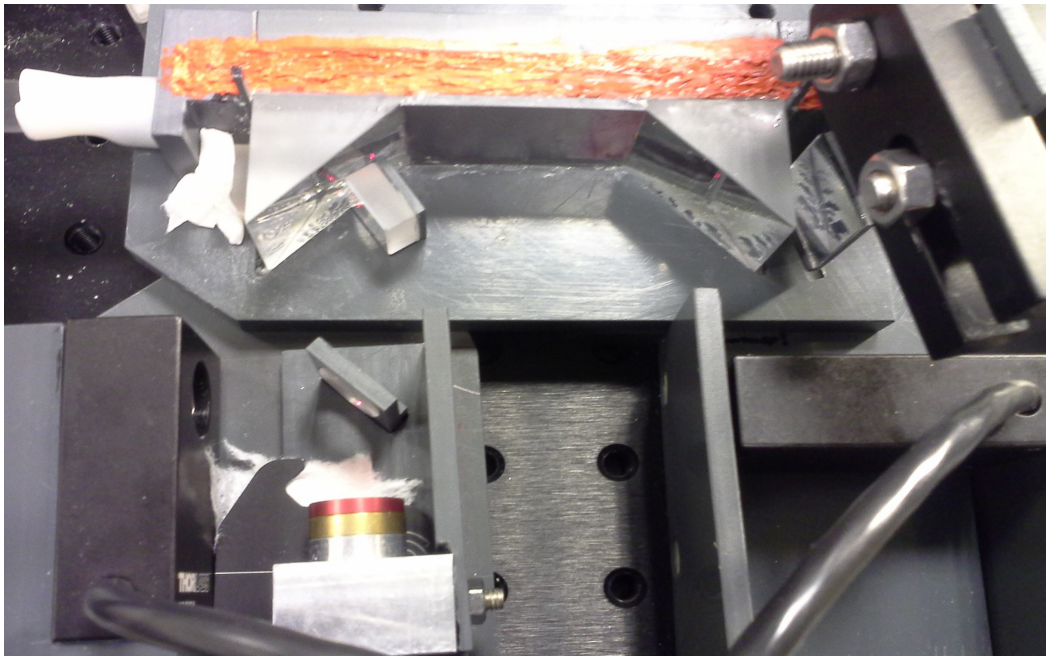

Figure E.1: A picture of the reference refractometer.

When constructing the refractometer setup described in the thesis, it was great uncertainty whether it would work as intended. As a precaution a reference setup was made, shown in Figure E.1. The reference setup have a very similar optical design as the main refractometer setup, but prisms are used instead of the glass cylinder and immersion oil.

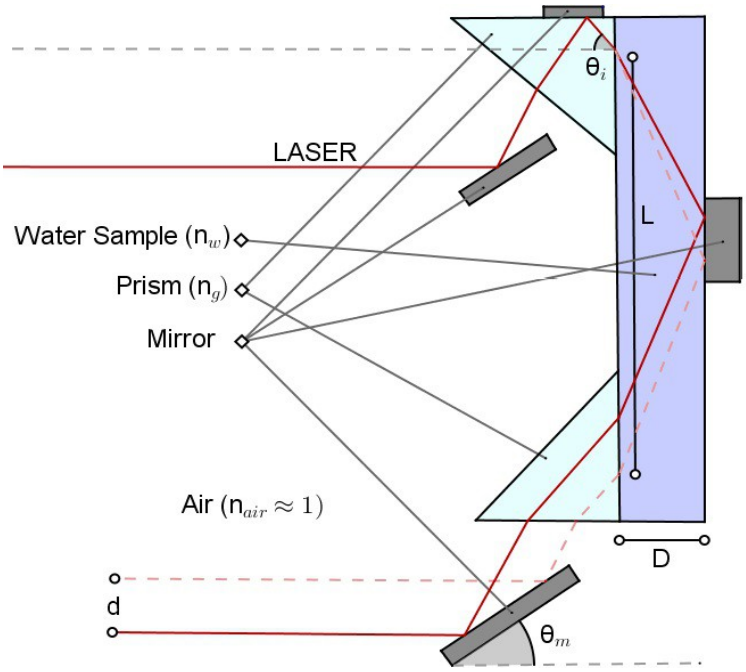

Figure E.2: Schematic drawing of the reference refractometer, not accurate. True scale drawings are shown in appendix F.

Table E.1 : Optical parts in the reference setup

Optical components	Characteristics	Model and manufacturer
Prisms	N-BK7, 25mm cathetus	Edmund Optics
Mirrors	Broadband mirrors, various sizes	Thorlabs

From the schematic drawing in Figure E.2 a theoretical model can be made for the displacement:

$$d = d_0 - \frac{2 \cdot D \cdot \tan\left[\sin^{-1}\left(\frac{n_g}{n_w} \cdot \sin\theta_i\right)\right]}{\tan\theta_i\left(1 - \tan\left[\sin^{-1}\left(n_g \cdot \sin\theta_i\right)\right] \cdot \tan\theta_m\right)}.$$

where d_0 is a constant. A temperature measurement was conducted with the reference setup, where a pure water sample was used. This measurement is used as a comparative basic when evaluating the performance of the main refractometer setup. When calculating the theoretical fit the following parameters were used: $D = 8$ mm,

d_0=45 mm, θ_i=59.5 °, and θ_m = 16°. The refractive index of the pure water sample n_w is found by the Millard-Seaver algorithm, equation (2.115). The refractive index of the N-BK7 prism n_g is determined by equation (2.85) and (2.109).

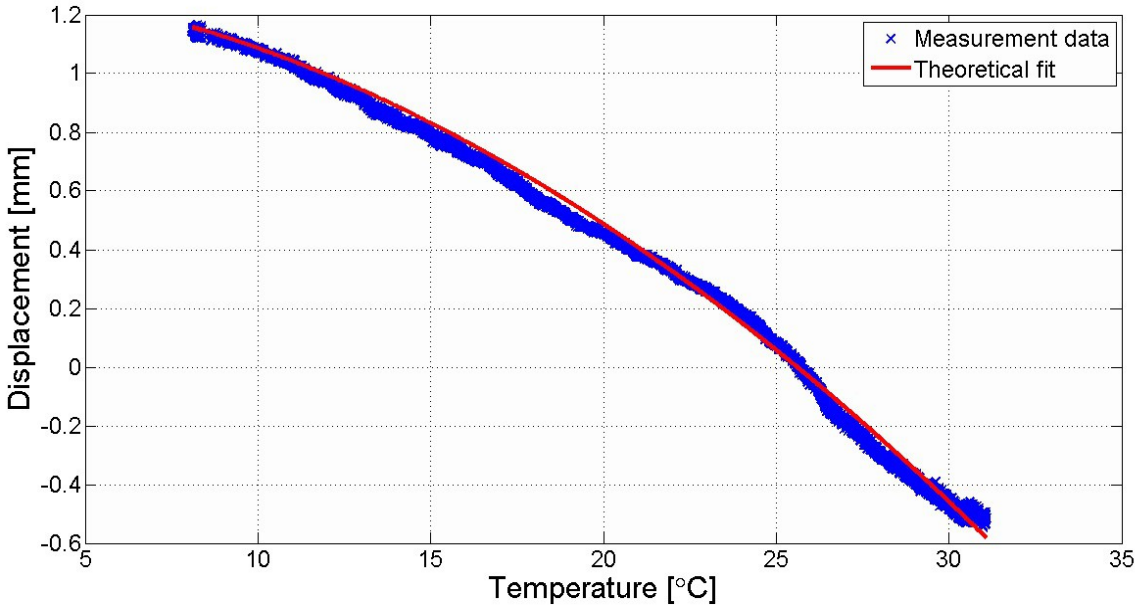

Figure E.3: Expected displacement and measured displacement versus temperature. Performed with the reference setup at 0 ppt salinity.

Appendix F – Setup sketches

This appendix shows the sketches of the base plates of the refractometer setups. The sketches were used during manufacturing of the setups. Figure F.1 shows the sketch for the main refractometer setup. Figure F.2 shows the sketch for the reference refractometer setup.

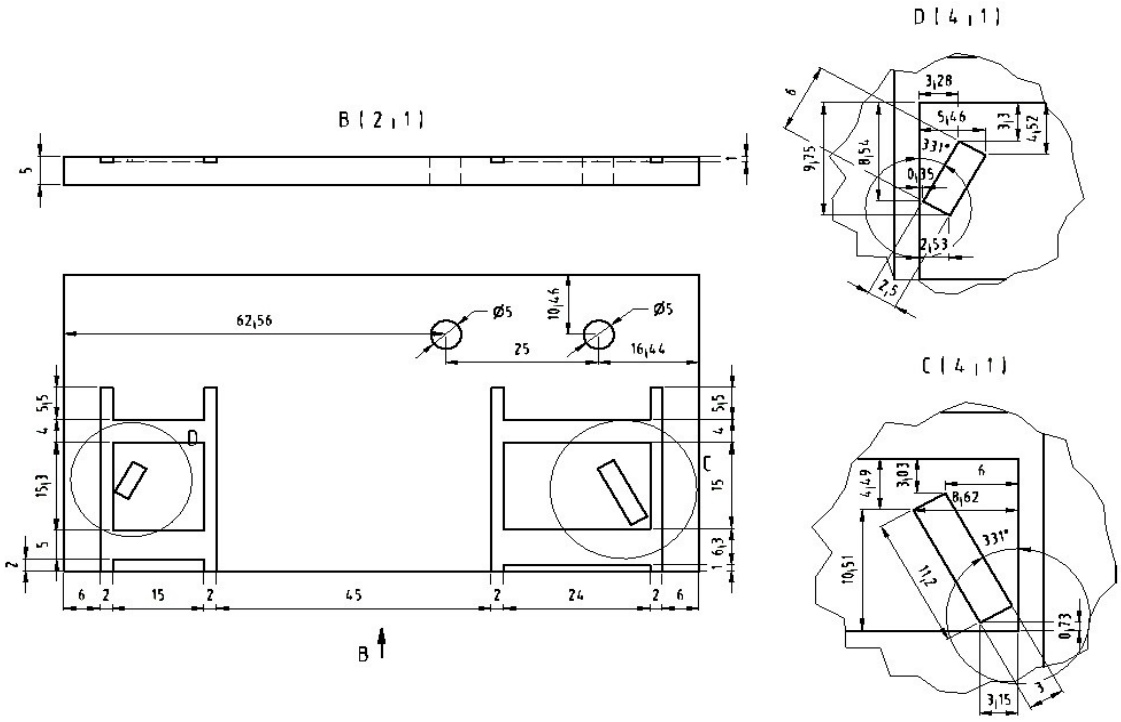

Figure F.1: A sketch of the main refractometer, dimensions in mm.

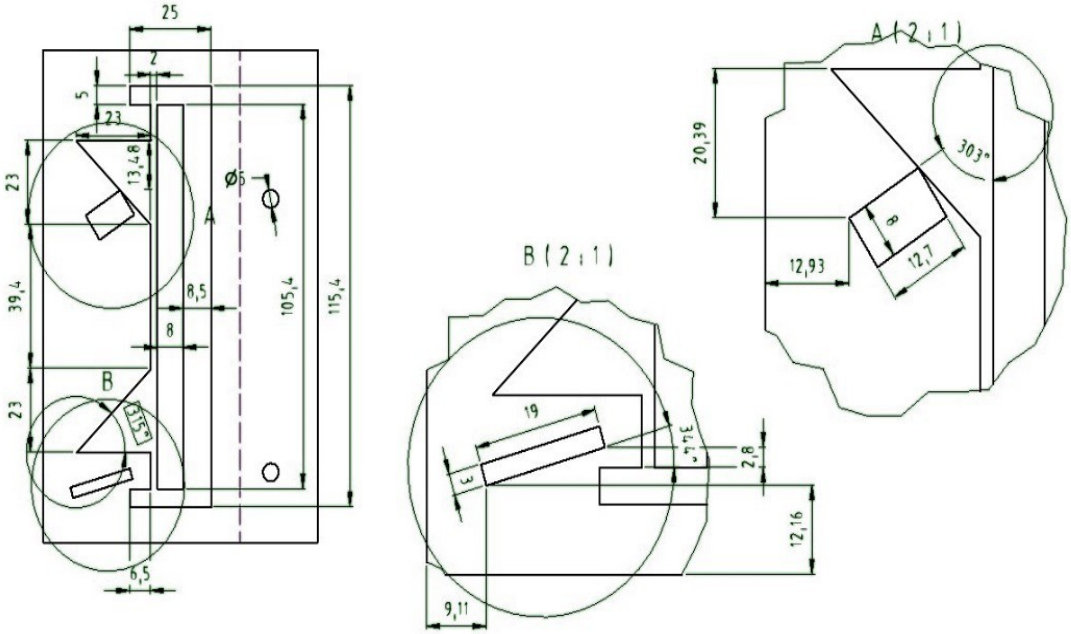

Figure F.2: A sketch of the reference refractometer, dimensions in mm.